

Title of my master thesis

Franziska Hellmuth



Thesis submitted for the degree of
Master in Meteorology
60 credits

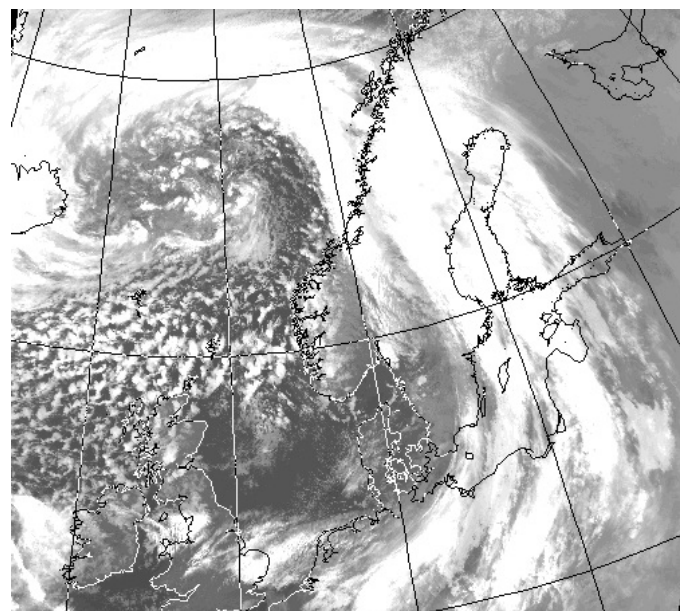
Department of Geoscience
Faculty of Mathematics and Natural Sciences

UNIVERSITY OF OSLO

Spring 2018

Title of my master thesis

Franziska Hellmuth



© 2018 Franziska Hellmuth

Title of my master thesis

<http://www.duo.uio.no/>

Printed: X-press printing house

ABSTRACT

This abstract needs to be updated.

TABLE OF CONTENTS

LIST OF ABBREVIATIONS	III
CHAPTER 1: INTRODUCTION	1
1.1 Measurement site - Haukeliseter	3
1.2 Observations in December	5
CHAPTER 2: ANALYSIS OF THE CHRISTMAS STORM 2016	7
2.1 Extreme weather	7
2.2 Dynamic Tropopause map	8
2.3 Thickness, Sea level pressure, moisture, and wind at 250 hPa	11
2.4 Atmospheric River map	13
2.5 Observations at the weather mast	15
2.6 Radiosonde from Stavanger	17
2.7 Large scale circulation	17
CHAPTER 3: INSTRUMENTATION, DATA, AND METHODOLOGY	21
3.1 Instruments	21
3.1.1 Double Fence	23
3.1.2 MRR - Micro Rain Radar	24
3.1.3 PiP - Precipitation Imaging Package	26
3.1.4 MASC - Multi-Angular Snowfall Camera	27
3.2 Optimal Estimation Retrieval Algorithm	28
3.2.1 Forward model	29
3.2.2 Snowfall retrieval scheme	31
3.2.3 Presence of snow	32
3.2.4 Size distribution	34
3.2.5 Snowfall rate at the surface	34
3.3 Numerical forecast model	35
3.3.1 AROME - MetCoOP	35

3.3.2	Meso-NH and the ICE3 scheme	36
3.3.3	Adjustment of ICE3 inside MEPS	39
3.4	Numerical data transformation	40
3.4.1	Layer thickness in MEPS	40
3.4.2	Snow water content	41
3.4.3	Snow water path	42
3.4.4	Ensemble mean and Ensemble spread	42
3.4.5	Dew point temperature for Skew-T log-P Diagram	42
CHAPTER 4: RESULTS AND DISCUSSION		44
4.1	Surface snowfall accumulation	44
4.1.1	Wednesday, 21 December 2016	49
4.1.2	Saturday, 24 December 2016	50
4.1.3	Sunday, 25 December 2016	52
4.2	Vertical Snow Water Content retrieved from optimal estimation and MEPS 48 h forecast	53
4.2.1	Verification of MEPS ensemble members	60
4.2.2	Wednesday, 21 December 2016	66
4.2.3	Saturday, 24 December 2016	67
4.2.4	Sunday, 25 December 2016	67
4.3	Wednesday, 21 December 2016	67
4.4	Saturday, 24 December 2016	67
4.5	Sunday, 25 December 2016	67
CHAPTER 5: SUMMARY AND CONCLUSION		73
REFERENCES		74
APPENDIX A: SYNOPTIC WEATHER SITUATION		81
A.1	Skew-T log-P diagram from Stavanger	81
APPENDIX B: FORWARD MODEL		85
B.1	Scattering Model	85
APPENDIX C: RESULTS		87
C.1	LWC and LWP from MEPS	87
C.2	Ensemble spread	90
C.3	Vertical SWC - ensemble member 0 to 9	93

LIST OF ABBREVIATIONS

AR	Atmospheric River
AROME	Applications of Research to Operations at Mesoscale
C3VP	Canadian CloudSat-CALIPSO Validation Project
CPR	Cloud Profiling Radar
DT	Dynamic Tropopause
ECMWF	European Centre for Medium-Range Weather Forecasts
EPS	Ensemble Prediction System
FMI	Finnish Meteorological Institute
IVT	Integrated Vapour Transport
MASC	Multi-Angular Snowfall Camera
MEPS	MetCoOp Ensemble Prediction System
Meso-NH	Mesoscale Non-Hydrostatic model
Met-Norway	Norwegian Meteorological Institute
MetCoOp	Meteorological Co-operation on Operational NWP
MRR	Micro Rain Radar
MSLP	Mean Sea Level Pressure

NWP	Numerical Weather Prediction
PIP	Precipitation Imaging Package
PSD	Particle Size distribution
SMHI	Swedish Meteorological and Hydrological Institute
SWC	Snow Water Content
SWP	Snow Water Path
WCB	Warm Conveyor Belt
WMO	World Meteorological Organization

CHAPTER 1: INTRODUCTION

During Christmas 2016 a storm impinged on the west coast of Norway. The storm, called 'Urd' was according to [Olsen and Granerød \[2017\]](#) associated with strong winds and high precipitation amounts. The midwind along the coast of Western Norway had hurricane strength (observed: 40 m s^{-1} to 55 m s^{-1}). In South and Eastern Norway west to north-west winds between 25 m s^{-1} to 40 m s^{-1} were measured. At the Haukeliseter measurement site, 136.4 mm of precipitation were monitored during 21 December 2016 to 27 December 2016. This event was just above the limit of been called an extreme weather. Storms of this kind are expected to occur on average every five years [[Olsen and Granerød, 2017](#)].

The financial costs associated with 'Urd' are estimated to about 180 million Norwegian kroner. 'Urd' led to major traffic problems for cars, trains, ferries and air planes. Most mountain crossings were kept closed during Christmas 2016. In addition, there was a power breakout of around 70.000 households and 40 emergency power stations failed during the extreme weather.

This extreme weather, might not have lead to the same damages as some of the extreme weather events of recent years. But since people are affected by extreme weather (Figure 1.0.1) it is important to predict storms, associated precipitation and wind as accurately as possible. Having accurate observations, will lead to better performing models which rely on observations. [include a reference here](#)

Figure 1.0.1 shows that precipitation and strong winds can influence in certain ways the infrastructure. To predict and measure snowfall accumulation as accurately as possible is important since snowfall has impact on avalanches, freshwater release into water systems in spring, and extra economical expenses for local infrastructure as well as climatological effects.

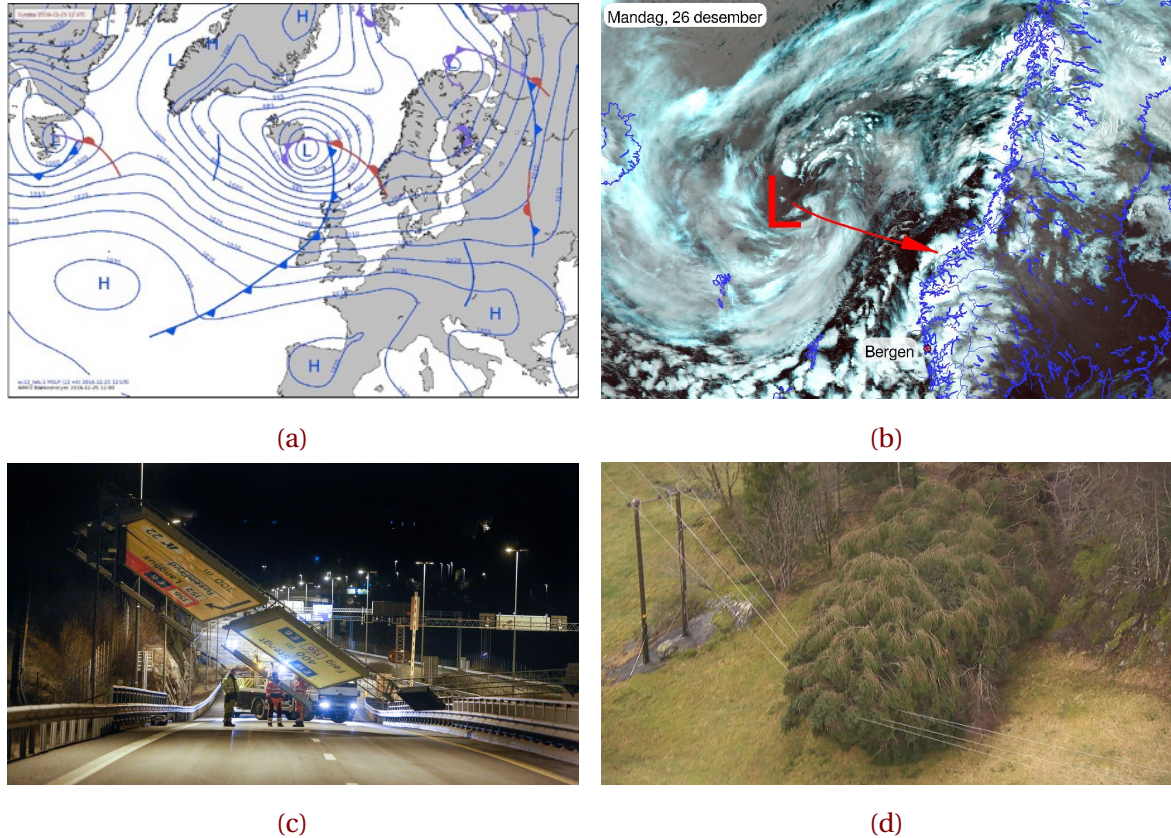


Figure 1.0.1: In **a**: Weather situation Sunday 25 December 2016 at 12 UTC, [Olsen and Granerød, 2017]. **b**: Tweet from Meteorologene [2016]: Here comes #Urd! The low pressure centre will hit Møre og Romsdal, but the strongest wind comes south of Stad. #SørNorge. **c**: This traffic sign, ten meter long and four meter high was blown down during the storm, [Ruud et al., 2016]. **d**: Trouble maker: The extreme weather during Christmas created problems for the local infrastructure. 80.000 households were without electricity during the storm, [Farestveit, 2016].

Joos and Wernli [2012] investigated the influence of microphysical processes on potential vorticity development in warm conveyor belts (WCB). They demonstrated the complex interaction between the small-scale microphysical processes and the large-scale flow in WCB. For the understanding of numerical simulations of storm developments it is important to know vertical precipitation profiles and their position within the synoptic vorticity environment. It is therefore crucial to study the vertical structure of different synoptic

storms and predict as accurately as possible.

Since November 2016, the Meteorological Cooperation on Operational Numerical Weather Prediction (MetCoOP) Ensemble Prediction forecast (MEPS) is operational at the Meteorological Institute of Norway (Met-Norway). The study by Müller et al. [2017] shows that the AROME-MetCoOp, a version of the Météo-France Applications of Research to Operations at Mesoscale, performs well for certain meteorological phenomena.

Microphysical processes in weather models are still not well understood and therefore are mostly parametrised [Müller et al., 2017]. Furthermore, high latitude regions are not well represented in meteorological models. Indeed a comparison between the MEPS data fit the observations for December 2016 but uncertainties are still present for this time period. Some satellites, such as CloudSat have been equipped with radar to estimate snowfall rates and vertical profiles of precipitation. CloudSat is one of the satellites orbiting in the A-Train formation and measures the vertical structure of cloud systems [Stephens et al., 2002].

Studies of Kulie and Bennartz [2009] showed that the Cloud Profiling Radar (CPR), mounted on the CloudSat, can be used to estimate global distributions of snowfall. They showed that different combinations of microphyiscal habits and fall speed can lead to the same results of reflectivity and therefore to the same amount of snowfall rate. Methods like optimal estimation retrieval were established to reduce the non-uniqueness. Where ground observations are used to estimate vertical profiles of precipitation.

The improvement of the CloudSat retrieval is helpful to show that climate models over estimate present-day Antarctic snowfall [Palerme et al., 2017]. Norin et al. [2015] presented a good agreement between the ground-based snowfall measurements and satellite observations.

1.1 MEASUREMENT SITE - HAUKELEISETER

Haukeliseter, shown in Figure 1.1.1 is a mountain plateau 991 m above sea level, located in the Norwegian county 'Telemark' (59.8° N, 7.2° E, Figure 1.1.1). The station measures precipitation, temperature, snow depth and wind. It has served as a measurement site for snow accumulation since the winter of 2010/2011 [Wolff et al., 2010, 2013, 2015].

The study site is surrounded by mountain tops being 100 m to 500 m higher than the flat

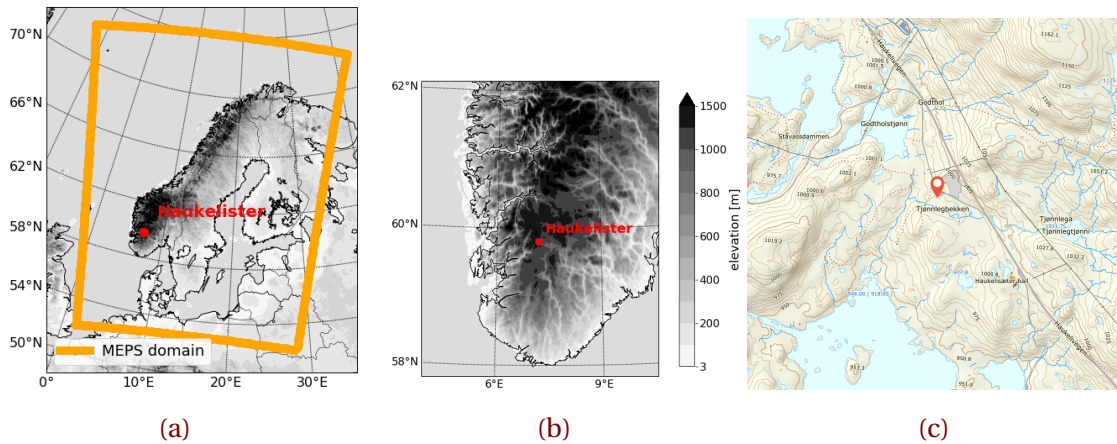


Figure 1.1.1: Elevation map of Northern Europe (a) and South Norway (b). Red dot indicates the location Haukeliseter and the orange square in a indicates the model domain of MEPS. Elevation according to the shading. c: topographical map of the measurement site marked with a red pin [Kartverket, 2018].

area. As seen in Figure 1.1.1c is the Haukeliseter measurement site located between two lakes, furthermore is it more open to the south and the west and the closest mountaintop (situated to the NE) has an altitude of 1162 masl, [Wolff et al., 2015].

In a study by Wolff et al. [2015] the wind-induced under-catch of solid precipitation is determined. Dependent on the kind of precipitation the wind plays different roles in the amount of accumulation. For temperatures below -2°C the wind speed influences the falling snow. Where less precipitation can be observed at higher wind speeds or more precipitation can be measured if too much is blown into the gauge. The catch ratio between the standard Geonor precipitation gauge and the DF-Geonor shows, that only 80 % of solid precipitation are observed at wind speeds of 2 m s^{-1} and only 40 % at 5 m s^{-1} , [Figure 5 in Wolff et al., 2015]. The double fence gauge is more accurate than the single fence and is used as the reference gauge. A further description of the double fence is found in Section 3.1.1. Nevertheless, this shows the need of a combination of ground based observations together with an optimal estimation retrieval to verify the accuracy of MEPS. Wolff et al. [2015] introduced an adjustment function for the Geonor double fence, so that different precipitation under certain wind speeds are presented correctly and can be used as confidential data.

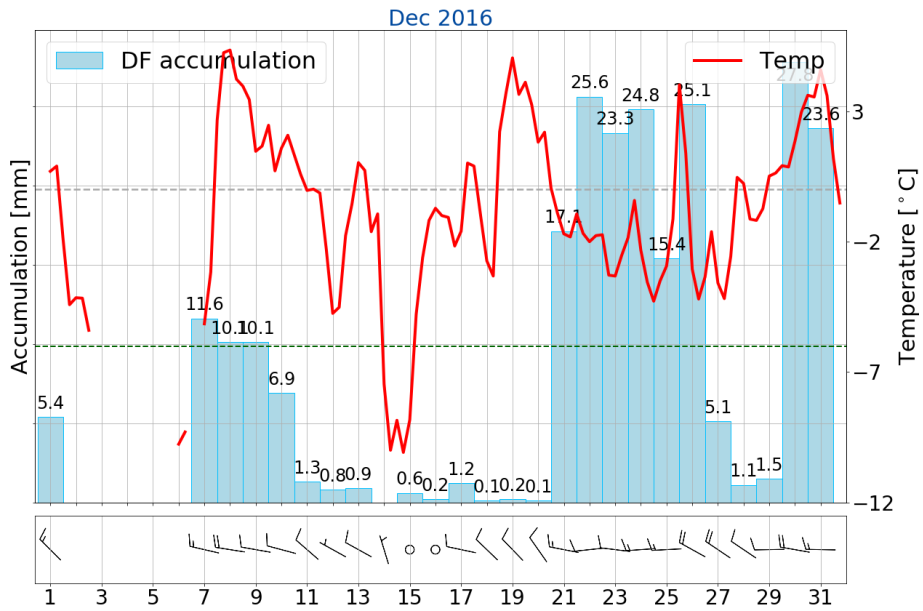


Figure 1.2.1: Observations at Haukeliseter weather mast for December 2016. Daily accumulation [mm] in light blue, mean temperature every six hours (red, [°C]), and daily maximum wind as barbs [m s^{-1}]. Gray dashed line indicates the freezing temperature. The monthly normal value is green dashed (-6.0°C), the values are taken from [eklima \[2016\]](#). Note, that no data was available from 2 December 2016 and 6 December 2016

1.2 OBSERVATIONS IN DECEMBER

The general climate at Haukeliseter can be defined with the updated Köppen-Geiger climate types presented in [Peel et al. \[2007\]](#). Figure 8 in [Peel et al. \[2007\]](#) shows, that Haukeliseter may lay in a transition zone and can be categorized as ET, a polar tundra climate type (hottest month temperature $T_{hot} \geq 0^\circ\text{C}$) or Dfc, a cold climate without dry season and cold summers. Haukeliseter presents a typical Norwegian climate condition. At the measurement site, frequent snow events combined with high wind speeds are observed during a six to seven month winter period. In addition a snow amount of about 2 m to 3 m can be expected, where 50 % of the yearly precipitation is solid [[Wolff et al., 2010, 2013, 2015](#)].

The mean wind direction for solid precipitation is from the west/east with maximum wind speeds above 15 m s^{-1} , observed during a 10 year winter period at a nearby station [[Wolff](#)

et al., 2010, 2015].

As seen in Figure 1.2.1 is the average December temperature -6°C (30-yr period 1961 to 1990, value taken from [eklima \[2016\]](#)). December 2016 was warmer with an anomaly of $+4.9\text{ K}$ above the climate mean. In 2016, the precipitation was 200 % more than the climate mean. [yr.no says something different. According to them was it only 76 %. But! change to double fence must have changed the precipitation amount to twice as much. Therefore probably wrong climate statistics since measured with single fence.](#) The precipitation observed in the time period 21 December 2016 to 27 December 2016 where 56.9 % of the total accumulation in December 2016. Furthermore, a maximum wind of 22.3 ms^{-1} was observed in this period, which can be associated to a slight storm, which is further described in Section 2.5 and Table 2.5.1.

CHAPTER 2: ANALYSIS OF THE CHRISTMAS STORM 2016

This extreme weather event is chosen since MEPS just became operational and in addition surface snow instruments where installed to profile the vertical at Haukeliseter. Preliminary test showed the overestimation of snow accumulation by MEPS compared to the measurements at the ground. Furthermore, was changed the phase between the precipitation.

The next sections will give a definition of an extreme weather, a description of the different weather maps, and a synoptic interpretation of the storm and why mixed phase precipitation was observed at Haukeliseter.

Before the analysis each weather maps' purpose will be presented to understand the connections between them. For this, the ECMWF ...blabla product... so many grid degree ... is processed.

2.1 EXTREME WEATHER

'Extreme weather' is a meteorological term, associated with the extent of a weather type. The Norwegian Meteorological Institute declares an extreme event, if strong winds, large amounts of precipitation and large temperature changes are expected before the event occurs. As well as a large avalanche risk is present and coastal areas are influenced by extremely high-water levels. All this occurred during the Christmas storm [[Olsen and Granerød, 2017](#)].

Generally, an event is divided into four phases that it can be called extreme [[Pedersen and](#)

Rommetveit, 2013].

Phase A: *Increased monitoring before the possible extreme weather.* The meteorologists give special attention to the weather situation. At this point it is not certain, that there will be an extreme weather event.

Phase B: *Short-term forecasts.* It is decided, that there will be an extreme event. The forecasts are more detailed and updates will be published at least every six hours. The event will get a name.

Phase C: *The extreme weather is in progress.* The meteorologists send out weather announcements at least every six hours.

Phase D: *The extreme weather event is over. Clean-up and repairs are in progress.* When the extreme weather is over the public is notified and information about the upcoming weather and clearing work is given.

2.2 DYNAMIC TROPOPAUSE MAP

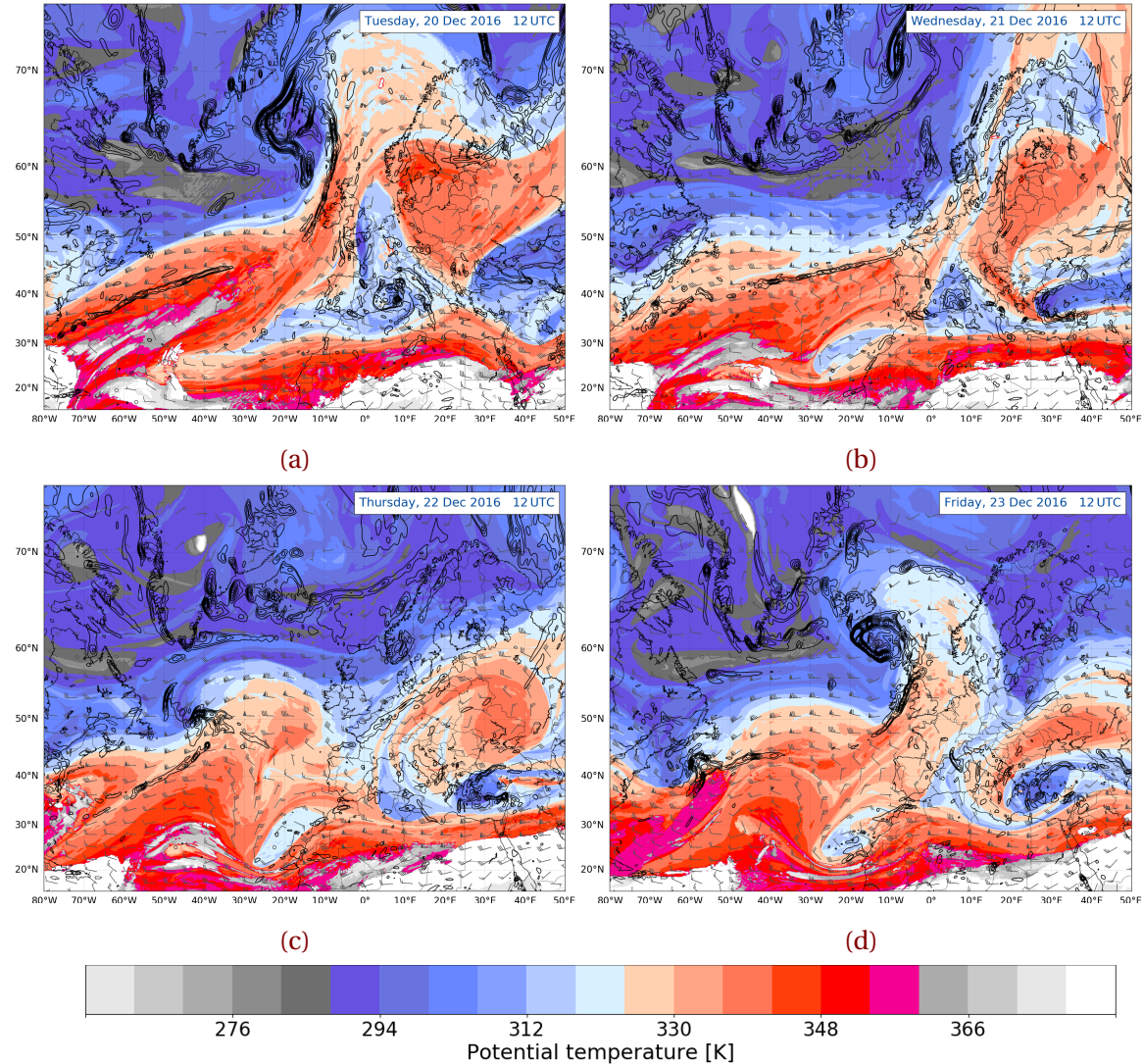
The dynamic tropopause map (DT), shown in Figure 2.2.1 presents the potential temperature distribution at the tropopause. Colder tropopause is associated with colder colours and vice versa warmer tropopause with warmer colours (shading according to the colorbar). Therefore, a warmer tropopause indicates an elevation of the atmospheric column.

The gradient at the 2 PVU (1 PV unit = $10^{-6} \text{ m}^2 \text{ s}^{-1} \text{ K kg}^{-1}$; Hoskins et al. [1985]) surface, between the cold and warm area indicates the thermal wind. There is a slope between the cold and warm surfaces increasing towards the warmer column averaged temperature. An increased slope means also an increased pressure gradient force with increasing height and therefore an increase in geostrophic wind. This means, that there exists a vertical wind shear. From this, the mid-latitude jet stream can be pointed out. **do I need to present the equation of thermal wind?** Wind barbs in m s^{-1} indicate the direction of the wind flow, which is generally from west to east in the mid-latitudes.

The 925 – 850 hPa layer-averaged surface relative vorticity is shown in black contours, every $0.5 \times 10^{-4} \text{ s}^{-1}$. It represents the rotation of a fluid. **Does the relative vorticity need more explanation?**

Along the Rossby-Wave-Guide, troughs and ridges are seen which can be combined with

the surface relative vorticity to understand the vertical dynamic interaction in the atmosphere. In case of a westward tilt between the surface cyclone and an upper level through an intensification of the surface cyclone is more likely to occur.



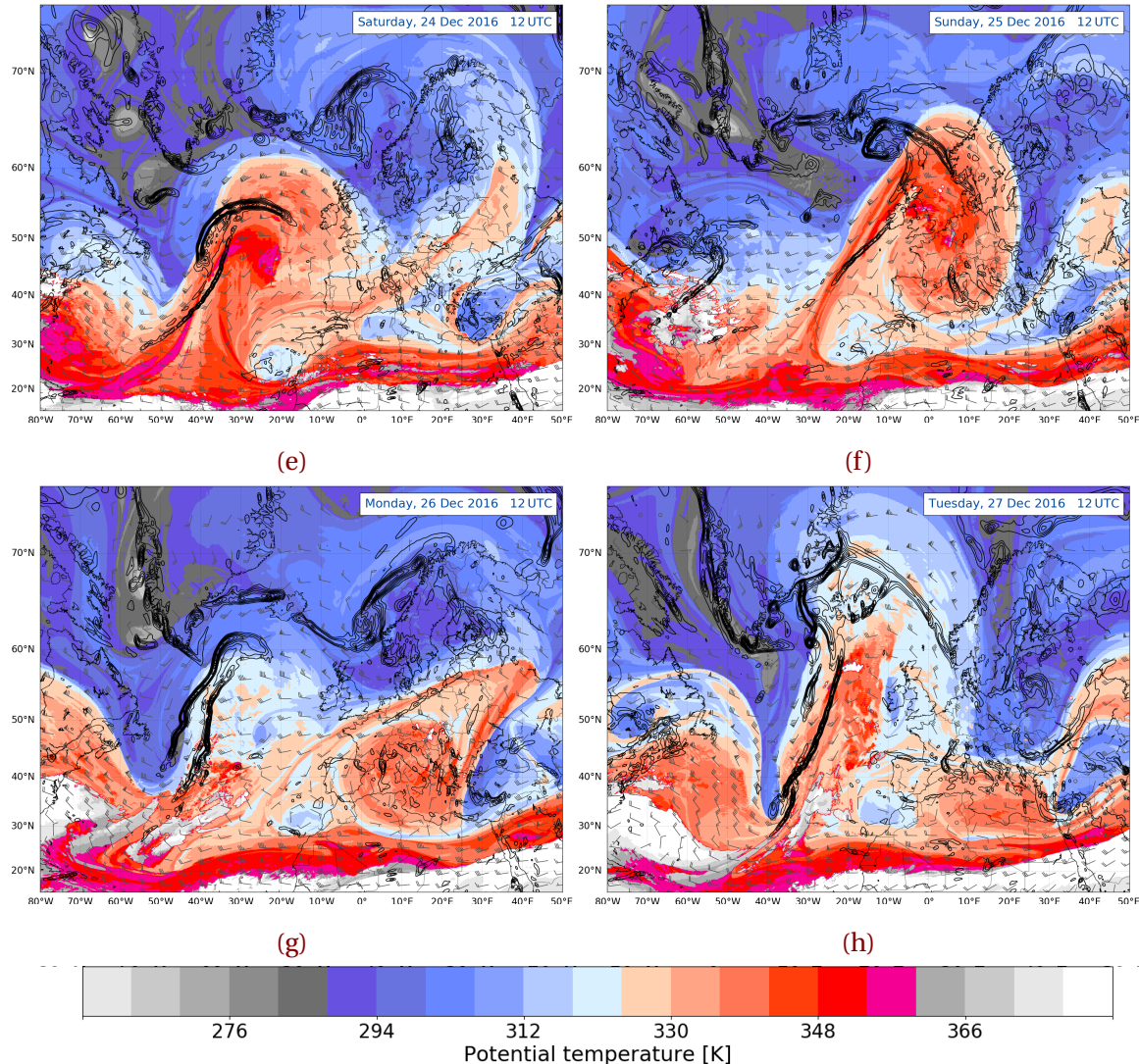
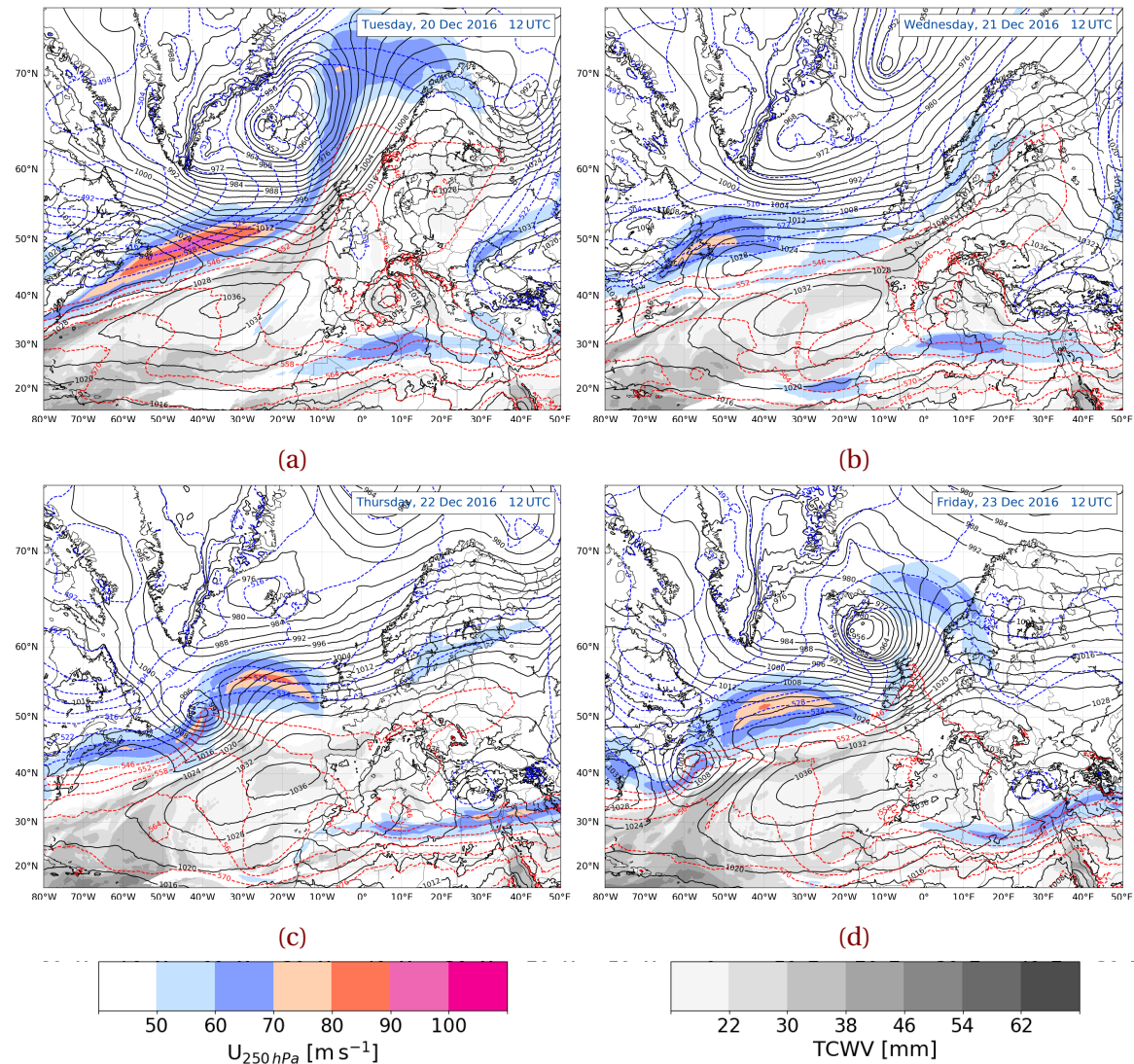


Figure 2.2.1: Dynamic tropopause analysis map, data from ECMWF at 2 PVU. During 20 December 2016 to 27 December 2016. Potential temperature [K] at the 2 PVU surface, shaded according to the colour bar. Total wind, barbs [m s^{-1}], and 925–850 hPa layer-averaged surface relative vorticity (black contours, every $0.5 \times 10^{-4} \text{ s}^{-1}$).

2.3 THICKNESS, SEA LEVEL PRESSURE, MOISTURE, AND WIND AT 250 hPa

A good overview gives the sea level pressure, 1000 – 500 hPa thickness map and winds at 250 hPa. Figure 2.3.1 shows, that it combines several important features of the vertical distribution within the atmosphere, for example.

Black contour lines indicate sea level pressure in hPa and makes it possible to observe cyclones and anticyclones at the sea surface.



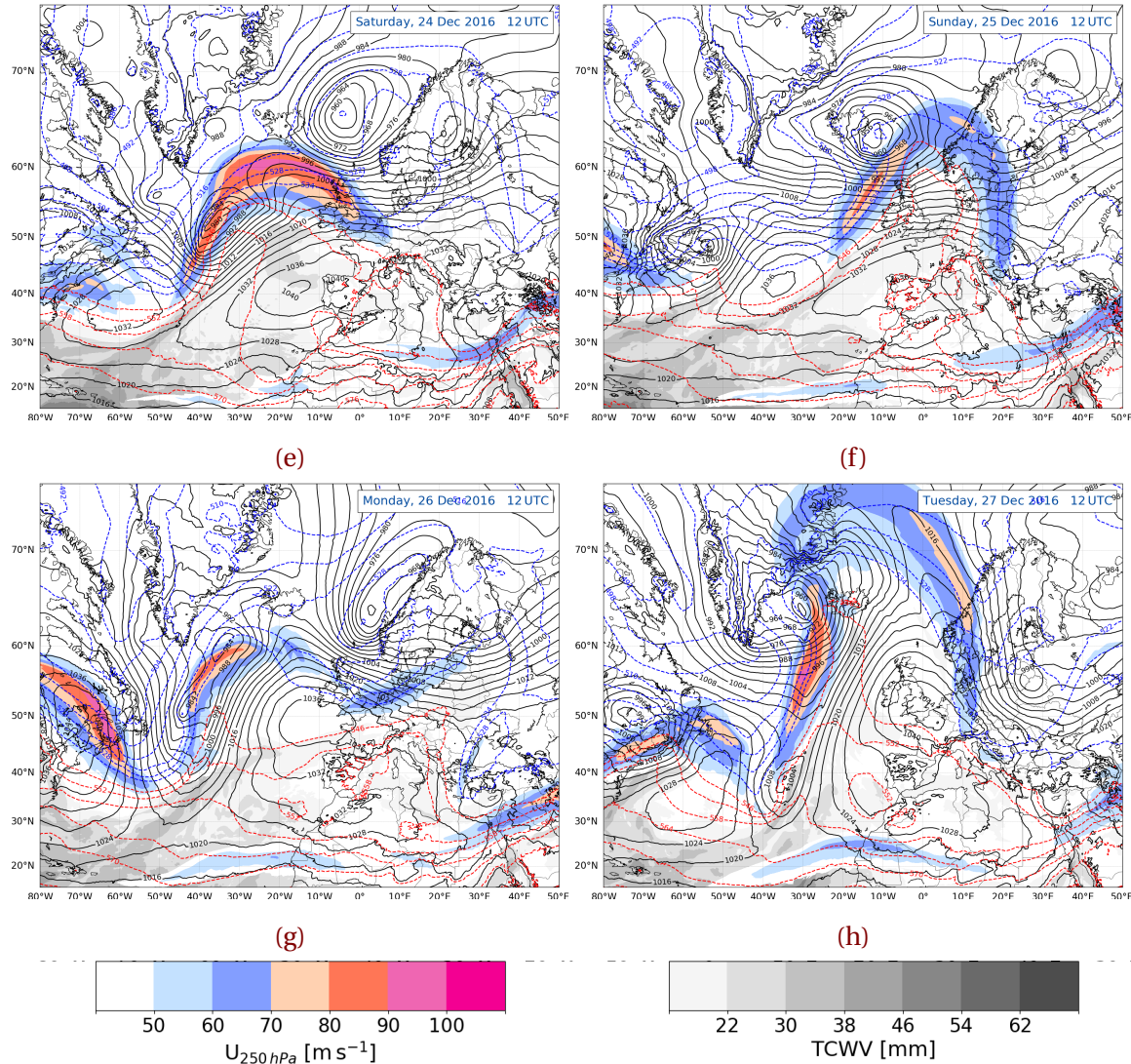


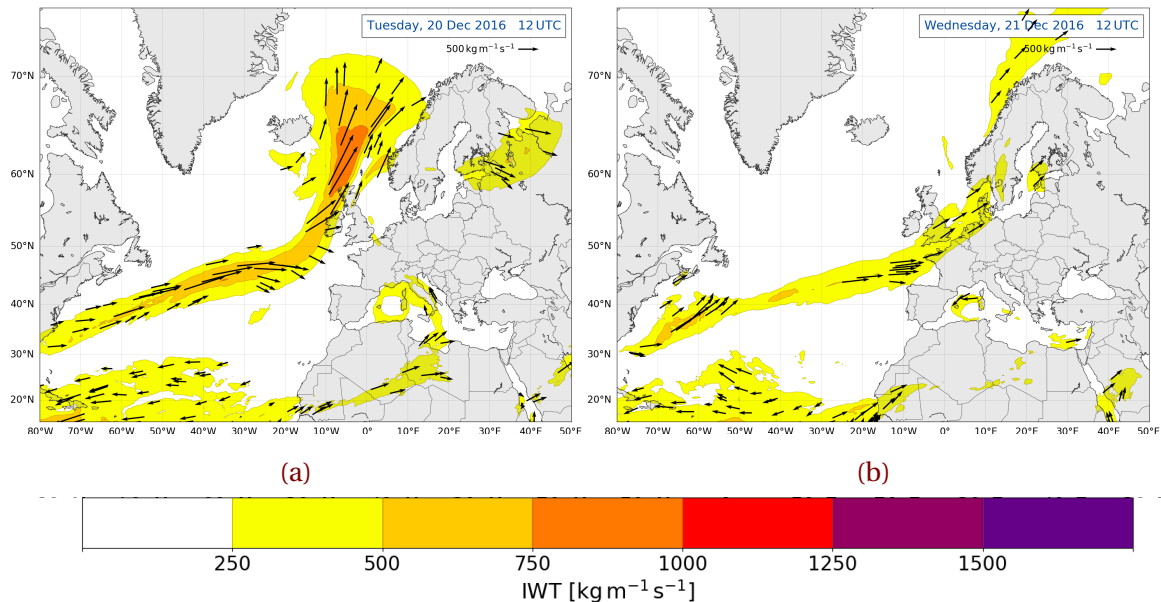
Figure 2.3.1: Jet, thickness, mean sea level pressure, and moisture synoptic analysis, data from ECMWF. During 20 December 2016 to 27 December 2016. 250 hPa wind speed, shaded according to the colour bar, $[\text{m s}^{-1}]$. 1000–500 hPa thickness, dashed contours every 6 dam, MSLP, black contours every 4 hPa, total column water vapour [mm], shaded according the grey scale.

The dashed, coloured contours show the vertical thickness between the 1000 hPa and 500 hPa surface, every 6 dam. The thickness between two pressure levels can be related to the hypsometric equation (Equation (3.4.3)). This is a relation of the mean temperature of the air between two pressure levels. Thus, high values of thickness mean relative warm, moist air (red, dashed). This can then be associated to rain or snow in mid-latitudes, depending on cold or warm air advection.

Gray shaded areas describe total precipitable water in the atmosphere in mm. It is an indicator for the amount of moisture to supply rainfall, and will be used to identify where moisture was present.

Colour shaded contours in Figure 2.3.1 indicate the mid-latitude jet streaks at 250 hPa. Warmer colour is associated with higher wind speeds at this level.

2.4 ATMOSPHERIC RIVER MAP



An atmospheric river (AR) is a filament structure of intense moisture transport from the tropics to higher latitudes. Heavy precipitation can be associated with it, because the air is warm and moist. This can often be observed at mountain ranges at west coasts such as in Norway [include reference here](#). Due to orographic lifting will the moisture be released and follow high amounts of precipitation.

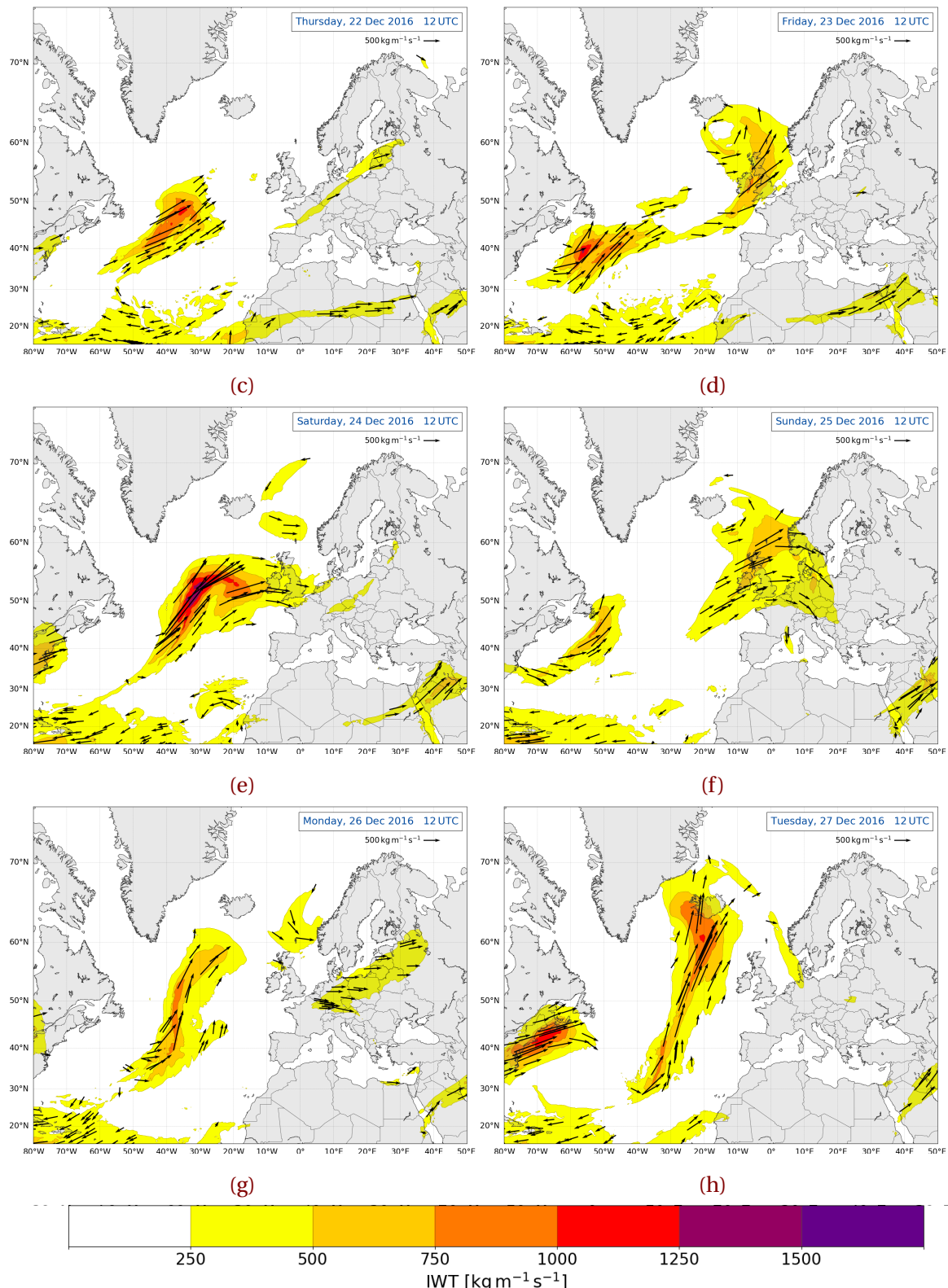


Figure 2.4.1: Atmospheric river analysis map, data from ECMWF. During 20 December 2016 to 27 December 2016. IVT, shaded according to the colour bar [$\text{kg m}^{-1}\text{s}^{-1}$]. Vectors, indicating the direction and magnitude of the IVT.

An atmospheric river is characterised if the integrated vapour transport shows values higher than $250 \text{ kg m}^{-1} \text{ s}^{-1}$ and is a continuous region larger than 2000 km [Rutz et al., 2014]. The integrated vapour transport (IVT) was calculated from the ECMWF data as followed:

$$IVT = \frac{1}{g} \int_{p_{sfc}}^{100 \text{ hPa}} q \mathbf{V} dp \quad [\text{kg m}^{-1} \text{ s}^{-1}] \quad (2.4.1)$$

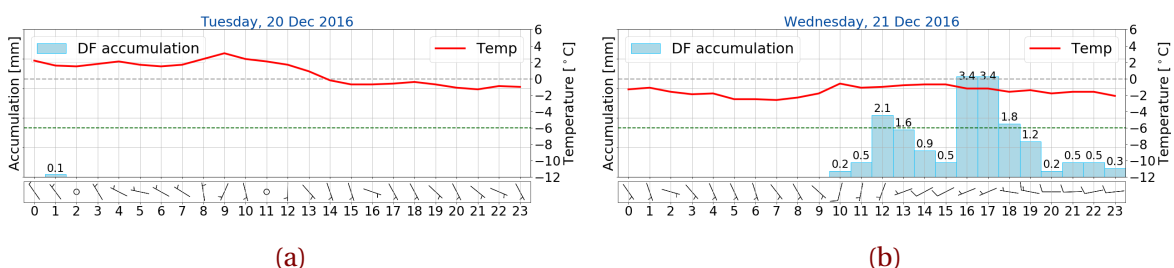
where g is the standard gravity, q the specific humidity, and \mathbf{V} the total wind vector at each pressure level p . The numerical, trapezoidal integration is performed by using data from the surface pressure p_{sfc} to 850 hPa in 50 hPa intervals and from 700 hPa to 100 hPa in 100 hPa intervals.

Figure 2.4.1 shows coloured contours of the integrated vapour transport (IVT) in $\text{kg m}^{-1} \text{ s}^{-1}$, where warmer colours indicate higher IVT. Stream vectors indicate the direction and intensity of the IVT flow.

2.5 OBSERVATIONS AT THE WEATHER MAST

The large scale synoptic analysis will be related to the local weather observations at Haukeliseter.

60 min accumulation is presented as bars in Figure 2.5.1 and will show the continuous precipitation at Haukeliseter during the extreme event. The possible change of precipitation will be investigated with the temperature. Snow fall is likely for temperatures up to 2°C . The intensity of the storm can be classified by the hourly averaged wind speed and direction as wind barbs in m s^{-1} . To understand which damage a storm can have, Færæas et al. [2016] released a table to associate wind strength with damage (see Table 2.5.1).



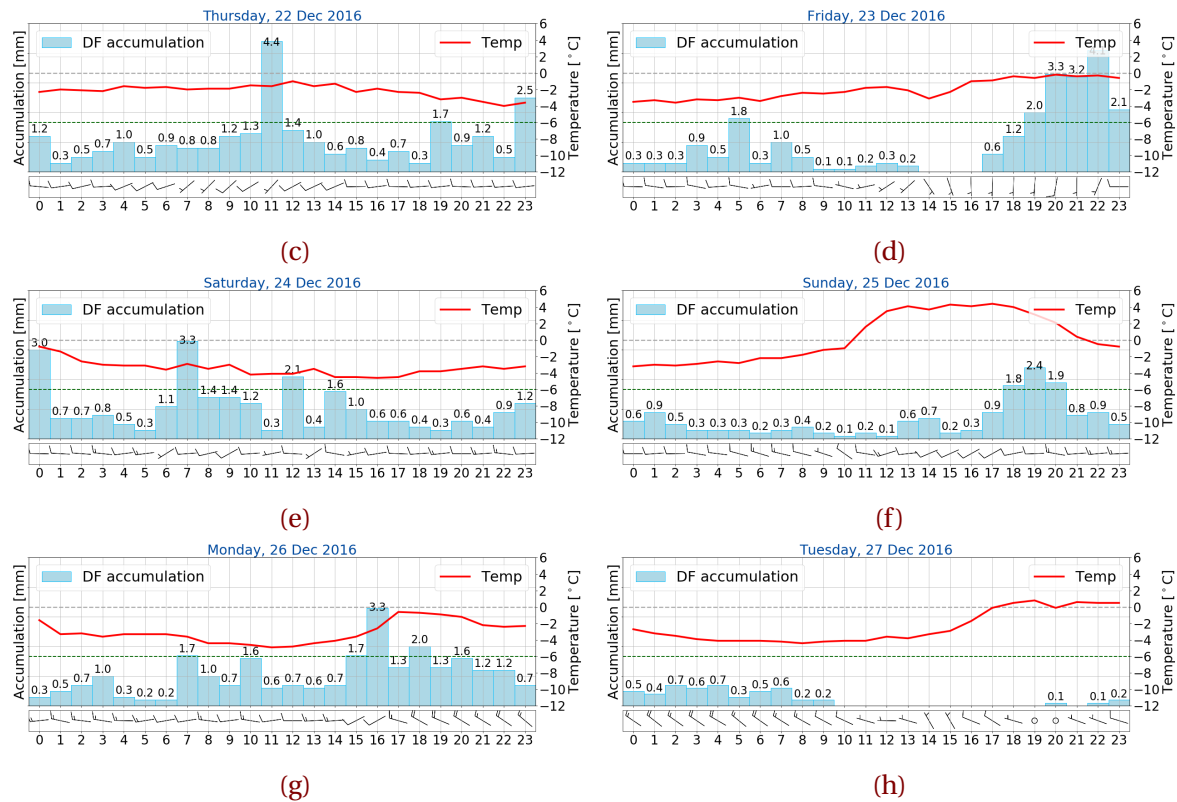


Figure 2.5.1: Observation from the weather mast at Haukeliseterd during 20 December 2016 to 27 December 2016. 60 min total accumulation [mm] in light blue as bar, temperature (red, $^{\circ}\text{C}$), and wind as barbs [m s^{-1}]. Gray dashed line indicates the freezing temperature and the green dashed line the 30-year climate mean temperature at -6°C . Hourly processed data taken from [eklima \[2016\]](#).

Table 2.5.1: Damage related to wind speed, from Færaas et al. [2016].

slight storm	$20.8 \text{ ms}^{-1} - 24.4 \text{ ms}^{-1}$	Large trees sway and hiver. Roofs can blow down.
full storm	$24.5 \text{ ms}^{-1} - 28.4 \text{ ms}^{-1}$	Trees are pulled up with clutter. Big damages to houses.
strong storm	$28.5 \text{ ms}^{-1} - 32.6 \text{ ms}^{-1}$	Extensive damage.
hurricane	$>32.6 \text{ ms}^{-1}$	Unusually large destruction.

2.6 RADIOSONDE FROM STAVANGER

The Appendix A.1 includes images of vertical temperature profiles of Radiosondes from Stavanger, represented in a Skew-T log-P diagram. The vertical profiles extend from surface up to 300 hPa. (Note, that the representation of the vertical scale (in m) differs with each sounding from day to day.)

The vertical temperature distribution will identify the stability of the atmosphere and give information on convection and thickness of clouds. Furthermore, warm air and cold air advection can be identified by observing the change of wind with height.

Black and green line represent the atmospheric and dew-point temperature, respectively.

2.7 LARGE SCALE CIRCULATION

Everything has to get into relation with the Radiosondes, Figure A.1.1. How to do that? Any suggestions? They took me some time to make, so I want to include them!

21 December 2016

The dynamic tropopause map in Figure 2.2.1b shows that Norway is influenced by a change of elevated tropopause to a suppressed tropopause during 20 December 2016 to 21 December 2016. Hence the potential vorticity changed from positive to negative at the tropopause and cold air stretches right over Norway. A good amount of moisture is

transported from the low latitudes to high latitudes, influencing Norway's west coast. This can be seen in the surface maps (Figure 2.3.1b) as well as in the atmospheric river maps (Figure 2.4.1b). The westerly flow in Figure 2.3.1b is conducive to orographic lifting. The precipitation was probably snow when having a look at the moisture content and the cold air. The change from warm air to cold air can also be observed in the time series of temperature in Figure 2.5.1b. And the westerly flow, combined with a good amount of vapour transport from the tropics led to orographic lifting and precipitation at the Haukeliseter site. At around 60°W a formation of a cyclone at the baroclinic zone can be implied.

22 December 2016

Twenty-four hours later the analysis shows from 22 December 2016 phasing between the surface relative vorticity and the baroclinic zone at 50°N in the DT. The centre of the surface low is directly located below the temperature gradient at the 2 PVU surface, hence this is good for synoptic lifting. Furthermore, the strongest baroclinicity is observed on the south west side of the surface low. The synoptic map of the geopotential thickness and the surface pressure show the beginning of the frontal boundaries in Figure 2.3.1c. At the same time shows the AR map, Figure 2.4.1c, large values just at the baroclinic zone, where the low pressure is beginning to form. **Help?! Does that lead to even more lifting in this area? Or does it just mean that the cyclone gets a good amount of moisture?!**. Norway is located in a cold area. The continues precipitation observed at Haukeliseter (Figure 2.5.1c) is associated with the westerly flow which is conducive to orographic lifting, and therefore moisture release.

23 December 2016

The begin of the ridging on the 22 December 2016 is more pronounced 24 h later. The warmer air pushes away the cold air, which covered Norway. The low pressure system moved north-east, and lies south of Iceland. The occluded front of this system passes through Haukeliseter, which is why a temperature 'jump' observed at 14 UTC. After this, Southern Norway is influenced by the warm sector, monitored as a temperature increase. The AR, as well as the total column water vapour amount in Figure 2.4.1d and Figure 2.3.1d,

respectively show the amount of moisture, transported from low latitudes.

At the same time forms a second cyclone at the baroclinic zone at 40° N. The atmospheric river map (Figure 2.4.1d) indicates a large amount of moisture at this latitude. Again, moist, warm air is conducive to intensify the surface cyclone. In addition, shows the DT map a phasing between the low level vorticity and the upper level baroclinic zone.

24 December 2016

After the passage of the cold front over Norway, Scandinavia is within colder air (compare Figure 2.2.1e and Figure 2.3.1e for 24 December 2016). Over the Atlantic warmer air starts to push the colder air northward. **something something with the low level vorticity and lifting; lifting at the right entrance region of the jet streak, and very high IVT.**

At Haukeliseter negative temperature up to -4°C is observed, compare Figure 2.5.1e. The westerly flow is again conducive for orographic lifting and associated precipitation.

25 December 2016

Twenty-four hours later the ridge is more pronounced and covers large parts of Norway. The surface low south-east of Iceland has build its frontal boundaries, which can be seen in the low-level vorticity of Figure 2.2.1f. The warm front lies west of Haukeliseter and starts to be observed at the measurement site (compare Figure 2.5.1f for 25 December 2016). Figure 2.4.1f indicating the integrated vapour transport shows that a lot of moisture is transported from the Atlantic, towards Great Britain and south-western Norway. Together with the lifting at the surface boundary a sufficient amount of precipitation is observed. Since the ridging brings more moist (Figure 2.4.1f), warm air (Figure 2.2.1f) and Norway lies in a warm sector (Figure 2.3.1f) the assumption will be made, that the precipitation changed from solid to liquid.

26 December 2016

Within the next twenty-four hours the cold front passed through (temperature change in Figure 2.5.1g for 25 December 2016 to 26 December 2016). Norway is covered in cold air (Figure 2.2.1g). The surface low-level indicates the occlusion of the cyclone and therefore a weakening. The wind is still from the west which is helpful for orographic lifting. The

moisture content is still present but much weaker and smaller in extend. Since Norway is covered in cold air, the temperature is below zero and the precipitation had to be solid.

27 December 2016

The images of 27 December 2016 show that the storm passed and disappeared. Southern Norway lies in cold air (Figure 2.2.1h), but on the right exit region of the jet (\rightarrow sinking motion of cold air), compare 2.3.1h. A small amount of moisture is present (Figure 2.4.1h). Because of the wind change from west to north-west follows that orographic lifting is not present and the precipitation amount decreases at the end of the storm.

CHAPTER 3: INSTRUMENTATION, DATA, AND METHODOLOGY

This chapter describes the instruments, the optimal estimation retrieval and the regional forecast model used in the scope of this study, to determine the snow water content in the vertical. The determination of required parameters from the measuring instruments in relation to the optimal estimation retrieval will be explained. The purpose of this study is to compare the vertical observations from the Haukeliseter measurement site and the output from the operational forecast model at the Norwegian Meteorological Institute for the extreme weather event during Christmas 2016. The last section will give an insight on how the data was analysed to compare the different systems.

3.1 INSTRUMENTS

Many factors such as humidity and temperature contribute to snowflake geometry. The knowledge of snowflake habits, particle size distributions, and fall speed lead to a reduction of errors in optimal estimation retrievals.

This work is based on several datasets collected at the Haukeliseter measurement site, 59.8° N, 7.2° E. A composition of advanced ground based observations and the CloudSat precipitation retrieval will help to get a better understanding of the vertical structure of the atmosphere.

A collaboration between the University of Utah, University of Wisconsin and Met-Norway made it possible to install three additional instruments at the measurement site during winter 2016/2017. A Multi-Angle Snowflake Camera (MASC) and a Precipitation Imaging Package (PiP) will be used to determine the snow habit, the snowfall particle size distribu-

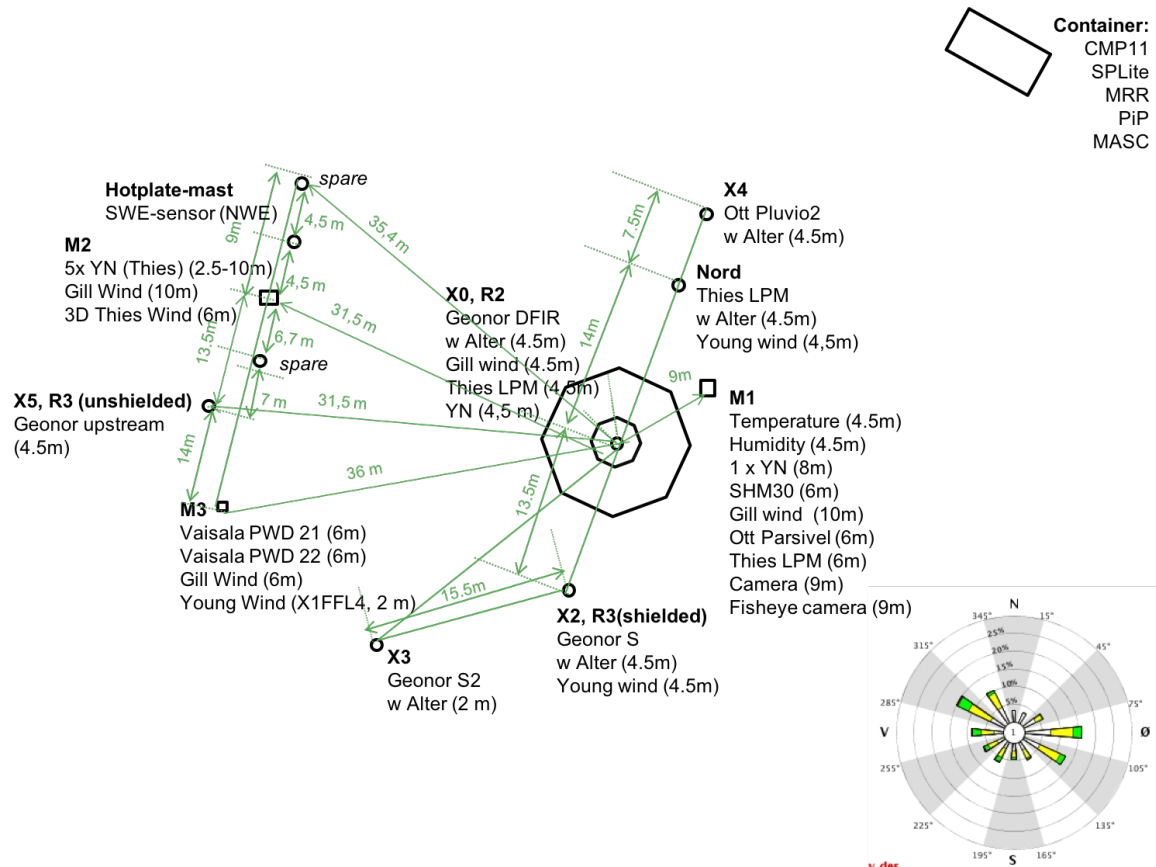


Figure 3.1.1: Instruments at the Haukeliseter measurement site during winter 2016/2017 [adapted from Wolff et al., 2015]. The windrose indicates the mean wind direction from either from west-north-west or east-south-east.

tion, and near-surface fall speed. Additionally, a Micro Rain Radar (MRR) is established to obtain fall speed and particle reflectivity aloft. Together with temperature observations at the surface, is this a good basis to reduce the non-uniqueness of snow accumulation in optimal estimation snowfall retrieval, described in Section 3.2.

A sketch of the instrumentation setting is presented in Figure 3.1.1. The octagonal indicates the double fence. The container is north-east from the double fence having the MRR, MASC and PiP mounted at the top. M1 in Figure 3.1.1 is the 10 m weather mast, providing the hourly [eklima \[2016\]](#) temperature and wind measurements. The mean wind direction from west-north-west and east-south-east are shown in the windrose in Figure 3.1.1.

3.1.1 DOUBLE FENCE

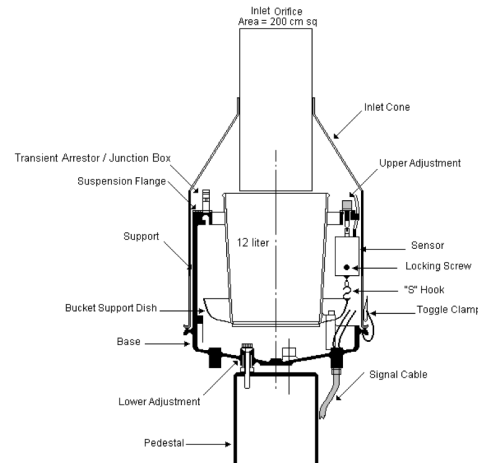
Since the winter season 2010/2011 Haukeliseter is equipped with several precipitation gauges. The wind shielded gauges are placed perpendicular to the main wind direction (E/W wind). The precipitation gauge protected by an octagonal double fence (Figure 3.1.2a) will be the reference to all surface accumulation measurements. The double fence creates an artificial calm wind and maximize the catch of precipitation, [Wolff et al., 2010, 2013, 2015]. The wind inside the double fence is measured to be not much higher than 5 m s^{-1} even if the winds outside exceed 20 m s^{-1} (occurred 26 December 2016). For now, it is presumed that the average undercatch inside a double fence is 20 % for wind speeds between 10 m s^{-1} and 20 m s^{-1} and 10 % for wind speeds under 9 m s^{-1} [Wolff, 2018].

Inside the double fence is a precipitation-weighing gauge Geonor T-200B3 [3-wire transducers, 1000 mm, Geonor Inc., 2015] with a Alter wind screen to reduce wind turbulence around the gauge. At Haukeliseter is the orifice height of the Geonor 4.5 m above the ground. This is due to an expected snow depth of 2 m to 3 m during a winter season and to reduce the likelihood of measuring drifting snow [Wolff et al., 2013, 2015].

A vertical cross section of the T-200B gauge is shown in Figure 3.1.2b. Precipitation particles fall through the 200 cm^2 orifice protected with a heated collar, into a cylindric bucket filled with frost protection. The bucket is placed on top of a Bucket Support Dish [Figure 3.1.2b, Geonor Inc., 2015]. This dish is connected with three wire sensors having an eigenfre-



(a)



(b)

Figure 3.1.2: a: Double fence and unprotected precipitation gauges at Haukeliseter, from Wolff et al. [2015]. The prevailing wind direction from east comes from the lower, left corner in the image and the west wind from the opposite site. b: Vertical cross section of T-200B precipitation gauge [Geonor Inc., 2015].

quency changing with the weight inside the bucket. A formula provided by [Geonor Inc. \[2015\]](#) calculates the amount of precipitation from the frequency of each sensor. The three sensors provide a reduction of an error in connection with an unlevel installation. Met-Norway will average value of all three sensors and provide it as hourly data at [eklima](#).

3.1.2 MRR - MICRO RAIN RADAR

Radars are very useful to observe the vertical of the atmosphere. The instrument is able to detect mesoscale features and makes it possible to see the vertical structure of storms [[Markowski and Richardson, 2011](#)].

The principle of radar measurements is based on an electromagnetic wave, which is emitted from the radar transmitter and interacts with the hydrometeors along the beam. A fraction of the pulse energy is reflected back to the receiver of the radar. The quantity of scattering depends on the shape and structure of the reflected particle. Vertical profiles of reflectivity give information about the diameter of the target object.

The Micro Rain Radar, in Figure 3.1.3, measures profiles of Doppler spectra [[METEK, 2010](#)]. The Doppler spectrum tells about the movement of the particle. The vertical pointing Doppler radar measures the energy that is returned from each interval and thus enabling the detection of the Doppler spectrum [[L'Ecuyer, 2017](#)]. The MRR measures at a frequency of 24 GHz, and has a temporal and spatial spatial resolution of 60 s and 100 m, respectively. The radar height range is from 100 m (because of ground clutter) to 3.000 m [[METEK, 2010](#)]. MRR radar reflectivity (Z) is transformed from $1 \text{ mm}^6/\text{m}^3$ to dBZ. The transformations is done with the following relationship;

$$Ze = 10 \log_{10} \left(\frac{Z}{1 \text{ mm}^6/\text{m}^3} \right) \quad [\text{dBZ}] \quad (3.1.1)$$



Figure 3.1.3: Micro Rain Radar.

A transformation to rainfall rates can be performed by the $Z-R$ (reflectivity - rainfall) relationship. The rainfall rate in each layer can be estimated by the use of typical fall speeds and the Marshall-Palmer particle size distribution for liquid particles [[Rinehart,](#)

2010].

$$Z = 200R^{\frac{8}{5}} \quad [\text{mm}^6\text{m}^{-3}]$$

$$R = \left(\frac{10^{\frac{Ze}{10}}}{200} \right)^{\frac{5}{8}} \quad [\text{mmh}^{-1}] \quad (3.1.2)$$

Table 3.1.1 represents the Z-R relationship if the Marshall-Palmer assumption (Equation (3.1.2)) is applied. Z-snowfall relationships are developed but are difficult to apply due to the variation of size and density of the particles [L'Ecuyer, 2017].

After the transformation to dBZ the reflectivity is averaged for every 200 m layer thickness, where only values above 300 m are taken. For instance, a reflectivity at 400 m represents the mean value of reflectivity between 300 m and 500 m.

Table 3.1.1: Typical reflectivity values, from Doviak and Zrnic [1993]. The values are obtained from measurements, models and observations. The rainfall rate R is calculated with Equation (3.1.2).

	Ze [dBZ]	R [mm h ⁻¹]
Drizzle	<25	1.3
Rain	25 to 60	1.3 to 205.0
Snow		
dry, low density	<35	5.6
Crystal; dry, high density	<25	1.3
wet, melting	<45	23.7
Graupel		
dry	40 to 50	11.5 to 48.6
wet	40 to 55	11.5 to 99.9
Hail		
small; <2 cm, wet	50 to 60	48.6 to 205.0
large; >2 cm, wet	55 to 70	99.9 to 864.7
Rain & Hail	50 to 70	48.6 to 864.7

3.1.3 PiP - PRECIPITATION IMAGING PACKAGE

The precipitation imaging package (PiP) is a modification of the Snowflake Video Imager presented by [Newman et al. \[2009\]](#). The video distrometer is a construct of a halogen flood lamp and a video system (Figure 3.1.4). The instrument determines the habit of snowflakes from images at a frequency of 60 Hz. Lamp and lens have a distance of approximately 3 m which follows a field of view: 32 mm by 24 mm.

In front of the halogen lamp is a frosted window, so that the background light is uniform over all time. A falling particle appears as a 2-D shadow in the video image. Particle size distribution (PSD) and fall speed of precipitation can be determined from the black and white images of the system. [Newman et al. \[2009\]](#) describes in detail the algorithm applied to the system to get information about the snow-particle habit.

Winds have almost no effect on the result of the video distrometer [[Newman et al., 2009](#)]. They also say, to reduce eventual wind effects, should the distrometer be oriented with regard to storm winds (optical axis perpendicular to mean wind). Was that the case for Haukeliseter (I'm just curious)???



Figure 3.1.4: Precipitation Imaging Package.

3.1.4 MASC - MULTI-ANGULAR SNOWFALL CAMERA

Instruments like the afore mentioned PiP has according to [Garrett et al. \[2012\]](#) coarser resolution and the determination of particle size can have larger errors. Hence, a new instrument was developed. The Multi-Angular Snowfall Camera (MASC) takes high-resolution images of hydrometeors in free fall and measures the fall-speed simultaneously.

The MASC consists of three cameras, three flashes, and two near-infrared sensors, pointing at a ring centre (Figure 3.1.5). A hydrometeor has to pass through the ring in a certain way to trigger the near-infrared sensors. At the same time the three cameras take a picture of the falling particle. Since the cameras take pictures from three different angles, the particles size, shape, and orientation can be specified from an algorithm applied to the image, described in [Garrett et al. \[2012\]](#). Furthermore, the form and heritage of the hydrometeor, such as collision-coalescence, riming, capture nucleation, or aggregation, can be determined. The near-infrared sensor, that is used to trigger the cameras and the lights quantifies the fall-speed of the hydrometeors, by measuring the time the particle needs to pass the distance between the upper and lower trigger.

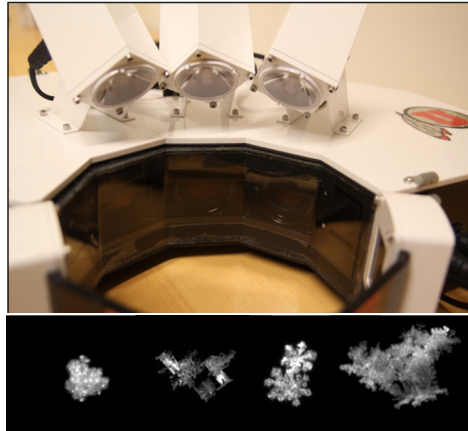


Figure 3.1.5: MASC and images taken by instrument. Lower panel taken from [Cooper et al. \[2017\]](#) maybe we get one for Haukeli?

3.2 OPTIMAL ESTIMATION RETRIEVAL ALGORITHM

Since 2006, with the launch of CloudSats Cloud Profiling Radar (CPR) a global estimation of snowfall can be done. Several studies, such as [Kulie and Bennartz \[2009\]](#) have shown that estimated snowfall values depend heavily upon assumed snowflake microphysical properties. [Wood et al. \[2015\]](#) showed that a refinement of the CloudSat snowfall retrieval algorithm can be performed by using snowflake models. This study was based on data from the Canadian CloudSat-CALIPSO Validation Project [C3VP, [Hudak et al., 2006](#)], where they concentrated on cold season clouds and precipitation.

In an attempt to reduce the non-uniqueness of the problem, [Wood et al. \[2015\]](#) used the a priori knowledge of snowfall microphysics and temperature (from ground-based observations) to refine the forward-model assumptions for the CloudSat snowfall retrieval scheme. Results from this scheme showed a good agreement with reported values observed at meteorological measurement sites.

Model estimates have proven, how useful the estimation retrieval can be to verify ground-based radar snowfall measurements [[Norin et al., 2015](#)]. Although the retrieval has obviously been improved the estimation algorithm, a priori guess can still lead to uncertainties in the retrievals of up to 140 % to 200 % [[Wood, 2011](#)].

[Cooper et al. \[2017\]](#) developed a technique to combine MRR, MASC, and PiP information into a common retrieval framework. Specifically, estimates of snowflake microphysical properties from the MRR are used as the a priori term in the optimal-estimation retrieval scheme. The usage of either MASC/PiP or MRR fall-speed can show which a priori guess in the retrieval gives the more accurate retrieved snowfall rate at the ground.

The difference between the retrieval and the snow gauge observations was –18 % when applied to data from Barrow, Alaska.

[Cooper et al. \[2017\]](#) also showed that the retrieval is sensitive to habit and fall speed. The installation of a MRR, MASC, and PIP should help to adjust the particle models for graupels and rimed particles which are often observed at Haukeliseter.

3.2.1 FORWARD MODEL

Forward model defines a relationship between the radar observations and the retrieved state vector \mathbf{x} . It is difficult to find the properties of the atmosphere by using observations due to unknown parameters influencing the measurement.

Stephens [1994] described the forward problem in the manner that a Dragon represents the known source, observations Figure 3.2.1. The amount of received radiation lost during the transmittance to the sensor is unknown, the Tracks in Figure 3.2.1. The forward model will help to find simulated observations before the attenuation took place and give information about the tracks of the dragon.

The knowledge about the a priori parameters and related covariances, as well as \mathbf{x} , are used to minimize Equation (3.2.7). The values of \mathbf{x} are found by Newtonian iteration [Wood et al., 2014, Eq. 5].

The snow water content in each layer is estimated from the knowledge of the snow particle mass-dimension relationship in Appendix B.1, and a PSD related to slope parameter and number concentration (Equations (3.2.12–14)).

$$\text{SWC} = \int_{r_{min}}^{r_{max}} m(r) n(r) dr \quad [\text{gm}^{-3}] \quad (3.2.1)$$

To achieve a relationship between the reflectivity and the snowfall amount one needs to account for attenuation in the atmosphere. Using the previously calculated PSD (Equation (3.2.12)) the backscattering cross-section σ_{bk} , one can estimate the reflectivity for Rayleigh approximated, singly-scattered non-attenuated ice particles [Kulie and Bentartz, 2009, L'Ecuyer and Stephens, 2002, Wood et al., 2015]. The Rayleigh approximation

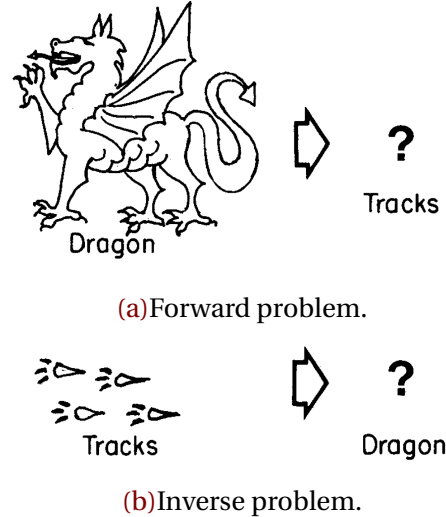


Figure 3.2.1: a Relationship between measurements (dragon) and the unknown parameter of interest (tracks), and b presenting the inverse problem when the parameter of interest is known but measurements are not [Stephens, 1994].

assumes, that $2\pi r/\lambda \ll 1$, where λ the wavelength of incident radiation.

$$\begin{aligned}\eta_{bk} &= \int_{r_{min}}^{r_{max}} n(r) \sigma_{bk} dr \quad [\text{m}^{-1}] \\ Ze^{ss,na} &= \frac{\Lambda^4}{\|K_w\|^2 \pi^5} \eta_{bk} \quad [\text{mm}^6 \text{m}^{-3}]\end{aligned}\quad (3.2.2)$$

where, Λ is the wavelength of the radar; $\|K_w\|^2$ is the complex refractive index of water and varies between 0.91 and 0.93 for wavelength between 0.01 m and 0.10 m and is independent of temperature. It also exists a complex refractive index for ice $\|K_i\|^2$, which is 0.18. This is valid for a density of 0.917 g cm^{-3} and is independent of temperature and of wavelength in the microwave region [Doviak and Zrnic, 1993]. In this work $\|K_w\|^2 = 0.93$ is chosen, BECAUSE???.

The singly-scattered reflectivity has to be corrected for attenuation in the layers above the actual layer. According to Beer's law is in a homogeneous medium one way transmission assumed.

$$\frac{I_\lambda}{I_{\lambda_0}} = \exp \left[- \int_0^s \beta_{ext} ds' \right] \quad (3.2.3)$$

where s is the path length through the medium. The transmissivity I_λ/I_{λ_0} is the relation of survived radiation through extinction in the atmosphere with the snow extinction coefficient β_{ext}

$$\beta_{ext} = \int_{r_{min}}^{r_{max}} n(r) \sigma_{ext} dr \quad [\text{m}^{-1}] \quad (3.2.4)$$

The extinction coefficient is the sum of absorption and scattering in the atmosphere followed from the extinction cross-section $\sigma_{ext} = \sigma_{abs} + \sigma_{scat}$, [Lamb and Verlinde, 2011, Lohmann et al., 2016]. [Eq. 12.1 and more Lohmann et al., 2016]

Following Equations (3.2.2–4) the singly-scattered attenuated reflectivity $Ze^{ss,a}$ is

$$Ze^{ss,a} = Ze^{ss,na} \cdot \frac{I_\lambda}{I_{\lambda_0}} \quad [\text{mm}^6 \text{m}^{-3}] \quad (3.2.5)$$

That follows with the use of radiative transfer equations for the simulated reflectivity from the forward model, $F(\mathbf{x})$ in Equation (3.2.7), after the transformation with Equation (3.1.1)

$$F(\mathbf{x}) = \begin{bmatrix} Ze_1^{ss,a} \\ \vdots \\ Ze_{nlayer}^{ss,a} \end{bmatrix} \quad [\text{dBZ}]. \quad (3.2.6)$$

3.2.2 SNOWFALL RETRIEVAL SCHEME

The optimal estimation method is based on Gaussian statistics. Minimizing the scalar cost function, Φ for the snowfall properties, \mathbf{x} . The cost function weights the difference between the observed reflectivity and the simulated measurements as well as the difference between the estimated and a priori guess.

Scalar cost function:

$$\begin{aligned}\Phi(\mathbf{x}, y, a) = & (y - F(\mathbf{x}))^T \mathbf{S}_y^{-1} (y - F(\mathbf{x})) \\ & + (\mathbf{x} - a)^T \mathbf{S}_a^{-1} (\mathbf{x} - a)\end{aligned}\quad (3.2.7)$$

where, \mathbf{x} , vector of retrieved snowfall properties (Equation (3.2.15)); y , vector of observation (MRR reflectivity); a , vector of the a priori guess (temperature dependent); \mathbf{S}_a , a priori error covariance matrix; \mathbf{S}_y , measurement error covariance matrix. The forward model $F(\mathbf{x})$, presented in Section 3.2.1 relates unknown snowfall parameters \mathbf{x} to radar observations y and approximates the true physical state between them [Cooper et al., 2017, Wood et al., 2014].

\mathbf{S}_a links the uncertainties of the PSD information and the surface temperature differences. The diagonal matrix elements in \mathbf{S}_a are equal to 0.133 and 0.95 for the particle slope parameter and the number concentration, respectively as from Eq. 7.35 and 7.36 in Wood [2011].

\mathbf{S}_y characterises the the uncertainties associated with the measurements and the error in the forward model. This study uses for the diagonal matrix elements 2.5² UNIT! based on the study from CITATION. BECAUSE.

I don't understand the next steps and if it is still the same \mathbf{x} !

At convergence is the error covariance of the retrieved state vector \mathbf{S}_x

$$\mathbf{S}_x = \left(\mathbf{S}_a^{-1} + \mathbf{K}^T \mathbf{S}_y^{-1} \mathbf{K} \right)^{-1} \quad (3.2.8)$$

which follows for \mathbf{x}

$$\mathbf{x} = \underbrace{\left(\mathbf{S}_a^{-1} + \mathbf{K}^T \mathbf{S}_y^{-1} \mathbf{K} \right)^{-1}}_{\mathbf{S}_x} \left(\mathbf{S}_a^{-1} \mathbf{a} + \mathbf{K}^T \mathbf{S}_y^{-1} (y - F(\mathbf{x}) + \mathbf{K}\mathbf{x}) \right) \quad (3.2.9)$$

The Jacobian matrix, \mathbf{K} , represents the sensitivity matrix of the perturbed result of the forward model. The true state \mathbf{x} is perturbed by $\pm 0.2\%$ and thus \mathbf{K} represents the relation

between simulated values to the true state and how sensitive the simulated values are to small changes when starting a new retrieval cycle. The closer \mathbf{K} is diagonal, the more is \mathbf{x} determined by the real observed and a priori values. If the limit of the partial derivative is close to unity, the retrieved value \mathbf{x} is its true state [Wood, 2011].

mmmh? What exactly are we doing here? Test the if convergent:

$$\hat{x} = (\mathbf{x} - F(\mathbf{x}))^T \mathbf{S}_x^{-1} (\mathbf{x} - F(\mathbf{x})) \quad (3.2.10)$$

only if \hat{x} is smaller than 2 it is a 'good' retrieval.

To test the result of \mathbf{x} a χ^2 test is performed at the convergence of \mathbf{S}_x .

$$\begin{aligned} \chi^2 = & (F(\mathbf{x}) - y)^T \mathbf{S}_y^{-1} (F(\mathbf{x}) - y) \\ & + (\mathbf{x} - a)^T \mathbf{S}_a^{-1} (\mathbf{x} - a). \end{aligned} \quad (3.2.11)$$

The first term in Equation (3.2.11) measures the part of χ^2 related to the noise of the forward model, and the second part the relation to the state vector. Thus the second term describes the accuracy of the quantities within the reflectivity and temperature measurements [Rodgers, 2000]. Furthermore, are the error contribution from the reflectivity measurement uncertainty, \mathbf{S}_{y_e} , and the uncertainty of the a priori values, \mathbf{S}_{a_e} estimated.

3.2.3 PRESENCE OF SNOW

To achieve vertical profiles of snowfall from MRR different steps and assumptions are done in the here presented snowfall retrieval. From one of the lower levels, the snowfall rate at the surface can be estimated. The retrieval is only performed for profiles, which are likely to have observed snow, where most retrievals use rain. In previous studies relationships between reflectivity and snowfall have been developed. Even if the PSD of ice particles is known, different crystal shapes led to different results. Snow densities vary significantly from storm to storm, where small particles are still Rayleigh scattered, and larger particles non-Rayleigh scattered [Gunn and East, 1954].

To obtain the likelihood of present snow a reflectivity threshold of -15 dBZ is used. This threshold is similar to the one used in Wood et al. [2013], where it states that light liquid precipitation is related to -10 dBZ [Stephens and Wood, 2007]. Wood [2011] compared the reflectivity in the lowest bin and adjacent bin and found, that the reflectivity above

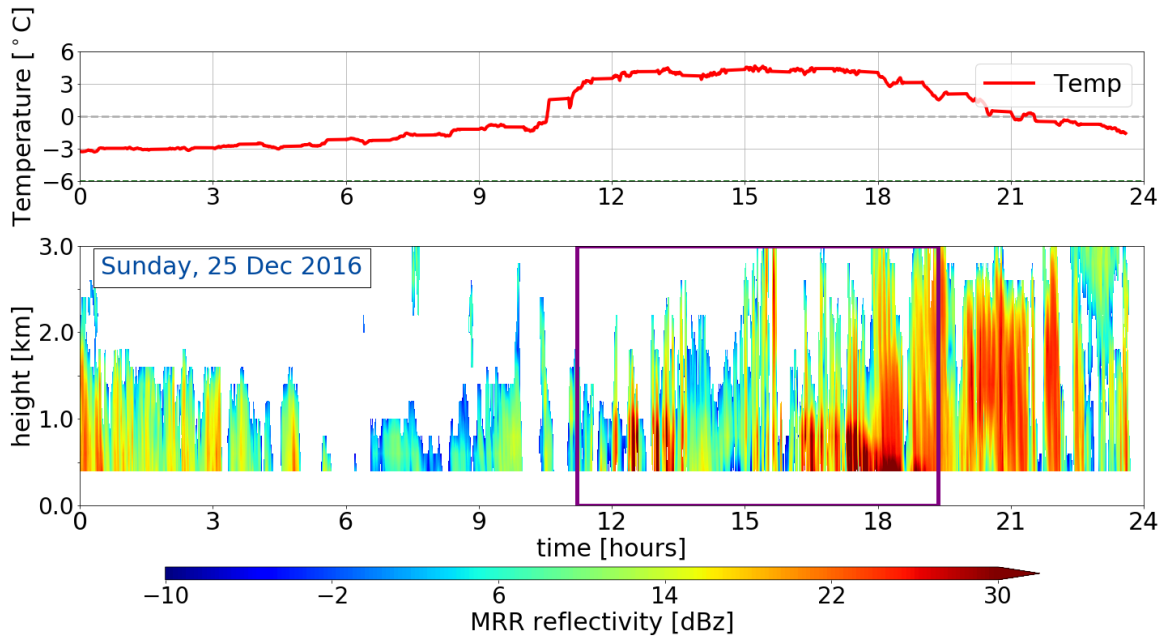


Figure 3.2.2: Shows the a priori temperature dependence within the optimal estimation retrieval for an all day precipitation event on 25 December 2016. The upper panel shows T_{ap} measured at the Haukeliseter site. The lower panel presents the reflectivity from the MRR in addition indicates the purple frame the time, where the MRR reflectivity was larger than -10 dBZ and surface temperatures less than 2°C

-15 dBZ are not influenced by ground clutter.

The Haukeliseter measurement site is equipped with a weather mast, measuring the air temperature every minute at two meter height (compare Figure 3.2.2, upper panel). Since the MRR measures above 300 m and only temperature measurements at the surface exists, a priori temperature (T_a) is assumed to be similar to the observed near-surface air temperature. Using a moist adiabatic lapse rate of $dT/dz = 5 \text{ K km}^{-1}$ gives T_a in each layer. Assuming snow exists at temperature measurements up to a threshold of 2°C , validated by Liu G. [2008] who analysed present weather reports to find the distinction between liquid and solid precipitation.

The purple line in the lower panel of Figure 3.2.2 represents the time frame during 25 December 2016, where the MRR reflectivity is less than -15 dBZ , and a priori temperature passes the 2°C limit at the surface.

3.2.4 SIZE DISTRIBUTION

To determine the snowfall rate at the surface an exponential particle size distribution (PSD) is needed.

$$n(r) = N_0 \exp(-\lambda r) \quad [\text{m}^{-3} \text{ mm}^{-1}] \quad (3.2.12)$$

where λ represents the PSD slope parameter and N_0 the number concentration. r is the particle maximum dimension evaluated from the 2D-scattering model for branched 6-arm spatial particles with porosities for reflectivity measurements at 24 GHz (see Appendix B.1). Since T_a varies with a moist adiabatic lapse rate in each layer bin the slope parameter and the number concentration in Equation (3.2.12) are changing too. Wood [2011] showed a linear fit between $\log(\lambda)$ and the a priori temperature, respectively $\log(N_0)$ and the a priori temperature. Using T_a in °C for each layer bin the following logarithmic assumption is used, to define the slope parameter and the number concentration.

$$\log(\lambda) = -0.03053 \cdot T_{ap} - 0.08258 \quad [\log(\text{mm}^{-1})] \quad (3.2.13)$$

$$\log(N_0) = -0.07193 \cdot T_{ap} + 2.665 \quad [\log(\text{m}^{-3} \text{ mm}^{-1})] \quad (3.2.14)$$

To achieve the state vector \mathbf{x} of unknown microphysical properties, the log-transformed values are taken.

$$\mathbf{x} = \begin{bmatrix} \log(\lambda)_0 \\ \vdots \\ \log(\lambda)_{\text{nlayer}} \\ \log(N_0)_0 \\ \vdots \\ \log(N_0)_{\text{nlayer}} \end{bmatrix} \quad \text{nlayer} = 14 \quad (3.2.15)$$

The log-transformed equation is useful, since the results from C3VP were similar to other observations. The study showed, that N_0 ranges over several order of magnitude as well as λ was non-Gaussian for the snow events Wood [2011].

3.2.5 SNOWFALL RATE AT THE SURFACE

To achieve snowfall rates at the surface, the snow water content (Equation (3.2.1)) has to be transformed. The use of an assumed particle fall speed of $V = 0.85 \text{ ms}^{-1}$ and the

retrieved SWC (Equation (3.2.1)) gives the snow mass flux $J_{snow} = \text{SWC} \cdot V$ in $[\text{kg m}^{-2} \text{s}^{-1}]$. Why did we use this fall speed? Where does this assumption come from? Similar as Cooper et al. [2017] Eq. 4? To compare retrieved snow fall rates to double fence measurements and the forecast model output, the precipitation amount at the surface is calculated.

$$P = J_{snow} \times 10^{-3} \cdot (3600 \text{s} \cdot 24) \quad [\text{mm d}^{-1}] \quad (3.2.16)$$

The precipitation amount at the surface, presented in Chapter 4, are taken to be equal to the values at the snow layer in 800 m. The use of the values at 800 m is due to the small increase of reflectivity (ground clutter) in the bottom layers and would follow more observed snow.

3.3 NUMERICAL FORECAST MODEL

MEPS (MetCoOp Ensemble Prediction System) was newly operational at Met-Norway when the extreme weather occurred in Norway. Comparing model data with actual observations helps to verify the agreement between model prediction and ground based measurements.

AROME-MetCoOp was operational from March 2014 until November 2016, when it was replaced with an ensemble prediction system (EPS) based on AROME-MetCoOp. MEPS is used as weather forecast at the Norwegian Meteorological Institute, the Swedish Meteorological and Hydrological Institute (SMHI) and the Finnish Meteorological Institute (FMI), [Køltzow, 2017, Müller et al., 2017].

3.3.1 AROME - METCOOP

In principle, MEPS is a short-term weather forecast of 66 h with 10 ensemble member and a horizontal resolution of 2.5 km and 65 vertical levels. One of the members is the deterministic forecast where the other nine present the perturbed state of the deterministic forecast. The initialisation of each member is performed at 0 UTC, 6 UTC, 12 UTC and 18 UTC [MetCoOp Wiki, 2017].

The orange frame in Figure 1.1.1 shows the MEPS model domain as it was operational for December 2016. It covers the Nordic Countries including open water such as the Atlantic Ocean, the North and the Baltic Sea.

The centre of the model is approximately at 63.5° N, 15° E. The horizontal grid points are projected on a Lambert projection to receive the same area size of each grid cell. The outer, parent grid is the ECMWF-IFS model (European Centre for Medium-Range Weather Forecasts Integrated Forecasting System) with a horizontal resolution of 9 km [Homleid and Tveter, 2016]. The ECMWF-IFS forecasts are used 6 h prior to the actual cycle in MEPS. Vertical hybrid coordinates are terrain-following and are mass-based, [Müller et al., 2017]. How the vertical hybrid coordinates are transformed into layer thickness or height is described in Section 3.4.1. Furthermore, MEPS underlies non-hydrostatic dynamics, Met-CoOp Wiki [2017].

The representation of snow is covered by a modification of the three-class ice parametrization (ICE3) scheme. Where liquid-phase processes are separated from slow ice-phase processes and described in Section 3.3.2. To model the snow cover an one-layer atmosphere model scheme is implemented. This includes three variables such as: snow water equivalent (SWE), snow density, and snow albedo [Müller et al., 2017].

As synoptic observations are included in the model the snow-depth predictions underlay a special performance. Observations of snow-depth are only available at 6 UTC and 18 UTC, therefore is the snow analysis only performed twice daily [Homleid and Tveter, 2016, Müller et al., 2017].

3.3.2 MESO-NH AND THE ICE3 SCHEME

The physical parametrization within AROME is based on the French research communities' mesoscale non-hydrostatic atmosphere model (Meso-NH). The microphysical scheme in the Meso-NH atmospheric simulation system is based on the ICE3 scheme. The purpose of the scheme is to model as correctly as possible the ice phase in the atmosphere [Pinty and Jabouille, 1998]. McCumber et al. [1991] concluded from their case study, that at least three different ice categories are necessary to cover most precipitation but that applications might be case specific. According to the Meteo France [2009] documentation, the ice phase microphysical scheme must include:

\mathbf{r}_i : pristine ice phase

\mathbf{r}_s : snowflake type from lightly rimed large ice crystals or dry clusters, and

\mathbf{r}_g : heavily rimed crystals, such as graupel, frozen drops or hail

Within the ICE3 scheme no distinction between hail and graupel exists and therefore is the physical discrimination in the growth mode of graupel and hail is neglected.

To achieve snow water content within MEPS the total number concentration, slope parameter, mass diameter and the particle size distribution have to be determined. According to [Caniaux et al. \[1994\]](#) follows the particle size distribution the Marshall-Palmer distribution similar to Equation (3.2.12). The goal is to use a varying number concentration N_0 dependent on the ice category. The study has shown that N_0 can be assumed with

$$N_0 = C\lambda^x \quad (3.3.1)$$

$$\log_{10} C = -3.55x + 3.89$$

where C and x depend on the ice category and represent the relation between each other in Equation (3.3.1).

The ice water content for primary ice, snowflakes and rimed crystals is then be assumed to be similar to Equation (3.2.1), but the integration limits range from zero to infinity and mass, and particle size distribution are dependent on the diameter of the particle. The mass diameter and particle size distribution (Equations (3.3.2) and (3.3.3)) are represented depending on the ice category shown in Table 3.3.1

$$m(D) = aD^b \quad (3.3.2)$$

$$n(D) = N_0 g(D) \quad (3.3.3)$$

and $g(D)$ to be the generalised Gamma function

$$g(D) = \frac{\alpha}{\Gamma(\nu)} \lambda^{\alpha\nu} D^{\alpha\nu-1} \exp(-(\lambda D)^\alpha) \quad (3.3.4)$$

with α , ν the shape and tail dispersion parameters and $\Gamma(\nu)$ the gamma function.

After following the above equations including Equation (3.2.1) the slope parameter λ can be generated with $G(B)$ the gamma function.

$$\lambda = \left(\frac{\text{SWC}}{aCG(b)} \right)^{\frac{1}{x-b}} \quad (3.3.5)$$

[Meteo France \[2009\]](#) documentation suggests to start the microphysics in the ICE3 scheme with 'slow' processes such as homogeneous and heterogeneous nucleation (HON, HEN),

Table 3.3.1: Characterization parameters from primary ice (r_i), snowflakes (r_s) and rimed crystals (r_g). Values are based on the references in [Meteo France \[2009\]](#) and in [Pinty and Jabouille \[1998\]](#).

	r_i	r_s	r_g
α, ν	3.3	1.1	1.1
a	0.82	0.02	196
b	2.5	1.9	2.8
c	800	5.1	124
d	1.0	0.27	0.66
C		5	5×10^5
x		1	-0.5

vapour deposition of snow and graupel particles (DEP), aggregation (AGG) and autoconversion (AUT), for ice processes right side in Figure 3.3.1. The second step is to initiate the warm processes left side in Figure 3.3.1. Then include the aggregation and conversion-melting (CVM) for snowflakes and contact freezing of raindrops (CFR). Add AGG and melting for graupel (MLT), and then the melting from pristine ice and the Wegener-Bergeron-Findeisen (BER) effect and lastly the sedimentation terms.

Figure 3.3.1 shows the summary of the microphysical processes for mixed phase clouds.

The study focuses mostly on solid precipitation particles and therefore only the initiation and growth of pristine ice crystals r_i , snowflakes r_s , and rimed crystals r_g is presented.

Following [Pinty and Jabouille \[1998\]](#) and Figure 3.3.1 it can be seen how AROME performs the ice production. Orange lines in Figure 3.3.1 show the initiation of pristine ice crystals and snowflakes. In purple the growth mechanisms of r_i (BER,DEP). Green lines demonstrate the expansion of the snowflakes (RIM, AGG, ACC). Graupel (r_g) forms as an effect of heavy riming (RIM), by collision of larger raindrops with snowflakes (ACC), by WET/DRY growth or by contact freezing of raindrops (CFR). All graupel growth processes are indicated by blue lines in Figure 3.3.1, were hail formation is included.

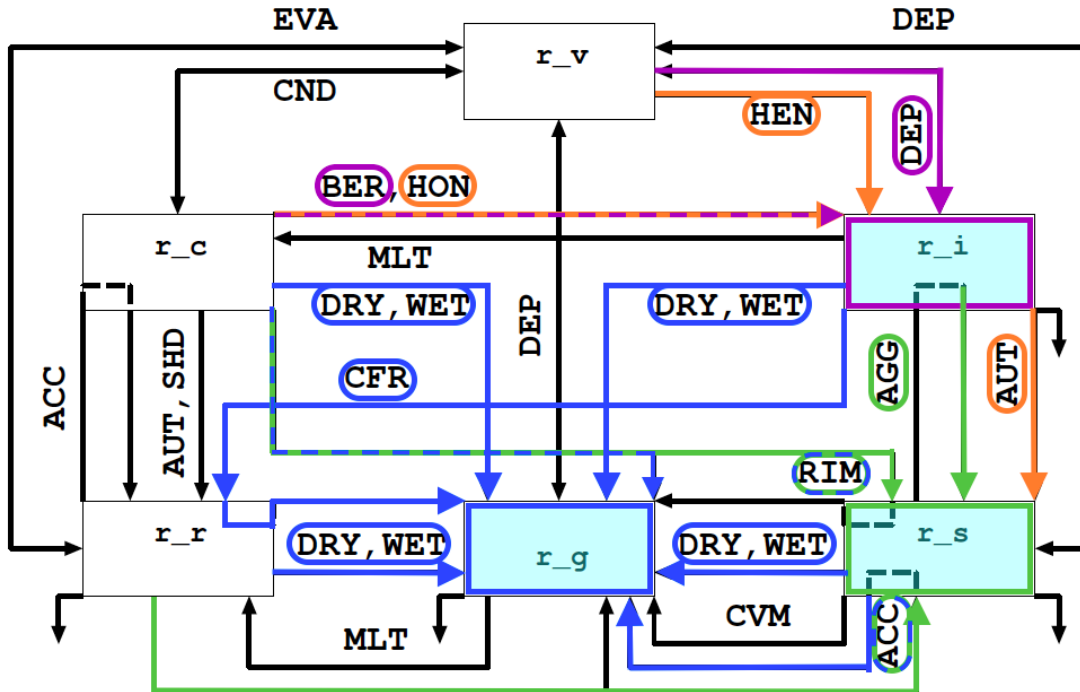


Figure 3.3.1: Microphysical processes for mixed phase clouds in the ICE3 scheme adapted from Meteo France [2009]. In orange the initiation processes for primary ice r_i and snowflakes r_s . The growing processes of r_i is shown in purple and for r_s in green. Graupel particles, r_g , grow from existent particles and the processes are shown in blue.

3.3.3 ADJUSTMENT OF ICE3 INSIDE MEPS

Since the ICE3 scheme showed some weaknesses for the winter month, Müller et al. [2017] introduced some modifications. During cold conditions the ICE3-scheme showed too low temperature at two meter, too much ice fog and all year long was the occurrence of cirrus overestimated. After implementing the modifications described in Müller et al. [2017] the two meter temperature bias was reduced as well as an improvement of low-level clouds was shown. An negative aspect of these adjustments was that the occurrence of fog increased.

3.4 NUMERICAL DATA TRANSFORMATION

The following section will describe how the different variables where processed to achieve a comparison between the retrieved values and the forecast model output.

3.4.1 LAYER THICKNESS IN MEPS

To compare the measurements from the surface with the MEPS data, the closest grid point to Haukeliseter, is used.

MEPS has a vertical resolution in hybrid sigma pressure coordinates, were one is at the surface and decreases with height. To calculate the actual vertical pressure in Pa, a formula is provided in the OPeNDAP Dataset of `meeps_full_2_5km_*.nc` by the [Norwegian Meteorological Institute \[2016\]](#).

$$p(n, k, j, i) = a_p(k) + b(k) \cdot p_s(n, j, i) \quad [\text{Pa}]. \quad (3.4.1)$$

p_s is the surface air pressure in Pa, and information about the variables a_p , b are not given from the access form. [Find reference for sigma-hybrid coordinate transformation equation.](#)

The next step was to convert pressure-levels into actual heights by the use of the hypsometric equation. Here, the air temperature in model levels is used to calculate the mean temperature of each layer.

$$\bar{T} = \frac{\int_{p2}^{p1} T \partial \ln p}{\int_{p2}^{p1} \partial \ln p} \quad [\text{K}] \quad (3.4.2)$$

For the numerical integration, the Simpson rule was used, which is a build-in function in Python.

[Martin \[2006\]](#) presents steps of differentiating the hypsometric equation by using the virtual air temperature. But when the atmospheric mixing ratio is large, will the virtual temperature only be 1 % larger than the actual air temperature. Since the error is little calculations are done with the provided air temperature in model levels.

The thickness, Δz , of each layer is then be found by using the hypsometric equation from

Martin [2006] and the previously calculated mean temperature (Equation (3.4.2)):

$$\Delta z = z_2 - z_1 = \frac{R_d \bar{T}}{g} \ln \left(\frac{p_1}{p_2} \right) \quad [\text{m}] \quad (3.4.3)$$

where R_d is gas constant for dry air with a value of $287 \text{ J kg}^{-1} \text{ K}^{-1}$, standard gravity $g = 9.81 \text{ m s}^{-2}$. p_1 and p_2 are the pressure levels at lower and higher levels, respectively ($p_2 < p_1$). To gain the respective height of each pressure layer, Δz is summed.

3.4.2 SNOW WATER CONTENT

To get a valid comparison between the SWC from the optimal estimation retrieval and the results from MEPS, the SWC is averaged over each hour. Taking the model initialisation of MEPS at 0 UTC the model produces forecast values at 0, 1, 2, ..., 22, 23, ..., 66 UTC. To approach hourly mean values from the retrieval SWC an average over 30 min prior and 29 min after each full hour is performed. This leads to a match of the average value at the same time as from MEPS.

Since MEPS has a higher vertical resolution than the optimal estimation snowfall retrieval each vertical profile of SWC is averaged every 200 m. To accomplish the same vertical resolution only values above 100 m are used to start at the same range height as given from the MRR (Section 3.1.2).

Within the output from MEPS snow water content does not exist for each model layer. Hence the calculation of the SWC is performed by using the three solid precipitation categories given in MEPS. Namely the instantaneous mixing ratio of snowfall (r_s), graupel-fall (r_g) and the atmosphere cloud ice content (r_i). The mixing ratios are represented in kg kg^{-1} and a transformation to gm^{-3} is performed. Densities in each model level (ρ_{ml}) are calculated and then multiplied with the sum of the solid precipitation mixing ratio.

$$\rho_{ml} = \frac{p_{ml}}{R_d T} \quad [\text{kg m}^{-3}] \quad (3.4.4)$$

$$SWC_{ml} = \rho_{ml} \cdot (r_s + r_g + r_i)_{ml} \cdot 10^6 \quad [\text{gm}^{-3}]. \quad (3.4.5)$$

3.4.3 SNOW WATER PATH

The snow water path (SWP) is the vertically integrated value of the averaged SWC (Equations (3.2.1) and (3.4.5)), where the numerical Simpson's integration is applied.

$$\int_{h_0}^{h_1=3000\text{m}} \text{SWC}(h) dh \approx \frac{h_1 - h_0}{6} \left[\text{SWC}(h_0) + \text{SWC}(h_1) + 4\text{SWC}\left(\frac{h_0 + h_1}{2}\right) \right] \quad [g\text{m}^{-2}] \quad (3.4.6)$$

The snow water path is a measure of the weight of ice particles per unit area. It indicates the total amount of ice in the atmosphere.

3.4.4 ENSEMBLE MEAN AND ENSEMBLE SPREAD

Check literature of meaning

The ensemble mean is the average of all ten ensemble members of MEPS.

$$\bar{x} = \frac{\sum_{i=1}^n x_i}{N} \quad (3.4.7)$$

The ensemble spread is known as the standard deviation with respect to their mean of the model output. That means it shows the variation around the center or control run.

$$\sigma = \sqrt{\frac{\sum_{i=1}^n (x_i - \bar{x})^2}{N-1}} \quad (3.4.8)$$

for either variable is the dimension of the standard deviation the same.

To verify how well MEPS performed during the Christmas storm a variation of the SWC is calculated. For this, the standard deviation (Equation (3.4.8)) is divided by the ensemble mean (Equation (3.4.7)).

3.4.5 DEW POINT TEMPERATURE FOR SKEW-T LOG-P DIAGRAM

The Python module pyMeteo is used to calculate the dew point temperature of each ensemble member to study the stability of the atmosphere (<https://pythonhosted.org/pymeteo/>, last visited: 25.01.2018). The additional package thermo.py is able to

calculate the dew point temperature if the pressure and the specific humidity in each level are known.

$$e_l = \ln \left(\frac{\frac{q_v}{\epsilon} \cdot \frac{p}{100}}{1 + \frac{q_v}{\epsilon}} \right) \quad (3.4.9)$$

$$T_d = 273.15 + \frac{243.5 \cdot e_l - 440.8}{19.48 - e_l} \quad [\text{K}] \quad (3.4.10)$$

where, q_v is the specific humidity, p pressure in [Pa], $\epsilon = R_d/R_v = 0.622$ with R_v gas constant for water vapour.

CHAPTER 4: RESULTS AND DISCUSSION

In this chapter the results of the optimal estimation retrieval and the regional mesoscale forecast model are presented. On the basis of the methodology described in Chapter 3 it should be evaluated if a regional mesoscale forecast model prognoses the same snowfall amount as observed with the ground based remote sensing at Haukeliseter. All days of the seven day event showed their own significances. Since some patterns repeated during these days the most interesting days, 21 December 2016, 24 December 2016 and 25 December 2016, are picked and studied in more detail.

4.1 SURFACE SNOWFALL ACCUMULATION

The surface accumulation is a good point to start to see, if the retrieved snowfall amounts at the surface catch the boundary condition as of the double fence. Precipitation amount at the surface are shown in Figure 4.1.1. The figures are representing the observed surface precipitation accumulation in mm over 48 h. Accumulation, measured by the double fence are presented as purple hexagons. Minutely retrieved surface snowfall amount in dash-dotted orange. The ten 48 h forecast ensemble members are lines in black and grey, the deterministic and its perturbed ensemble members, respectively. The blue dashed line shows the ensemble mean of all ten members. Since the deterministic and the first ensemble member are having values every hour and the other perturbed members only every three hours, shows the ensemble mean the precipitation amount at 00 h, 3 h, ..., 21 h, 24 h, ..., 48 h forecast time. Underneath is the associated 10 min average wind of the last hour from the 10 m weather mast at Haukeliseter, to see if surface accumulation observations are influenced by wind.

In general show the 48 h surface accumulation in Figures 4.1.1a to 4.1.1c a good agreement

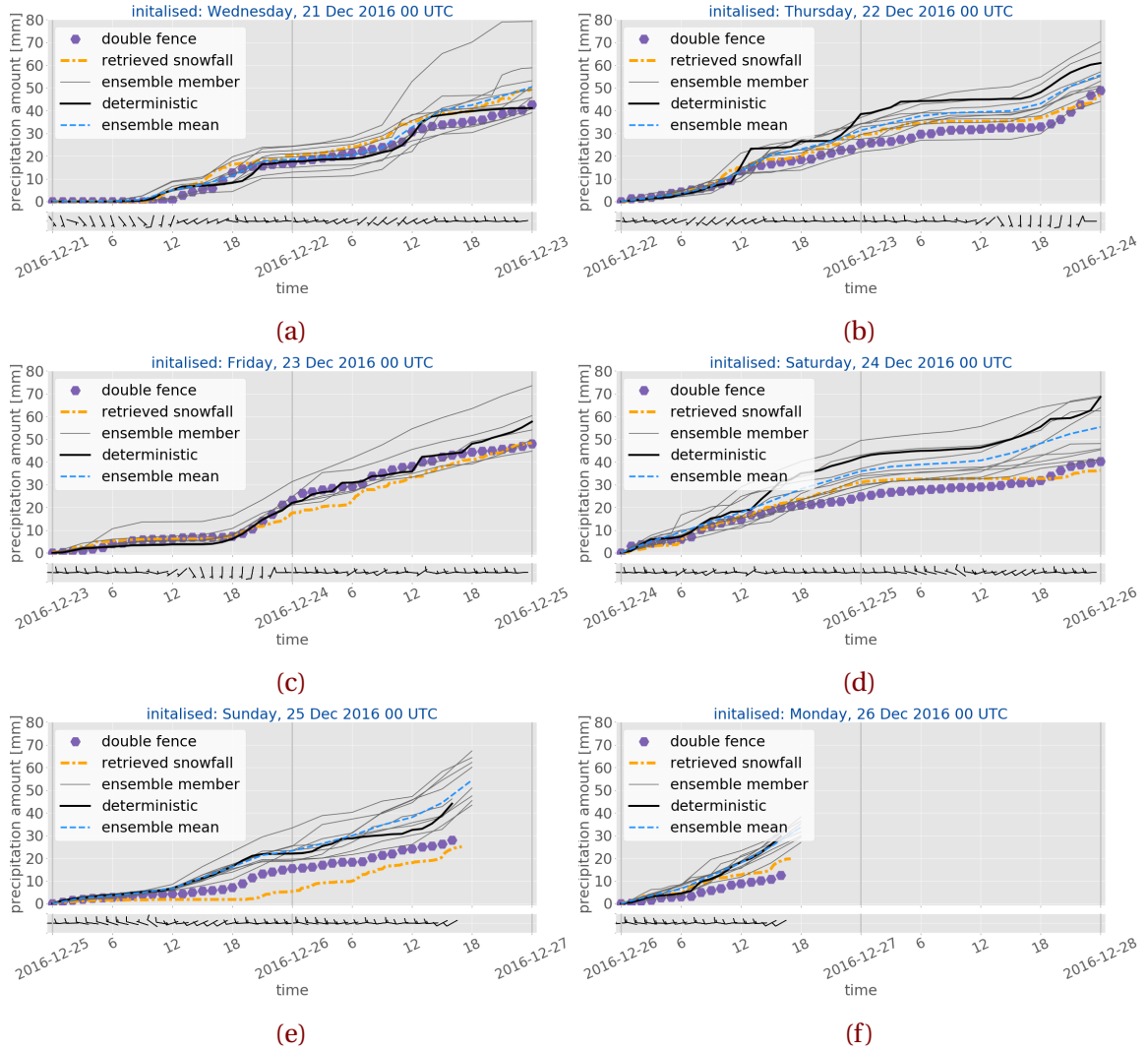


Figure 4.1.1: Surface snowfall accumulation. Representing the values from the double fence in purple, hexagons; optimal estimation retrieval output at snow layer height 800 m in dash-dotted orange; and ensemble member deterministic forecast, initialised at 00 UTC in black and its nine perturbed ensemble members in grey. The ensemble mean of all ten members is shown in blue dashed. Underneath are the associated last 10 min average wind from the weather mast at 10 m height.

between the foreasted values and the retrieved snowfall amount when comparing to the double fence. 24 December 2016 and 25 December 2016 show a disagreement between the surface observations and the model forecast. During this days is the precipitation

amount predicted by MEPS for all ten ensemble members higher than for the measured accumulation. The possible reason for the overestimation at the ground is later discussed in Section 4.1.2 and 4.1.3.

Retrieved accumulation almost always reached the boundary condition of the double fence observations. The only well pronounced mismatch is seen on 25 December 2016, where it measures much less than the double fence gauge.

The surface accumulation initialised on the 21 December 2016 at 00 UTC has one ensemble member overestimating the precipitation amount after 33 h forecast time. Otherwise, agree all three systems well with each other and the perturbed ensemble members are equally spread around the deterministic forecast.

On 22 December 2016 (Figure 4.1.1b) fit the ensemble mean relatively well to the observed surface accumulation, were the double fence estimates the least amount. Clearly, the ensemble members in grey are not equally distributed around the deterministic forecast. The deterministic is predicting more surface accumulation with a large jump after 11 h, always being higher than most of the ensemble members and observations.

When too few ensemble members were present, like on 23 December 2016, no ensemble mean is calculated. Figure 4.1.1c shows a good agreement between the double fence observations and the deterministic forecast. Here, for the first time measures the retrieved surface snowfall accumulation less than for the double fence, but the difference is almost negligible and starts to be too little after 20 UTC on 23 December 2016. This underestimation might be related to the wind change from weaker south to stronger west wind.

Figure 4.1.1d indicates an overestimation of the deterministic surface snowfall prediction already after 16 h forecast time, when initialised on 24 December 2016. The deterministic forecast in solid black is much higher and increases faster than the observations. A higher value of approximately 15 mm can be seen when compared to the surface measurements at 16 UTC on 24 December 2016. This difference remains almost constantly over the forecast time. Furthermore, all ensemble members seem to overestimate the surface accumulation after 24 h prediction time. Since MEPS performed on the previous days one might assume, that the double fence gauge measurements are influenced by the surface winds. By comparing the 10 min average wind at 13 UTC it shows an increase of wind speed from 5 m s^{-1} to 10 m s^{-1} . In Wolff [2018] it is stated, that the gauge protected by a double fence is influenced by wind but the error is not too big compared to strong wind

higher than 20 m s^{-1} . Therefore, it is assumed that the measurements from the double fence are correct and MEPS had rather a forecast error, since the retrieved surface snow accumulation would assume the same precipitation amount. The total accumulated precipitation amount provided in MEPS includes liquid and solid precipitation. The ensemble mean shows also an inaccuracy of forecasted precipitation at the surface. One reason for the overestimation of the accumulation on the ground could be that MEPS has expected a large amount of liquid precipitation, which actually did not occur. A discussion, including a whisker-box-plot from the ensemble members is provided in Section 4.1.2.

On the 26 December 2016 the MRR did not work after approximately 17 UTC and therefore only values before 17 UTC are compared. The surface precipitation amount on 25 December 2016 shows again a miscalculation from MEPS in Figure 4.1.1e. After 12 h forecast time the ensemble members overestimate the surface accumulation, which gets more pronounced at 18 UTC. But still, the model forecast members seem to follow the same structure as the double fence, just too high. Compared to the 24 December 2016 where the ensemble members were not spread equally around the deterministic forecast, shows the 25 December 2016 a good distribution since the ensemble mean is almost the same as the deterministic forecast. The retrieved snowfall accumulation seems to be too little over the entire period, when it starts to precipitate more around 18 UTC on the 25 December 2016 in Figure 4.1.1e. This might be, because the optimal estimation retrieval does not account for liquid precipitation, which was observed during this time period. While the double fence gauge measures liquid and solid precipitation could the pure neglection of liquid precipitation follow the disagreement between double fence and retrieved surface accumulation, which will be further discussed in Section 4.1.3.

Because of an instrumentation error after 17 UTC on 26 December 2016 is this day not really representable. From the double fence precipitation measurement in Figure 2.5.1g and 2.5.1h it is known that precipitation was continuous present until 27 December 2016 10 UTC. Nevertheless, Figure 4.1.1f shows an overestimation by MEPS after 12 h prediction. The spread around the deterministic forecast is relatively narrow with a good agreement between ensemble mean and deterministic.

According to Müller et al. [2017] are strong precipitation events better predicted with MEPS than ECMWF (European Centre for Medium-Range Weather Forecasts), which are used as boundary conditions to initialise MEPS. In Section 1.2 it was described, that during

Table 4.1.1: Surface snowfall accumulation measured by the double fence gauge. Presenting 12 h accumulation before noon and after noon, as well as the total 24 h surface accretion.

Day	Accumulation		
	[mm]		
	12 h (0 to 12 UTC)	12 h (12 to 23 UTC)	24 h
21 December 2016	0.7	16.4	17.1
22 December 2016	13.6	12.0	25.6
23 December 2016	6.3	17.0	23.3
24 December 2016	14.7	10.1	24.8
25 December 2016	4.3	11.1	15.4
26 December 2016	8.8	16.3	25.1

21 December 2016 to 27 December 2016 56.9 % of the total December 2016 accumulation was observed. Also, the Christmas storm was just above being called an extreme event with strong precipitation over seven days.

During the first few days the ensemble outputs cover the surface snow amount good in comparison to the double fence observations. The spread of the ensemble members around the control run fits as well to the observations for this time period. The 21 December 2016 had the highest snow accumulation within 24 h at the surface (compare Table 4.1.1).

For an initialisation on the 24 December 2016, 0 UTC one can see that MEPS over estimates the amount of snow accumulation. It is even more pronounced with the initialisation on the 25 December 2016, 0 UTC (compare Figure 4.1.1e). Even though Müller et al. [2017] states, that an overestimation appears, where the precipitation event (12 h accumulation) is less than 10 mm this seems not to be true for all days. On the 24 December 2016 the miscalculation appears to happen after 13 h. The accumulation before 12 h was 14.7 mm and after that it was around 10 mm. Also on the 25 December 2016 this seems not to be the case even though after noon 12 h accumulation is less than 10 mm. While this was also the case on 21 December 2016 and 23 December 2016 before noon one can not see an inaccuracy between the observations and the forecast. Whereas on 26 December 2016

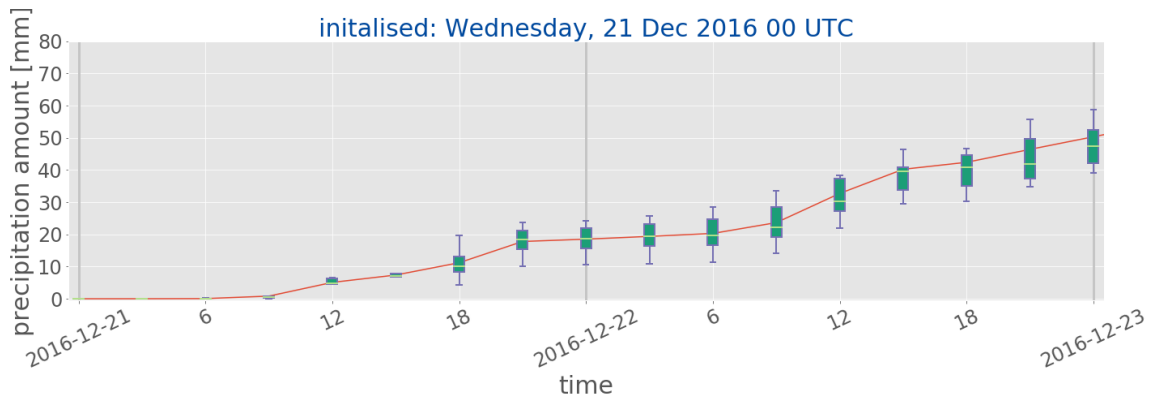


Figure 4.1.2: Box-whisker-plot of the ten ensemble members of MEPS. Red line indicating the ensemble mean, lower and upper whisker the 25th and 75th percentile, respectively. Light green shows the median of all members and the box represents the middle 50 % of scores of the precipitation.

the overestimation might be correlated to the 10 mm problem described by Müller et al. [2017], since until noon a small miscalculation can be seen and the double fence 12 h accumulation measured 8.8 mm.

4.1.1 WEDNESDAY, 21 December 2016

The surface accumulation at the ground in Figure 4.1.1a showed a good agreement between retrieved snowfall amount, MEPS precipitation amount, and the reference frame of the double fence gauge. Since MEPS had an outlier ensemble member a box-whisker-plot is been provided. A box-whisker-plot shows the time evolution of the distribution of the precipitation amount made of ten ensemble members up to 48 h. Since some ensemble member do not have forecast values every hour provides the box-whisker-plot in Figure 4.1.2 information every 3 h. The red line shows the ensemble mean of all ten members. The short light green horizontal line is showing the median, wide vertical box represents the 25th and 75th percentiles, and minimum and maximum values are indicated by the vertical lines.

The box-whisker-plot in Figure 4.1.2 shows the distribution of the ten ensemble members. In the first 15 h of the forecast time agree all members well, since the box and whiskers are narrow. With increasing forecast time, increases the uncertainty. After 33 h is the

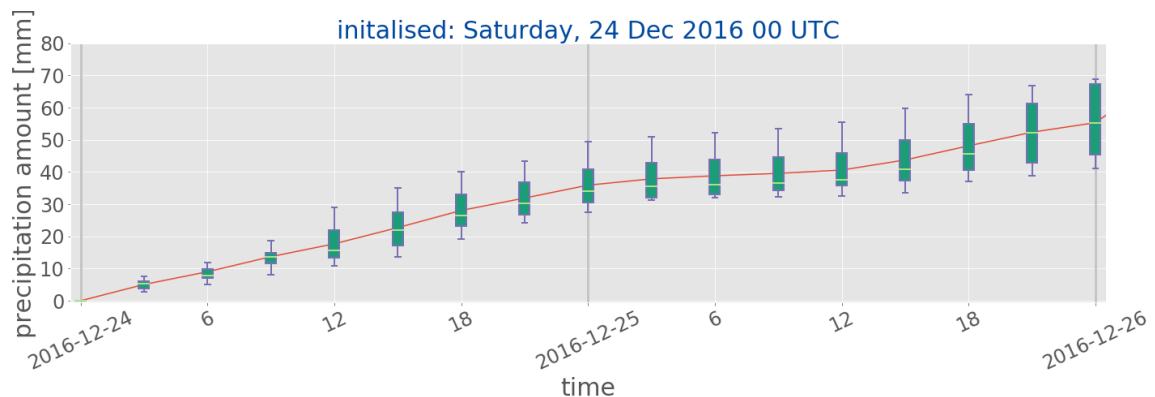


Figure 4.1.3: Box-whisker-plot of the ten ensemble members of MEPS. Red line indicating the ensemble mean, lower and upper whisker the 25th and 75th percentile, respectively. Light green shows the median of all members and the box represents the middle 50 % of scores of the precipitation.

ensemble mean slightly higher than the median of the data. This shift is associated with the one ensemble member being an outlier. In general can the surface forecast be trusted, especially up to 24 h since the values of the ensemble members are well distributed around the mean. Maximum and minimum are not having a too large difference which also shows the small spread between the members.

4.1.2 SATURDAY, 24 December 2016

As discussed early seems the surface precipitation amount on 24 December 2016 not to be influenced by too little precipitation which Müller et al. [2017] showed to be the case for precipitation amount up to 10 mm. To understand what might have led to the overestimation of surface precipitation on the 24 December 2016 in Figure 4.1.1d, a box-whisker-plot is presented. Compared to 21 December 2016 shows the box-whisker-plot in Figure 4.1.3 an uncertainty between the ten ensemble members already after 3 h forecast time. The spread between the ensemble members (shown by the minimum and maximum whiskers) seems to be wide. Not all ten members agree on the same precipitation amount as they did for example on 21 December 2016.

The ensemble mean (red line) is always higher than the median and already after 12 h forecast time is the median closer to the lower 25th percentile. Also, all upper whiskers are

taller than the lower ones, which would follow that the ensemble members vary amongst the most positive quartile and that it is very similar for the least positive quartile group. A comparison with Figure 4.1.1d shows that most of the member lie beneath the ensemble mean (dashed, blue line). On 24 December 2016 the ensemble mean is much lower than the deterministic forecast, which lies closer to the 50th percentile. This is not for all days the case, on most of the days is the ensemble mean either similar or a little less to the deterministic forecast. Since the deterministic forecast, black line in Figure 4.1.1d, is in the upper percentile compared to its perturbed members it follows that for this forecast the deterministic forecast was not the best guess for the surface accumulation and by using the 'wrong' initial state it can have led to larger miscalculations. Therefore, it would be interesting to perform a new deterministic forecast and its associated perturbations to see if a change in choosing another initial state results in a similar measured precipitation amount at the ground.

The uncertainty appearing already after 3 h can be associated with a too long spin-up time of MEPS. MEPS usually has a spin-up time of about three hours on 25 December 2016 this might have been longer and followed by poorer initial conditions. To represent the surface accumulation well, the model systems needs to be spin-up. The regional model MEPS needs initial and boundary conditions from ECMWF before it can produce forecasts. Since initial conditions such as observations have uncertainties as well as the model has mistrust and needs to approach its own climatology, a model has to stabilize before the simulations can be trusted. The spin-up time varies depending on the quality of the initial and boundary conditions. Apparently, it seems, that the initial and boundary conditions for MEPS were not perfect on 24 December 2016 at 0 UTC since the deterministic and perturbed members seem not to have stabilised yet and show uncertainties in Figure 4.1.3 from early on. At this point it might be interesting to re-run the initialisation again with all available observations to see, if that might have an influence on the overestimation observed in Figure 4.1.1d. It might not necessarily be the observations. Since, ECMWF is the boundary condition of MEPS it could also be that the ECMWF forecast did not have reached its stabilised state when MEPS was initiated.

The uncertainty might also have resulted from the fact, that the precipitation around 0 UTC on 24 December 2016 was higher than on the previous days (see, Figure 2.5.1). Where on the previous days the hourly precipitation around 0 UTC was less intense

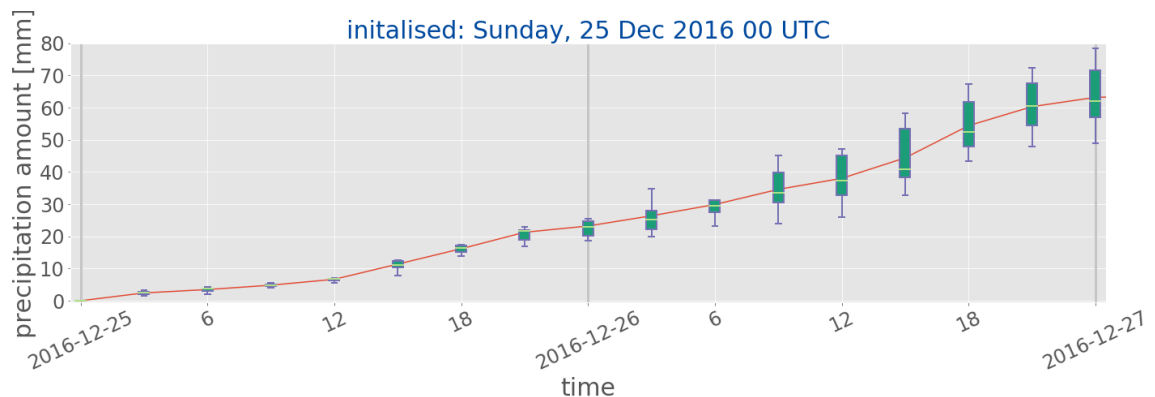


Figure 4.1.4: Box-whisker-plot of the ten ensemble members of MEPS initialised on 25 December 2016 at 0 UTC. Red line indicating the ensemble mean, lower and upper whisker the 25th and 75th percentile, respectively. Light green shows the median of all members and the box represents the middle 50 % of scores of the precipitation.

might a big accretion have followed an uncertainty already after 3 h. MEPS initialised on 24 December 2016 at 0 UTC might have accounted for an additional precipitation at 12 UTC on 24 December 2016 and that led to the strong increase at 13 UTC. This might be a local effect, that a precipitation cell in the model was spatially misplaced or a by a few kilometres or a higher precipitation amount was expected by the model and actually did not occur at Haukeliseter rather at another site close to Haukeliseter, and followed that strong increase after noon.

It is therefore important as the double fence construction or measurements from the MRR to give models a good initial condition from observations, so that spin-up time can be reduced and model initialisation start at a realistic state.

4.1.3 SUNDAY, 25 December 2016

On 25 December 2016 the surface accumulation for the first 12 h is 4.3 mm (see Table 4.1.1). Müller et al. [2017] stated that the deterministic forecast is showing some overestimation if the 12 h accumulation is less than 10 mm. Even though the surface accretion is smaller than 10 mm might that not correlate with miscalculation on 25 December 2016. The overestimation started to be pronounced 13 h after the initialisation in Figure 4.1.1e. Compared to 24 December 2016 are the box-whiskers narrower for the first 30 h on 25 December 2016

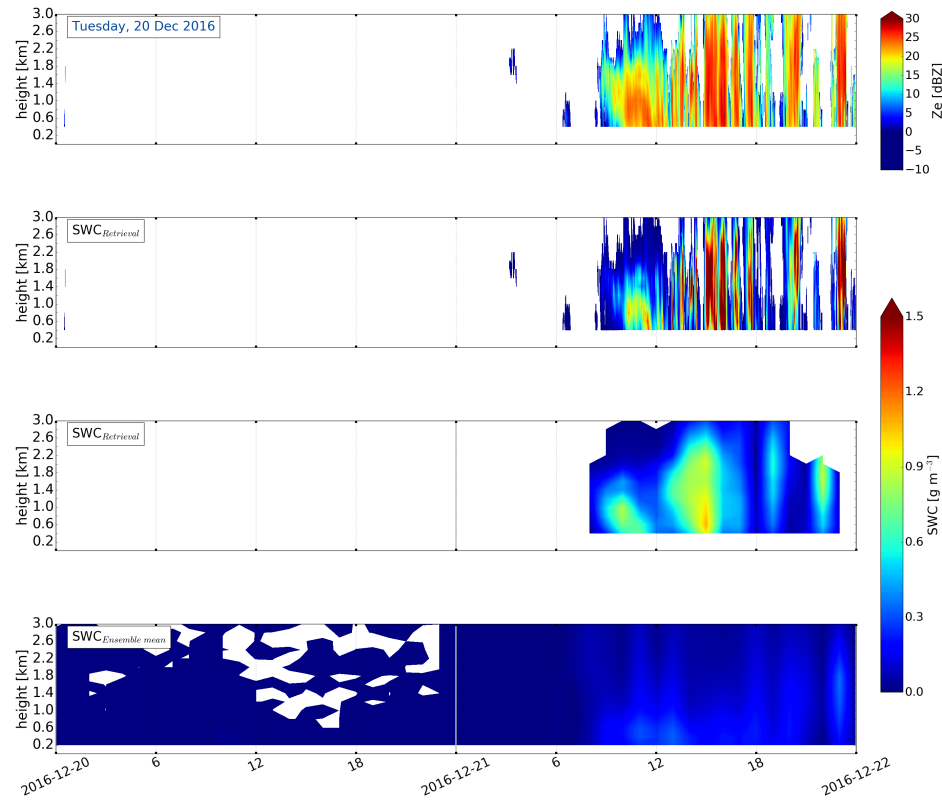
in Figure 4.1.4. The overestimation started to occur around 13 UTC in Figure 4.1.1e. As Figure 4.1.4 shows, increases the uncertainty in the forecast after 15 UTC. In general agree median and mean well for the entire period of a 48 h forecast. After 39 h prediction time is the mean much higher than the median and closer to the lower 25th percentile in Figure 4.1.4. It seems, that all ten ensemble members agree well on the prediction and nevertheless overestimates MEPS the surface accumulation. It shows that the MEPS estimation follows the double fence amount, just not as high.

In this case it might have been a miscalculation of the occurrence and amount of the precipitation. From the box-whisker-plot (Figure 4.1.4) it seems not to be an initialisation problem, since all members agree and the fact that the ensemble mean agrees with the deterministic run. On 25 December 2016 it was expected from the weather maps that a warm front, the warm sector, and a cold front are going to pass. MEPS might have misinterpreted this passages and expected more, probably liquid precipitation associated with the warm front. An error associated with the spin-up time of MEPS is not totally excluded. Since the box-whisker-plot shows a good agreement between all members it is not very likely that this was the problem on 25 December 2016

That the retrieval underestimates the surface precipitation in the afternoon on 25 December 2016 is due to the total negligence of liquid precipitation if the surface temperature exceeds 2 °C. Since the optimal estimation retrieval only uses the moist adiabatic lapse rate of 5 K km^{-1} it might not represent the true state of the atmosphere. Therefore, a use of radiosonde can provide a real structure of the vertical temperature profile which then can help to give real estimations of solid precipitation in the vertical. After the optimal estimation retrieval is fully developed it will be interesting to study the combination of liquid and snowfall precipitation.

4.2 VERTICAL SNOW WATER CONTENT RETRIEVED FROM OPTIMAL ESTIMATION AND MEPS 48 h FORECAST

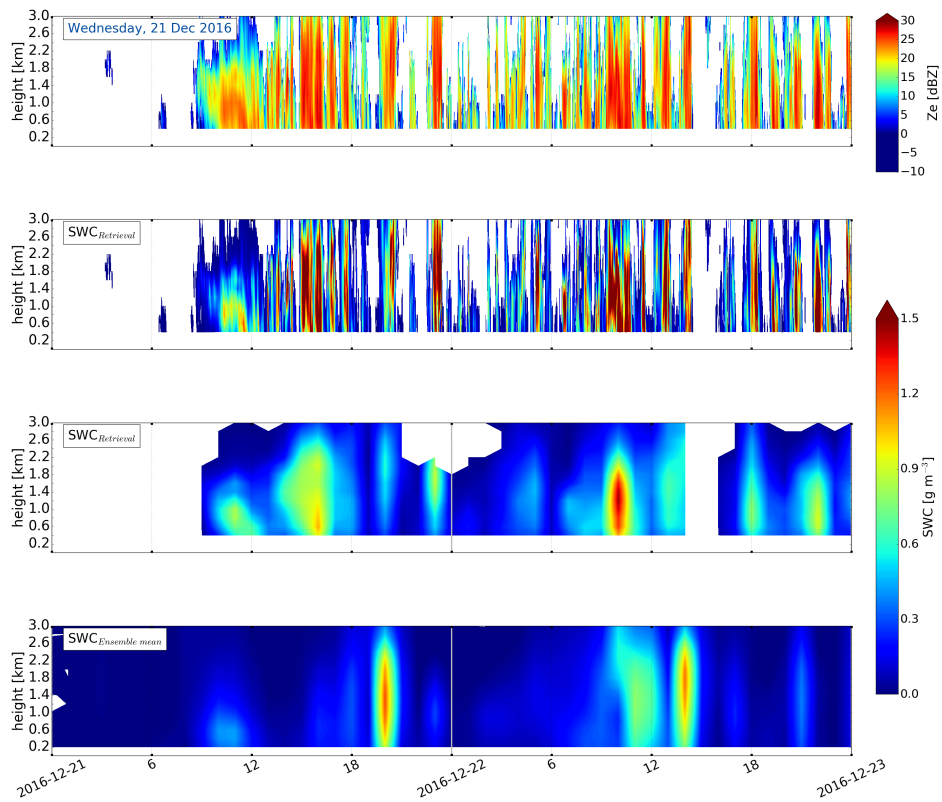
The vertical observations from the MRR and the results of the snowfall retrieval for 20 December 2016 to 27 December 2016 are presented in the three upper panels of Figures 4.1.5a to 4.1.5f. The first panel shows the transformed radar reflectivity in [dBZ], excluding values, were the surface temperature exceeds 2 °C and reflectivities lower than



(a)Initialised: Tuesday, 20 December 2016

-15 dBZ. After the application of the optimal estimation retrieval, the minutely snow water content is shown in the second panel in Figure 4.1.5. The third panel in Figure 4.1.5 shows the hourly averaged SWC from the optimal estimation retrieval. The forecast ensemble mean of all ten ensemble members of MEPS, averaged over 200 m layers is shown in the forth panel. Although ensemble member two to nine have only data every third hour, the ensemble mean was generated every hour. On hours when there was only the deterministic and the first ensemble member, it can cause that the SWC is slightly higher compared to the three hour values when all ten ensemble member existed. A variation of the SWC of all ten ensemble members is described in Section 4.2.1 and the vertical SWC of each ensemble for 21 December 2016, 24 December 2016 and 25 December 2016 are presented in Sections 4.2.2 to 4.2.4

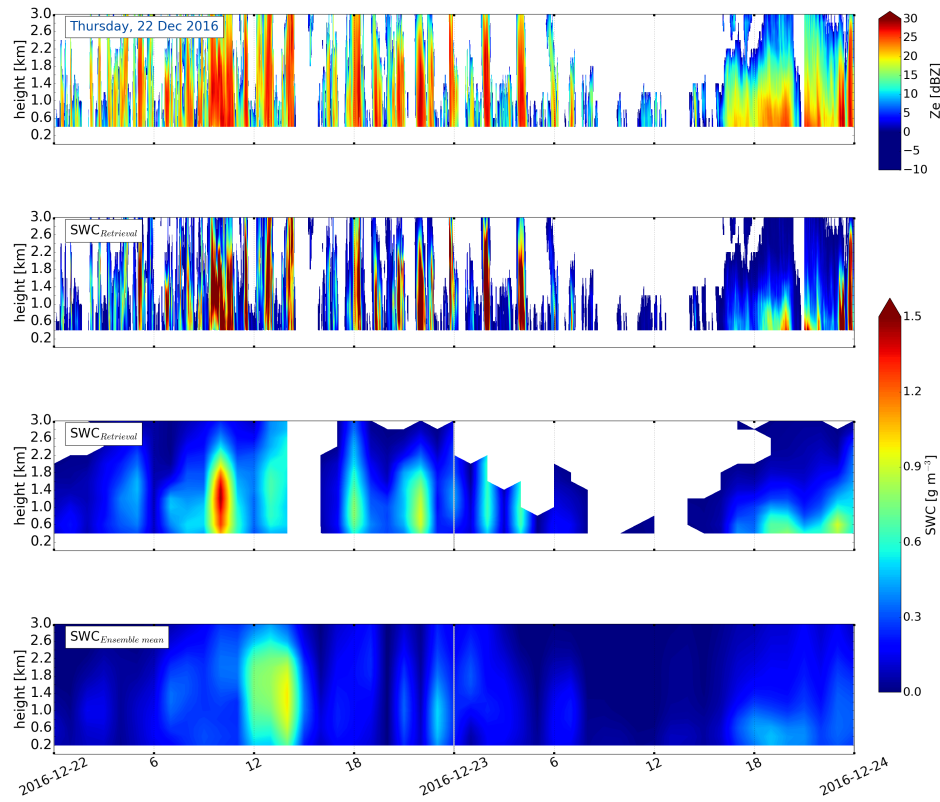
Figure 4.1.5a shows the SWC for an initialisation on 20 December 2016 at 0 UTC. With a forecast time more than 24 h prior to the actual precipitation, MEPS does not catch the



(b) Initialised: Wednesday, 21 December 2016

intensity of the storm. The upper panel in Figure 4.1.5a shows an up-slope event (wind from the east, compare Figure 1.1.1c) between 9 UTC and 13 UTC. This turned afterwards into a pulsing event with intense precipitation, resulting in higher reflectivity and therefore higher SWC of more than 1.5 gm^{-3} , for durations of about half an hour. The association between up-slope winds and therefore more consistent storm structure, can be seen from the wind barbs in Figure 4.1.1a. Up-slope storms are associated with weaker south-east winds and pulsing with stronger wind from the west. When comparing the MEPS forecast initialised on 21 December 2016 at 00 UTC, third and forth panel in Figure 4.1.5b, it shows, that the numerical forecast model captures the up-slope part of the storm, much weaker but around the same time as observed with the MRR. Furthermore captures MEPS some of the pulses occurring after 15 UTC with a peak of 1.24 gm^{-3} at 20 UTC, which is in the observations much weaker at this time. An in-depth analysis of 21 December 2016 is given in ??.

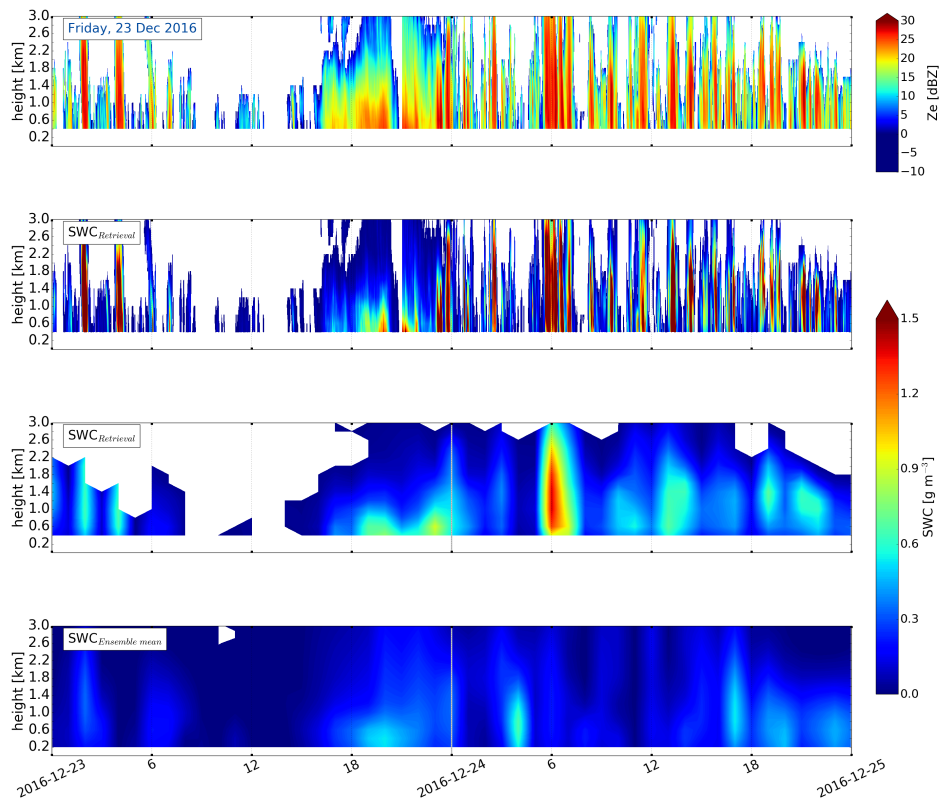
The 22 December 2016 is dominated by south-west to west wind. As Figure 4.1.5b and



(c) Initialised: Thursday, 22 December 2016

4.1.5c show, is this associated with a pulsing of precipitation. High retrieved SWC values are observed by the MRR at 10 UTC. The 24 h prior initialisation of MEPS indicates some of the pulsing during 22 December 2016. A forecast started at 0 UTC on 22 December 2016 smears the pulsing more out and also weakens the averaged SWC of the ensemble mean compared to the initialisation on 21 December 2016, but the pulsing of the event is present in both cases.

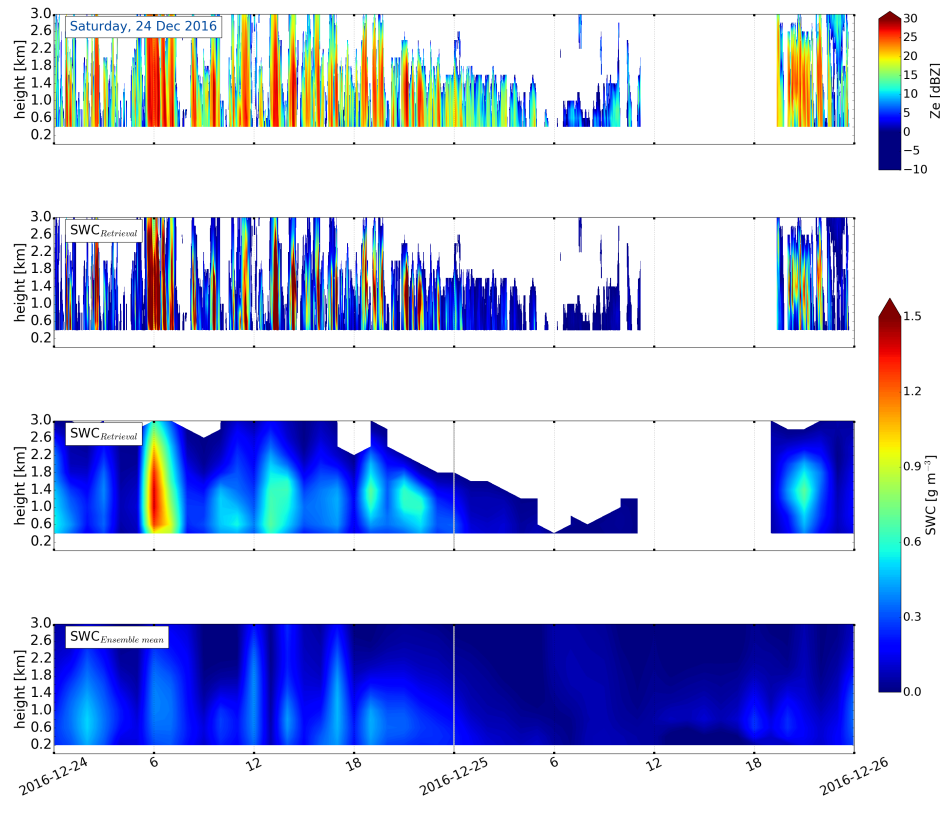
In the evening of 23 December 2016 the wind turns from west to south, again the up-slope wind creates a more consistent storm after around 17 UTC and does not break up the storm structure with a peak of high SWC between 20 UTC to 22 UTC (Figure 4.1.5c and 4.1.5d). Since the wind turns back to west, the maximum value of the hourly averaged SWC is found at 23 UTC. Already on 22 December 2016 one can predict the more consistent up-slope storm in the evening of 23 December 2016, although weak. An initialisation at 0 UTC on 23 December 2016 intensifies the pulses in the morning and reaches slightly higher values when an up-slope storm is observed.



(d) initialised: Friday, 23 December 2016

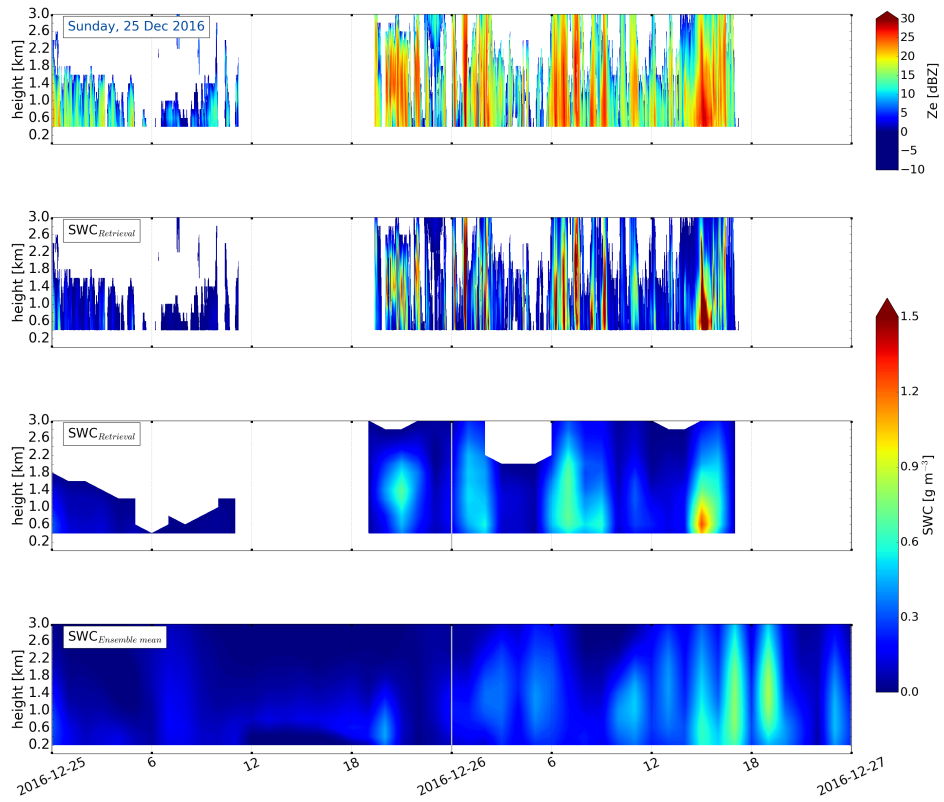
The 24 December 2016 is dominated by strong west winds and therefore associated with a pulsing event. The SWC obtained by the optimal estimation retrieval reaches its peak at 6 UTC. The MEPS forecast, initiated on 23 December 2016, shows already the structure of an pulsing event. Comparing the initialisation at 24 December 2016 (forth panel in Figure 4.1.5e), matches the ensemble mean the structure of the observed pulsing of the storms precipitation. Even though the maximum of 1.39 gm^{-3} was observed around 6 UTC and MEPS had a SWC maximum value of 0.51 gm^{-3} at around 2 UTC is the key, that MEPS already records the structure of the storm more than 24 h before the event. A detailed description and discussion for 24 December 2016 is given in Section 4.2.3.

In the observations on the 25 December 2016 it shows a gap between 11 UTC to 19 UTC in the observations in Figure 4.1.5e and 4.1.5f. This blank is associated with the fact, that the snowfall retrieval assumes to have the presence of rain, if the surface temperature exceeds 2°C and or the reflectivity value is less than -15 dBZ . Until noon show the observations weak snowfall and after the assumed rain a pulsing storm with associated west wind is



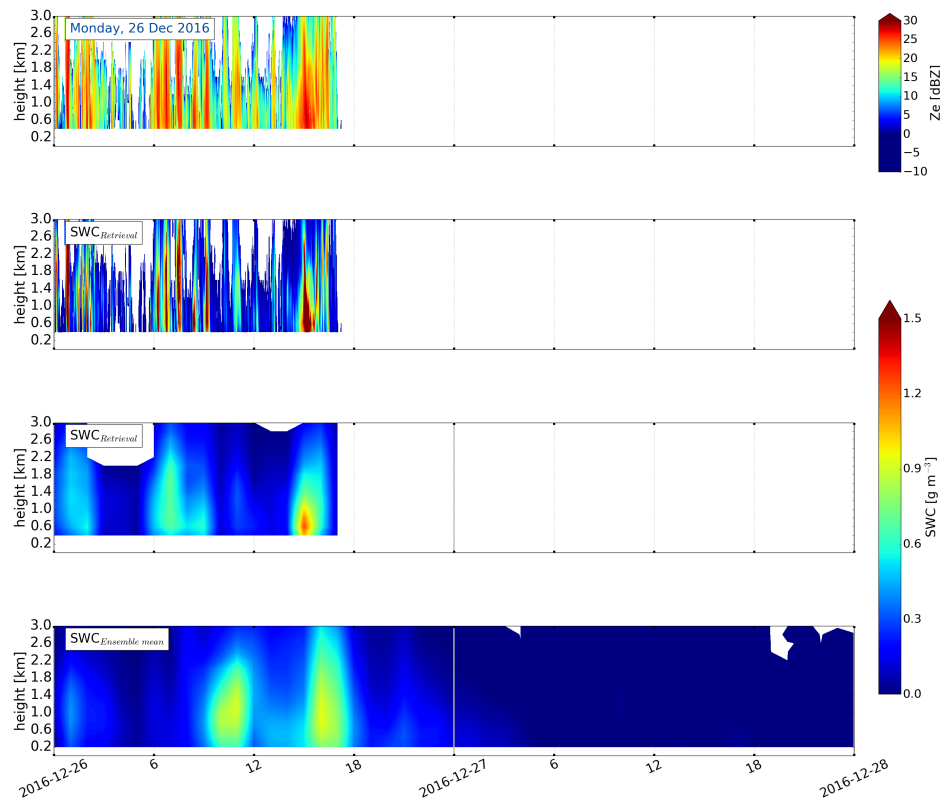
(e) Saturday, 24 December 2016

observed from 19 UTC to 24 UTC. Neither the MEPS initialisation on 24 December 2016 nor on 25 December 2016 estimates the observed pattern on 25 December 2016. MEPS predicts a weak peak just after the rain when initialised less than 24 h in advance. But, it seems that MEPS predicts the liquid water content (LWC) correctly in height and duration between 12 UTC to 18 UTC. The MRR reflectivity shows high values up to 1.2 km during 16 UTC to 20 UTC, shown in Figure 3.2.2. The sum of cloud water content and rainfall amount from MEPS in Figure C.1.1d and C.1.1e show high LWC amount during that specific time with maximum values of 0.32 gm^{-3} at 17 UTC for an initialisation on 25 December 2016 at 0 UTC. Also, in the vertical figures for the SWC (Figure 4.1.5e and 4.1.5f) the liquid layer after noon can be estimated since the values are zero and just above this layer are some lighter blue peaks which indicate a snow water content up to 0.5 gm^{-3} . On 26 December 2016 only retrieved SWC until 17 UTC is valid and comparable, as the reflectivity in the first panel of Figure 4.1.5f and 4.1.5g shows. After approximately 17 UTC did the MRR not respond. The observations show a pulsing, again related to the west



(f) Initialised: Sunday, 25 December 2016

wind over the mountain, close to Haukeliseter. As for 24 December 2016 covers MEPS this pulsing quite well in both, the 24 h and 48 h forecast and even gives an idea how the observations might have been. The maximum SWC value of 1.25 gm^{-3} was observed in the hourly averaged retrieved snow water content (third panel Figure 4.1.5g) at 15 UTC, were the ensemble mean showed a daily maximum value of 0.95 gm^{-3} at 16 UTC. The purpose of this work is to show, that MEPS forecasts cover the observed snow water content. Even though the ensemble mean might not have reached the maximum value or even covered the same time, a delay of 1 h to 2 h is a good performance of the regional ensemble model. Comparing the SWC initialised on 25 December 2016 for the 26 December 2016, it shows more pulsing similar to the observations than an initialisation on 26 December 2016.



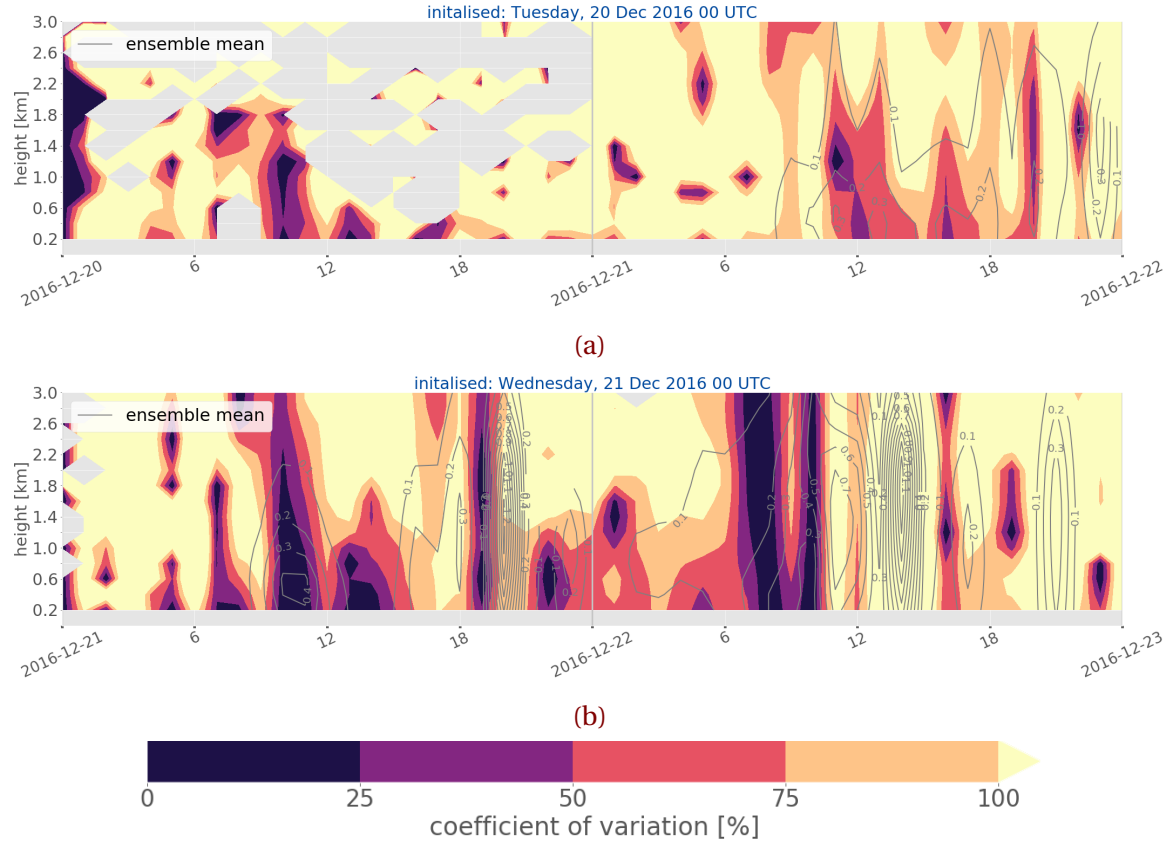
(g)Initialised: Monday, 26 December 2016

Figure 4.1.5: Upper panel: MRR reflectivity in dBZ, excluding the reflectivity for surface temperatures higher than 2 °C . 2nd panel: SWC optimal estimation retrieval output every second in gm^{-3} . 3rd panel: hourly-averaged SWC optimal estimation retrieval output. 4th panel: 200 m-averaged SWC ensemble mean forecast from MEPS.

4.2.1 VERIFICATION OF MEPS ENSEMBLE MEMBERS

To verify how well the ensemble forecast system MEPS has performed, a verification is performed as described in Section 3.4.4. Figures 4.2.1a to 4.2.1f show the coefficient of variation for SWC, which is the standard deviation of the ten ensemble members divided by the mean of all ensemble members. This coefficient gives the possibility to compare the SWC results for different days with different values. It also shows if the ensemble spread (standard deviation of all ensemble members) is low the SWC is does not need to be less variable.

The grey line in Figure 4.2.1 shows the ensemble mean as a contour. The darker the



colour in Figure 4.2.1 the smaller is the variation of SWC relative to the mean. The 23 December 2016 does not exist, because it had too few ensemble members (only six) to create a reasonable verification and therefore is the ensemble mean in Figure 4.1.5d classified as very uncertain. The interpretation of the coefficient of variation for SWC is presented in Table 4.2.1. A small CV indicates a very high forecast accuracy, since the variability is negligible between the ten ensemble members (0 % to <25 %). Similar is a large CV associated with a low forecast accuracy and therefore a very high variability between the members (>100 %). As expected increases the forecast uncertainty with increasing prediction time. It is still possible that in some cases the CV will be larger with a shorter prediction time than with a longer lead time. This could be the case, when strong synoptic systems with complex structure are apparent.

In some cases increases the forecast accuracy with lead time. It also shows, that the CV agrees well with the prediction of the up-slope events and is more often uncertain about the pulsing part, when west wind is observed.

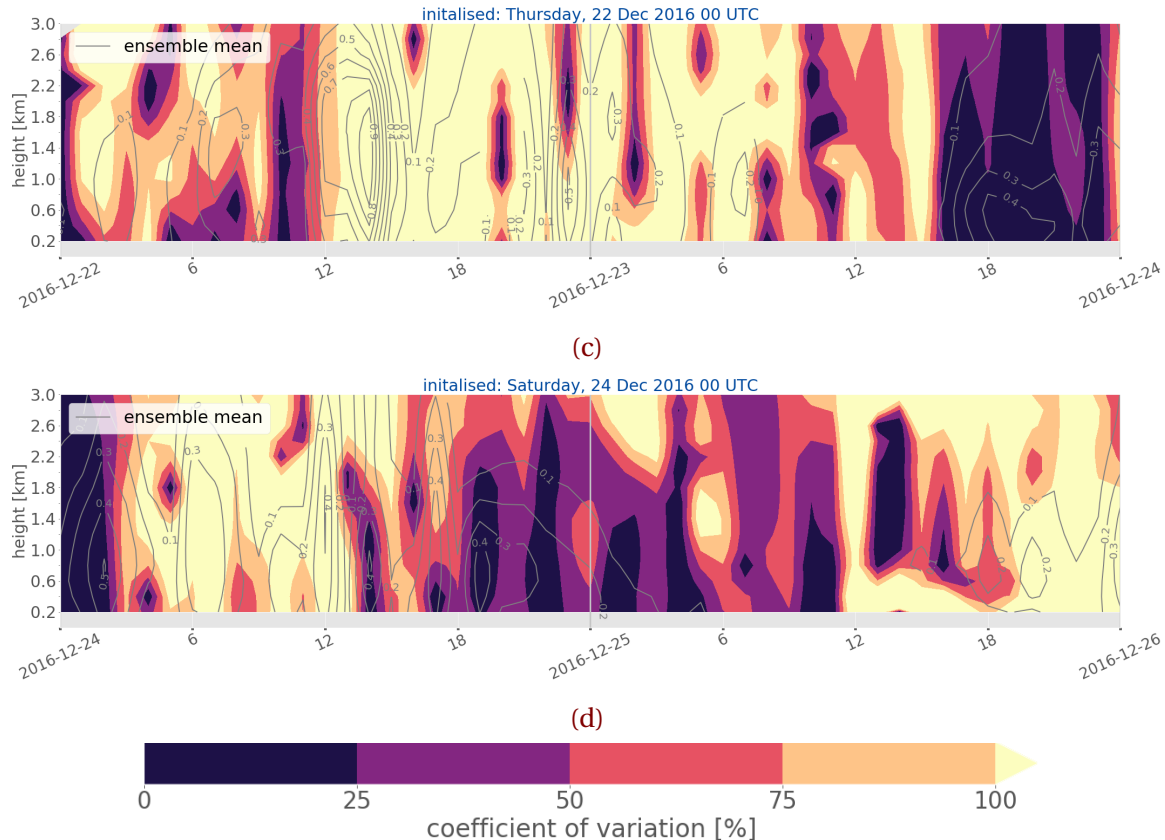


Table 4.2.1: Interpretation of the coefficient of variation for SWC.

Size of CV %	Interpretation	
	variability	forecast accuracy
0 to <25	negligible	very high
25 to <50	low	high
50 to <75	moderate	moderate
75 to <100	high	low
100 to ∞	very high	no

The 21 December 2016 contained an up-slope event between 9 UTC to 13 UTC and a wind change to west followed a pulsed precipitation afterwards. The coefficient of vari-

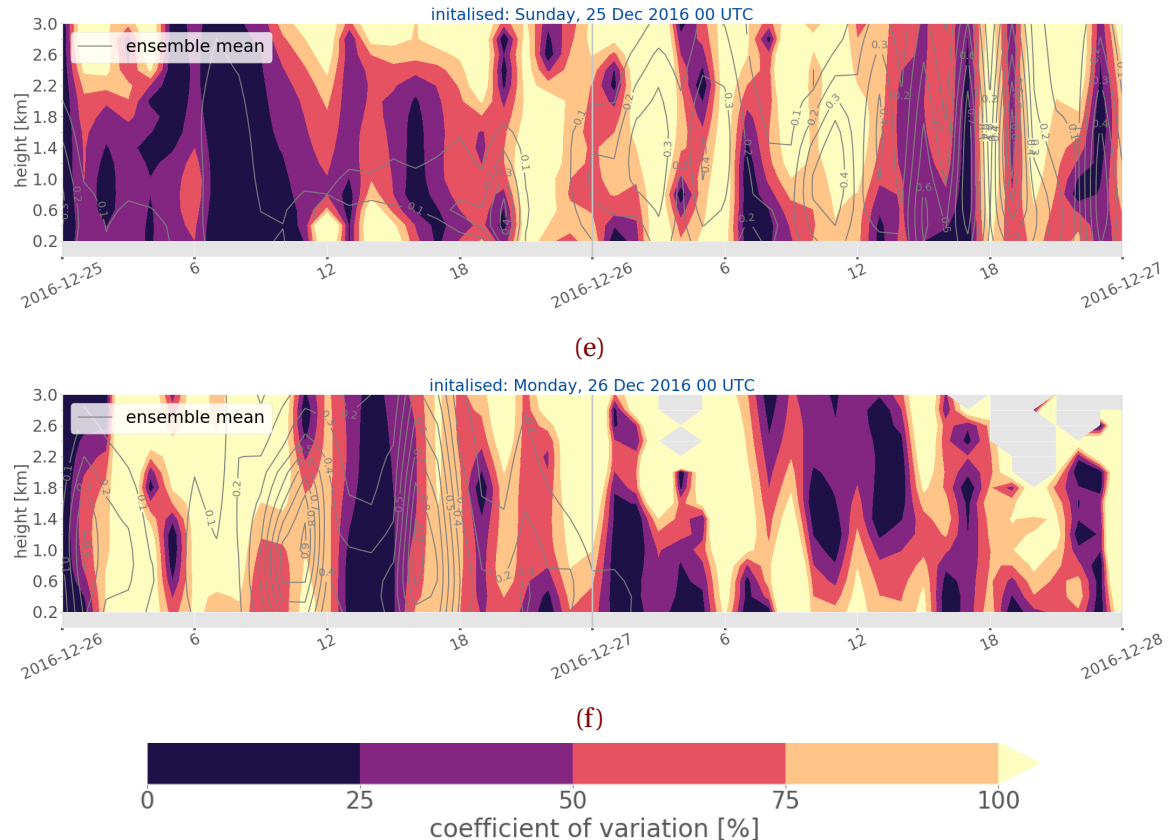


Figure 4.2.1: SWC variation of the ten ensemble members of MEPS. The lighter the colour according to the colourbar the higher the variation between the perturbed ensemble members. In grey the ensemble mean of all ten members.

ation of the SWC in Figure 4.2.1a shows a variation of up to 100 % for the up-slope and more than 100 % for the pulsed part, when initialised on 20 December 2016. An initialisation on 21 December 2016 gives a better result, were the variation is less with a pronounced accuracy of up to 30 % for the up-slope part around noon. The variation shows another good agreement around 19 UTC, one hour prior the maximum predicted mean SWC. For the maximum observed SWC is the CV higher than 90 % and thus no forecast accuracy exists. This maximum followed from the fact, that the deterministic forecast is the strongest at time and all other ensemble members respond with a weaker SWC. The very high variability and the discrepancy between the ensemble members will be discussed further in Section 4.2.2.

While the ensemble mean produced a high SWC at 11 UTC and 14 UTC on the 22 December 2016, shows the variation of SWC a very high variability at this times, when initialised on 21 December 2016 (Figure 4.2.1b). This follows a high uncertainty of the SWC peak values in Figure 4.1.5b, whereas it is very certain some hours before when almost no snow water content was present. For an initialisation on 22 December 2016 is the peak around 11 UTC merged together with the one at 14 UTC. The CV in Figure 4.2.1c displays again a very high forecast accuracy (<25 %) for little SWC and very high variability when the SWC peaks were observed. A moderate to low forecast accuracy can be seen around 3 UTC when the SWC is not higher than 0.3 gm^{-3} . A reason for this discrepancy is again due to the very high predicted SWC performed by the first ensemble member (Figure C.3.1b). Here it shows, that six ensemble members would predict a high SWC around noon, which almost agrees with the vertical retrieved SWC. The pulsing after 18 UTC is forecasted by the first ensemble member and the forth, fifth, and seventh show a possibility of precipitation as well. According to the CV in Figure 4.2.1b and 4.2.1c exists there no forecast accuracy for the predicted peaks and the forecasts are only reliable when there is almost no SWC predicted. On 22 December 2016 shows the forecast for initialisations more than 24 h and less than 24 h prior a pattern as for few precipitation is the forecast accuracy high to very high and for higher SWC is the forecast accuracy not existing.

All ensemble members agree well with the occurrence of the up-slope storm on 23 December 2016 (Figure C.3.1b). The verification in Figure 4.2.1c shows little discrepancy below 50 % with most having a high forecast accuracy. All ten ensemble members forecast the up-slope to occur after 17 UTC, compare Figure C.3.1b. While comparing only six ensemble members in Figure C.3.1c, one could assume that the uncertainty of all ensemble members during the up-slope storm is low, but not as certain as for an initialisation on 22 December 2016 at 0 UTC. The deterministic forecast (EM0) and ensemble member one in Figure C.3.1b indicate peaks of high SWC before 7 UTC. The retrieved SWC on 23 December 2016 had two peaks, one at around 2 UTC and another at 5 UTC. The first ensemble member predicted the peak just to occur in between and a second at 7 UTC. Overall seems the first ensemble member of the 22 December 2016 initialisation to be a good forecast when comparing to the retrieved SWC in Figure 4.1.5c.

The 24 December 2016 was one of the days, where pulsing of the storm was observed and predicted throughout the day. Figure C.3.1c can give an idea about the variation between the six existing forecasts. Three ensemble members (EM0, EM7, EM8) seem to

agree on the occurrence of a SWC peak around 18 UTC, which would be in the range of a moderate forecast accuracy. For an initialisation on 24 December 2016 indicates the variation coefficient of all ten ensemble members in Figure 4.2.1d different accuracies. The ensemble mean is presented in grey and shows the pulses forecasted. Until noon on 24 December 2016 is no forecast accuracy for the peaks. The peak observed at 14 UTC indicates a low variability between the ensemble members. The peak at 17 UTC has a high accuracy up to 0.8 km and moderate up to 1.2 km. After 19 h forecast time is the variability between the ensemble members negligible and all agree on the existence of precipitation. A detail inter-comparison between the surface accumulation and the vertical snow water content is presented in Section 4.2.3.

In general was the 25 December 2016 a very weak snow storm with strong liquid precipitation observed between 12 UTC and 18 UTC. Figure 4.1.5e and Figure 4.1.5f gave a low value of predicted SWC in the course of a day. As Figure 4.2.1d indicates is the forecast accuracy very high up to 1.8 km until noon, this is when liquid precipitation was measured. According to Figure C.1.1d and C.1.1e was the depth of the liquid layer up to 0.8 km. The variation coefficient has a large disagreement below 0.8 km, but above is the variability between the members not existing or low. The weak peak in Figure 4.1.5f at 18 UTC had a moderate forecast accuracy, were it is afterwards very high. For an initialisation on 25 December 2016 is the forecast accuracy high until noon (Figure 4.2.1e). While liquid precipitation was monitored is the accuracy in the lower layer first not existing and shortly before 18 UTC very high. A high agreement exists for the SWC peak up to 0.8 km and decreases to be moderate above. A discussion about the precipitation change and its related forecast is given in Section 4.2.4.

Again, the 26 December 2016 is only comparable until 17 UTC even though Figure 4.1.5f would suggest a continues pulsing of the storm. The two peaks around 18 UTC (Figure 4.1.5f) are forecasted with a very high and moderate accuracy in Figure 4.2.1e. The SWC peaks at around 2 UTC and 5 UTC show a very high variability. Figure 4.2.8 shows that four out of ten ensemble members would agree with the peaked event around 5 UTC. Whereas the peak at 2 UTC is dominated by the strong predicted SWC of the deterministic forecast, which follows the high variation in Figure 4.2.1e. Initialised on 26 December 2016 follows that the SWC peak at 2 UTC is related to a moderate forecast accuracy. Low forecast accuracy is shown for the SWC at 11 UTC and the one at 16 UTC has a low to moderate variability between the members. When looking at Figure C.3.1d might this disagreement

be related to the colourful variation of the vertical predicted SWC. There seems no agreement between the different members about the incidence of the SWC peaks. The high conflict for the CV before noon is most likely related to the high SWC of the deterministic SWC.

4.2.2 WEDNESDAY, 21 December 2016

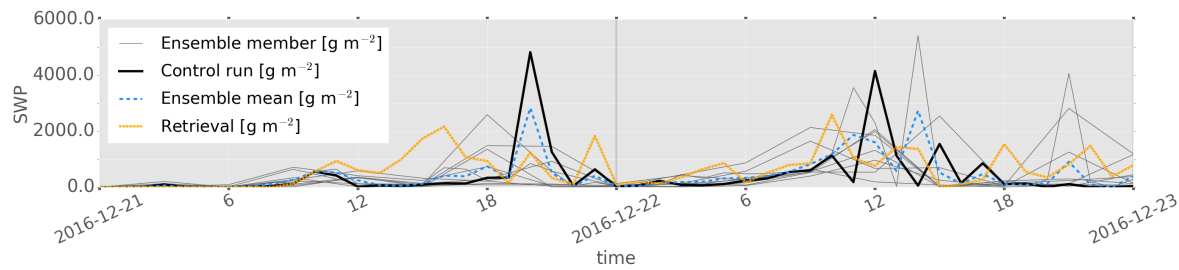


Figure 4.2.2

It shows from the SWP image in Figure 4.2.2, that the deterministic forecast of MEPS (black line) dominates. Most of the other ensemble members (grey line) prognoses the daily maximum snowfall amount two hours earlier than the deterministic forecast. The blue, dashed line, indicating the ensemble mean SWP shows the weakening of the snowfall amount when taking the average of all ten ensemble members with a maximum value at 20 UTC. By comparing the orange line (SWP from the retrieval) and the blue, dashed line it shows, that the ensemble mean value of MEPS gets closer to the observed one, 2833 g m^{-2} and 2162 g m^{-2} respectively. **DISCUSSION!** Why does MEPS not catch that peak at 16 UTC? Maybe because it is too close to the up-slope storm. Also, Why is the control so high compared to the perturbed members? It catches the up-slope part when also a little weak. Most of the ensemble members would have caught it around 9 UTC. One ensemble member has predicted a high value of SWC at 18 UTC, compare to Figure 4.2.3. Why is the up-slope storm more consistent compared to the pulsing? Regional effects? MEPS does well even with catching the pulses and up-slopes, at Haukeliseter is a very difficult orography.

The vertical temperature profile performed with MEPS in Figure 4.2.4a and 4.2.4b, shows that an initialisation 36 h prior to the event would give a cloud with height up to 3 km, as observed in Figure 4.1.5b first panel. An initialisation closer to the occurrence of the storm

shows, that MEPS underestimates the intensity and height of the storm (Figure 4.2.4b).
DISCUSSION! Bring all into relation with the coefficient of variation.

4.2.3 SATURDAY, 24 December 2016

DISCUSSION! Bring all into relation and include the verification plots

- Because EM3, EM4, EM7 to EM9 are only valid every three hours can precipitation peaks not crop up in such a high frequency as for example the deterministic forecast.

4.2.4 SUNDAY, 25 December 2016

DISCUSSION! Bring all into relation and include the verification plots

4.3 WEDNESDAY, 21 December 2016

Get surface accumulation and vertical into relation. Why does the surface overestimate, but the vertical is weaker. Why does the surface overestimate but the vertical seems to catch the observations better?

4.4 SATURDAY, 24 December 2016

4.5 SUNDAY, 25 December 2016

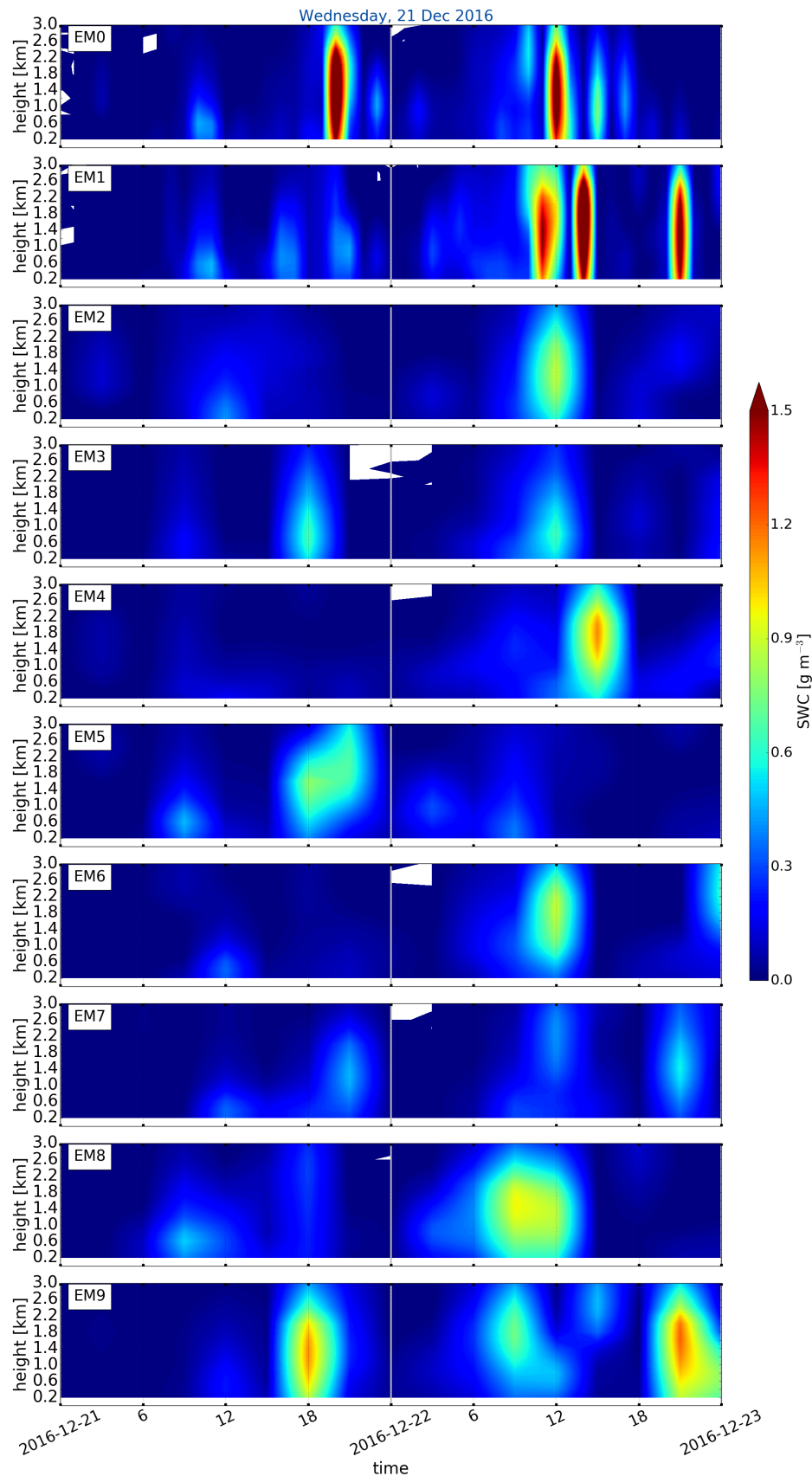


Figure 4.2.3: SWC of all ensemble members initialised Wednesday, 21 December 2016 at 00 UTC forecast for 48 h.

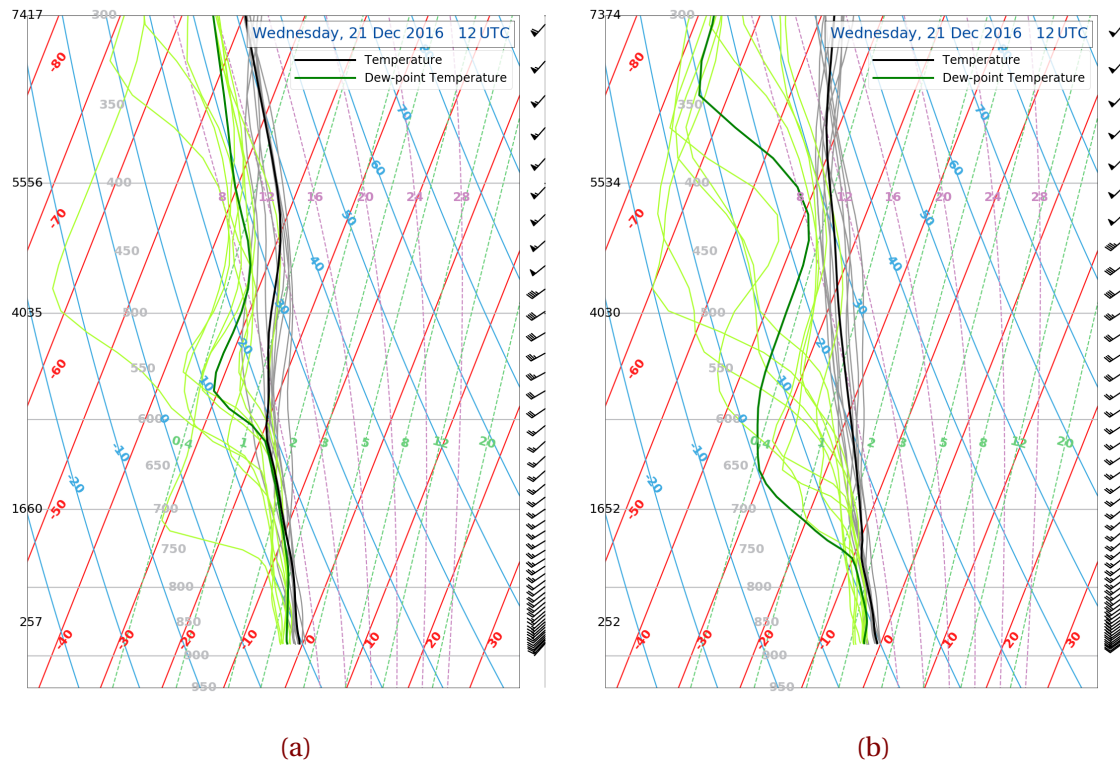


Figure 4.2.4: Vertical temperature profiles produced with MEPS. **a** is initialised: Tuesday, 20 December 2016 0 UTC. **b** is initialised: Wednesday, 21 December 2016 0 UTC.

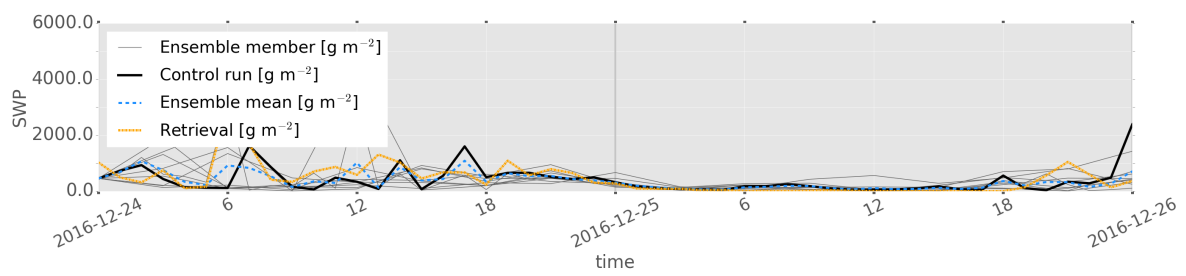


Figure 4.2.5

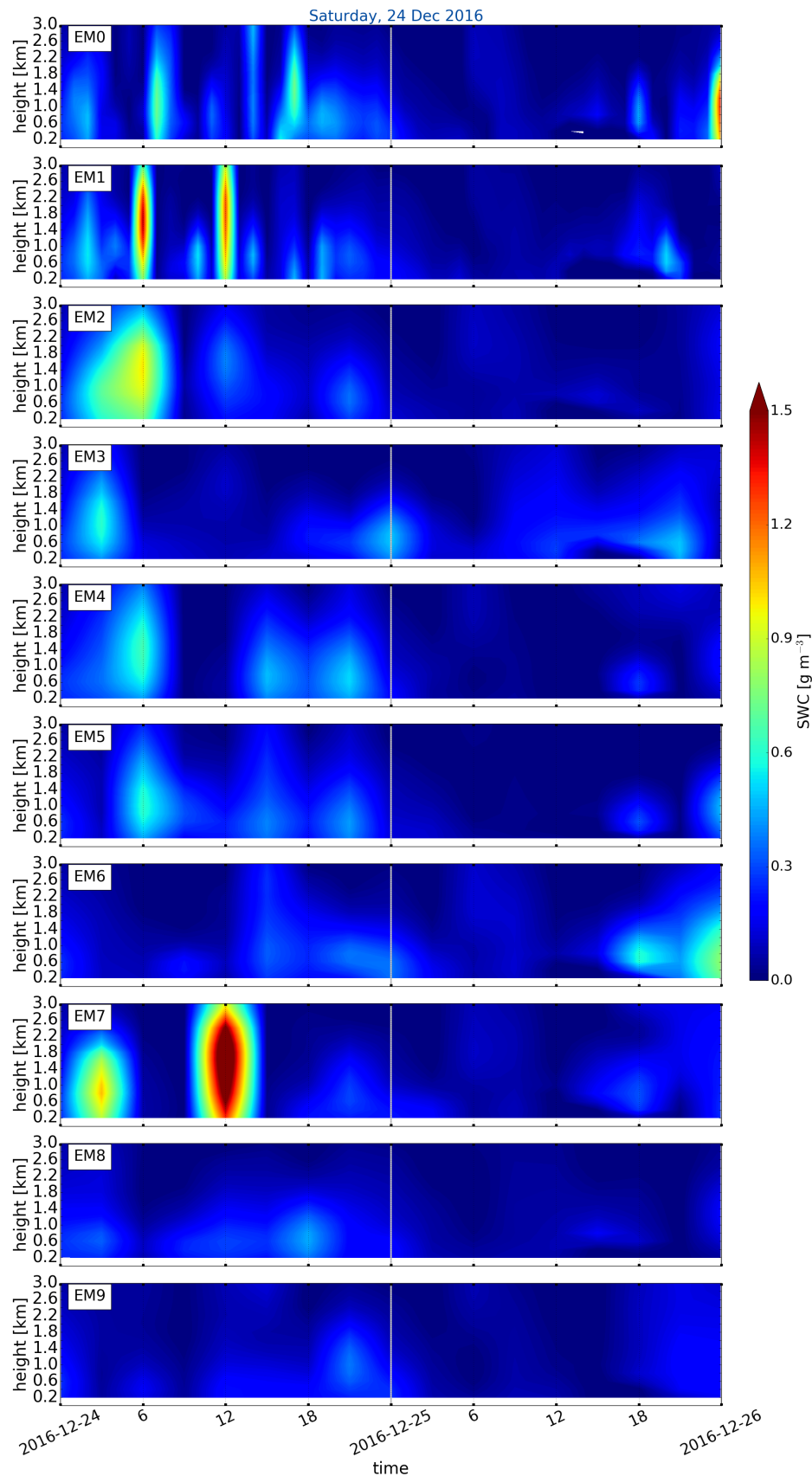


Figure 4.2.6: SWC of all ensemble members initialised Saturday, 24 December 2016 at 00 UTC forecast for 48 h.

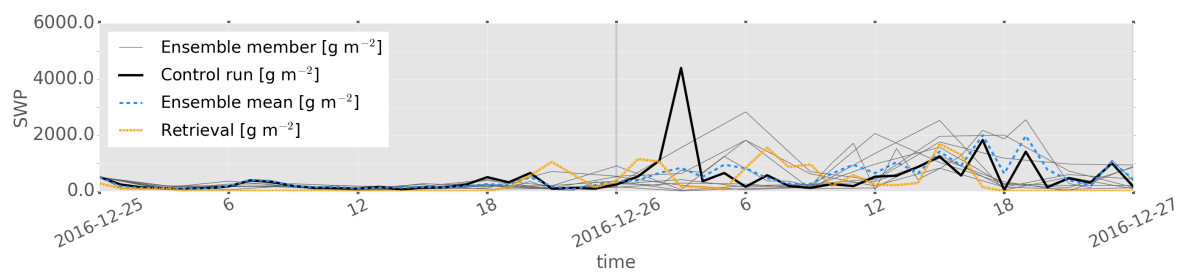


Figure 4.2.7

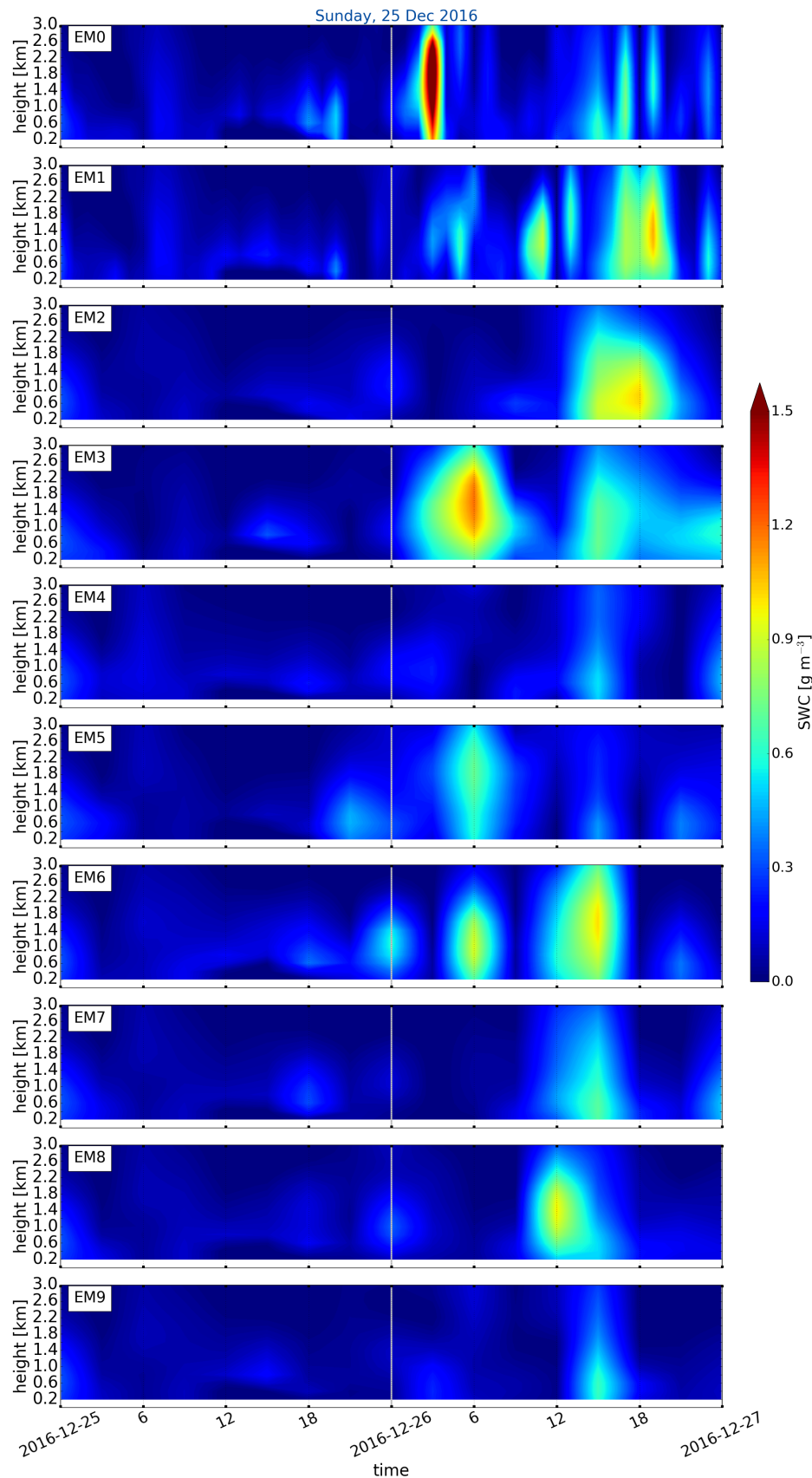


Figure 4.2.8: SWC of all ensemble members initialised Sunday, 25 December 2016 at 00 UTC forecast for 48 h.

CHAPTER 5: SUMMARY AND CONCLUSION

SUMMARIZE! What did you do? Why did you do it? What did you use? What were your findings? What could be done in the future?

REFERENCES

- G. Caniaux, J-L. Redelsperger, and J-P. Lafore. A Numerical Study of the Stratiform Region of a Fast-Moving Squall Line. Part I: General Description and Water and Heat Budgets. *J. Atmos. Sci.*, 51(14):2046–2074, July 1994. ISSN 0022-4928. doi: [10.1175/1520-0469\(1994\)051<2046:ANSOTS>2.0.CO;2](https://doi.org/10.1175/1520-0469(1994)051<2046:ANSOTS>2.0.CO;2). URL [https://journals.ametsoc.org/doi/abs/10.1175/1520-0469\(1994\)051%3C2046:ANSOTS%3E2.0.CO;2](https://journals.ametsoc.org/doi/abs/10.1175/1520-0469(1994)051%3C2046:ANSOTS%3E2.0.CO;2).
- S. J. Cooper, N. B. Wood, and T. S. L'Ecuyer. A variational technique to estimate snowfall rate from coincident radar, snowflake, and fall-speed observations. *Atmos. Meas. Tech.*, 10(7):2557–2571, July 2017. ISSN 1867-8548. doi: [10.5194/amt-10-2557-2017](https://doi.org/10.5194/amt-10-2557-2017). URL <https://www.atmos-meas-tech.net/10/2557/2017/>.
- R. J. Doviak and D. S. Zrnic. *Doppler Radar and Weather Observations*. Courier Corporation, 1993. ISBN 978-0-486-45060-5. Google-Books-ID: [ispLkPX9n2UC](#).
- eklima. Norwegian Meteorological Institute, 2016. URL http://sharki.oslo.dnmi.no/portal/page?_pageid=73,39035,73_39049&_dad=portal&_schema=PORTAL.
- E. Farestveit. 80.000 mista radioen under ekstremvêret, December 2016. URL <https://www.nrk.no/hordaland/80.000-mista-radioen-under-ekstremveret-1.13294980>.
- A. Færaas, A. Rommetveit, J. Duesund, and E. Senel. «Urd» har nådd orkan styrke – flytter seg mot Østlandet, December 2016. URL http://www.yr.no/artikkel/_urd_-har-nadd-orkan-styrke--flytter-seg-mot-ostlandet-1.13292245.
- T. J. Garrett, C. Fallgatter, K. Shkurko, and D. Howlett. Fall speed measurement and high-resolution multi-angle photography of hydrometeors in free fall. *Atmos. Meas. Tech.*, 5

- (11):2625–2633, November 2012. ISSN 1867-8548. doi: [10.5194/amt-5-2625-2012](https://doi.org/10.5194/amt-5-2625-2012). URL <https://www.atmos-meas-tech.net/5/2625/2012/>.
- Geonor Inc. T-200b All Weather Precipitation – Rain Gauge, 2015. URL <http://geonor.com/live/products/weather-instruments/t-200b-weather-precipitation-rain-gauge/>.
- K. L. S. Gunn and T. W. R. East. The microwave properties of precipitation particles. *Q. J. Royal Meteorol. Soc.*, 80(346):522–545, 1954.
- M. Homleid and F. T. Tveter. Verification of operational weather prediction models september to november 2015. *METInfo Rep*, 16:2016, 2016. URL https://www.met.no/publikasjoner/met-info/met-info-2016/_attachment/download/b0463915-cba0-42ac-8539-4233ae2bf01c:3d71565a27f88085373199a33ab8569151c144e9/MET-info-22-2016.pdf.
- B. J. Hoskins, M. E. McIntyre, and A. W. Robertson. On the use and significance of isentropic potential vorticity maps. *Q. J. Royal Meteorol. Soc.*, 111(470):877–946, October 1985. ISSN 1477-870X. doi: [10.1002/qj.49711147002](https://doi.org/10.1002/qj.49711147002). URL <http://onlinelibrary.wiley.com/doi/10.1002/qj.49711147002/abstract>.
- D. Hudak, H. Barker, P. Rodriguez, and D. Donovan. The Canadian CloudSat Validation Project. *4th ERAD*, September 2006. URL <http://www.crahi.upc.edu/ERAD2006/proceedingsMask/00165.pdf>. Barcelona, Spain.
- H. Joos and H. Wernli. Influence of microphysical processes on the potential vorticity development in a warm conveyor belt: a case-study with the limited-area model COSMO. *Q. J. Royal Meteorol. Soc.*, 138(663):407–418, January 2012. ISSN 00359009. doi: [10.1002/qj.934](https://doi.org/10.1002/qj.934). URL <http://doi.wiley.com/10.1002/qj.934>.
- Kartverket. Norgeskart, November 2018. URL http://www.norgeskart.no/?_ga=2.7509489.291164698.1524482471-1352211079.1517515119#!?project=seeiendom&layers=1002,1015&zoom=4&lat=7197864.00&lon=396722.00.
- M. S. Kulie and R. Bennartz. Utilizing Spaceborne Radars to Retrieve Dry Snowfall. *J. Appl. Meteor. Climatol.*, 48(12):2564–2580, January 2009. ISSN 1558-8424. doi:

- 10.1175/2009JAMC2193.1. URL <http://journals.ametsoc.org/doi/abs/10.1175/2009JAMC2193.1>.
- M. A. Ø. Køltzow. MetCoOp EPS - A convection permitting ensemble prediction system, October 2017.
- D. Lamb and J. Verlinde. *Physics and Chemistry of Clouds*. Cambridge University Press, April 2011. ISBN 978-1-139-50094-4. Google-Books-ID: H97QKhe16aUC.
- T. S. L'Ecuyer. AOS 441 - Satellite and Radar Meteorology. January 2017. URL <https://lecuyer.aos.wisc.edu/aos441>.
- T. S. L'Ecuyer and G. L. Stephens. An Estimation-Based Precipitation Retrieval Algorithm for Attenuating Radars. *J. Appl. Meteor.*, 41(3):272–285, January 2002. ISSN 0894-8763. doi: [10.1175/1520-0450\(2002\)041<0272:AEBPRA>2.0.CO;2](https://doi.org/10.1175/1520-0450(2002)041<0272:AEBPRA>2.0.CO;2). URL [http://journals.ametsoc.org/doi/abs/10.1175/1520-0450\(2002\)041%3C0272:AEBPRA%3E2.0.CO%3B2](http://journals.ametsoc.org/doi/abs/10.1175/1520-0450(2002)041%3C0272:AEBPRA%3E2.0.CO%3B2).
- Liu G. Deriving snow cloud characteristics from CloudSat observations. *J. Geophys. Res. Atmos.*, 113(D8), September 2008. ISSN 0148-0227. doi: [10.1029/2007JD009766](https://doi.org/10.1029/2007JD009766). URL <https://agupubs.onlinelibrary.wiley.com/doi/abs/10.1029/2007JD009766>.
- U. Lohmann, F. Lüönd, and F. Mahrt. *An Introduction to Clouds: From the Microscale to Climate*. Cambridge University Press, June 2016. ISBN 978-1-107-01822-8. Google-Books-ID: KR1CDAAAQBAJ.
- P. Markowski and Y. Richardson. *Mesoscale Meteorology in Midlatitudes*. John Wiley & Sons, September 2011. ISBN 978-1-119-96667-8. Google-Books-ID: MDeYosfLLEYC.
- J. E. Martin. *Mid-Latitude Atmospheric Dynamics: A First Course*. Wiley, May 2006. ISBN 978-0-470-86466-1.
- M. McCumber, W.-K. Tao, J. Simpson, R. Penc, and S.-T. Soong. Comparison of Ice-Phase Microphysical Parameterization Schemes Using Numerical Simulations of Tropical Convection. *J. Appl. Meteor.*, 30(7):985–1004, July 1991. ISSN 0894-8763. doi: [10.1175/1520-0450-30.7.985](https://doi.org/10.1175/1520-0450-30.7.985). URL [https://journals.ametsoc.org/doi/abs/10.1175/1520-0450-30.7.985](https://doi.org/10.1175/1520-0450-30.7.985).

- MetCoOp Wiki. Description of MEPS, December 2017. URL <https://metcoop.smhi.se/dokuwiki/nwp/metcoop/>.
- Meteorologische Messtechnik GmbH METEK. Micro Rain Radar MRR-2, October 2010. URL <http://metek.de/wp-content/uploads/2014/05/Metek-Micro-Rain-Radar-MRR-2-Datasheet.pdf>.
- Meteo France. The Meso-NH Atmospheric Simulation System: Scientific Documentation, Part III: Physics, January 2009.
- Meteorologene. "Her kommer #Urd! Selve Lavtrykksenteret treffer Møre og Romsdal, men den sterkeste vinden kommer sør for Stad. #SørNorge" 26 December 2016, 9:34am, 2016. URL <https://twitter.com/Meteorologene>.
- M. Müller, M. Homleid, K.-I. Ivarsson, M. A. Ø. Køltzow, M. Lindskog, K. H. Midtbø, U. Andrae, T. Aspelien, L. Berggren, D. Bjørge, P. Dahlgren, J. Kristiansen, R. Randriamampianina, M. Ridal, and O. Vignes. AROME-MetCoOp: A Nordic Convective-Scale Operational Weather Prediction Model. *Wea. Forecasting*, 32(2):609–627, January 2017. ISSN 0882-8156. doi: [10.1175/WAF-D-16-0099.1](https://doi.org/10.1175/WAF-D-16-0099.1). URL <http://journals.ametsoc.org/doi/abs/10.1175/WAF-D-16-0099.1>.
- A. J. Newman, P. A. Kucera, and L. F. Bliven. Presenting the Snowflake Video Imager (SVI). *J. Atmos. Oceanic Technol.*, 26(2):167–179, February 2009. ISSN 0739-0572. doi: [10.1175/2008JTECHA1148.1](https://doi.org/10.1175/2008JTECHA1148.1). URL [https://journals.ametsoc.org/doi/abs/10.1175/2008JTECHA1148.1](http://journals.ametsoc.org/doi/abs/10.1175/2008JTECHA1148.1).
- L. Norin, A. Devasthale, T. S. L'Ecuyer, N. B. Wood, and M. Smalley. Intercomparison of snowfall estimates derived from the CloudSat Cloud Profiling Radar and the ground-based weather radar network over Sweden. *Atmos. Meas. Tech.*, 8(12):5009–5021, December 2015. ISSN 1867-8548. doi: [10.5194/amt-8-5009-2015](https://doi.org/10.5194/amt-8-5009-2015). URL <https://www.atmos-meas-tech.net/8/5009/2015/>.
- Norwegian Meteorological Institute. MET Norway Thredds Service, 2016. URL <http://thredds.met.no/thredds/catalog/meps25epsarchive/catalog.html>.
- A.-M. Olsen and M. Granerød. Ekstremværrapport. Hendelse: Urd 26. desember met. info. no. 18/2017 ISSN X METEOROLOGI Bergen, - PDF, September

2017. URL <http://docplayer.me/48734203-Ekstremvaerrrapport-hendelse-urd-26-desember-met-info-no-18-2017-issn-x-meteorologi-bergen.html>.
- C. Palerme, Ch. Genthon, C. Claud, J. E. Kay, N. B. Wood, and T. L'Ecuyer. Evaluation of current and projected Antarctic precipitation in CMIP5 models. *Clim. Dyn.*, 48(1-2): 225–239, January 2017. ISSN 0930-7575, 1432-0894. doi: [10.1007/s00382-016-3071-1](https://doi.org/10.1007/s00382-016-3071-1). URL <https://link.springer.com/article/10.1007/s00382-016-3071-1>.
- K. Pedersen and A. Rommetveit. Hva er et «ekstremvær»?, November 2013. URL http://www.yr.no/artikkelen/hva-er-et-_ekstremvaer__-1.7890946.
- M. C. Peel, B. L. Finlayson, and T. A. Mcmahon. Updated world map of the Köppen-Geiger climate classification. *Hydrology and Earth System Sciences Discussions*, 4(2):439–473, March 2007. URL <https://hal.archives-ouvertes.fr/hal-00298818>.
- J.-P. Pinty and P. Jabouille. A mixed-phased cloud parameterization for use in a mesoscale non-hydrostatic model: Simulations of a squall line and of orographic precipitation. pages 217–220. Amer. Meteor. Soc., 1998.
- R. E. Rinehart. *Radar for Meteorologists: Or You, Too, Can be a Radar Meteorologist*. Rinehart Publications, 2010. ISBN 978-0-9658002-3-5. Google-Books-ID: VqatcQAACAAJ.
- C. D. Rodgers. *Inverse Methods for Atmospheric Sounding: Theory and Practice*. World Scientific, 2000. ISBN 978-981-02-2740-1. Google-Books-ID: FjxqDQAAQBAJ.
- J. J. Rutz, W. J. Steenburgh, and F. M. Ralph. Climatological Characteristics of Atmospheric Rivers and Their Inland Penetration over the Western United States. *Mon. Wea. Rev.*, 142(2):905–921, January 2014. ISSN 0027-0644. doi: [10.1175/MWR-D-13-00168.1](https://doi.org/10.1175/MWR-D-13-00168.1). URL <https://journals.ametsoc.org/doi/abs/10.1175/MWR-D-13-00168.1>.
- S. Ruud, H. Carr Ekroll, A. Bakke Foss, H. O. Torgersen, and P. Annar Holm. To tonn tungt skilt blåste ned da ekstremværet traff Oslo og Østlandet i natt, December 2016. URL <https://www.aftenposten.no/article/ap-2z6wy.html>.
- G. L. Stephens. *Remote Sensing of the Lower Atmosphere: An Introduction*. Oxford University Press, 1994. ISBN 978-0-19-508188-6. Google-Books-ID: 2FcRAQAAIAAJ.

- G. L. Stephens and N. B. Wood. Properties of Tropical Convection Observed by Millimeter-Wave Radar Systems. *Monthly Weather Review*, 135(3):821–842, March 2007. ISSN 0027-0644, 1520-0493. doi: [10.1175/MWR3321.1](https://doi.org/10.1175/MWR3321.1). URL <http://journals.ametsoc.org/doi/abs/10.1175/MWR3321.1>.
- G. L. Stephens, D. G. Vane, R. J. Boain, G. G. Mace, K. Sassen, Z. Wang, A. J. Illingworth, E. J. O’Connor, W. B. Rossow, S. L. Durden, S. D. Miller, R. T. Austin, A. Benedetti, C. Mitrescu, and the CloudSat Science Team. THE CLOUDSAT MISSION AND THE A-TRAIN: A New Dimension of Space-Based Observations of Clouds and Precipitation. *Bull. Am. Meteorol. Soc.*, 83(12):1771–1790, December 2002. ISSN 0003-0007, 1520-0477. doi: [10.1175/BAMS-83-12-1771](https://doi.org/10.1175/BAMS-83-12-1771). URL <http://journals.ametsoc.org/doi/10.1175/BAMS-83-12-1771>.
- University Wyoming. Atmospheric Soundings, January 2018. URL <http://weather.uwyo.edu/upperair/sounding.html>.
- M. A. Wolff. WMO Solid Precipitation Intercomparison Experiment (WMO-SPICE), Ch. 4.2.4 Precipitation measurements in areas with high winds and/or complex terrain. unpublished, 2018.
- M. A. Wolff, R. Brækkan, K. Isaksen, and E. Ruud. A new testsite for wind correction of precipitation measurements at a mountain plateau in southern Norway. In *Proceedings of WMO Technical Conference on Meteorological and Environmental Instruments and Methods of Observation (TECO-2010). Instruments and Observing Methods Report*, 2010.
- M. A. Wolff, K. Isaksen, R. Brækkan, E. Alfnes, A. Petersen-Øverleir, and E Ruud. Measurements of wind-induced loss of solid precipitation: description of a Norwegian field study. *Hydrol. Res.*, 44(1):35–43, February 2013. ISSN 0029-1277, 2224-7955. doi: [10.2166/nh.2012.166](https://doi.org/10.2166/nh.2012.166). URL <http://hr.iwaponline.com/content/44/1/35>.
- M. A. Wolff, K. Isaksen, A. Petersen-Øverleir, K. Ødemark, T. Reitan, and R. Brækkan. Derivation of a new continuous adjustment function for correcting wind-induced loss of solid precipitation: results of a Norwegian field study. *Hydrol. Earth Syst. Sci.*, 19(2):951–967, February 2015. ISSN 1607-7938. doi: [10.5194/hess-19-951-2015](https://doi.org/10.5194/hess-19-951-2015). URL <https://www.hydrol-earth-syst-sci.net/19/951/2015/>.

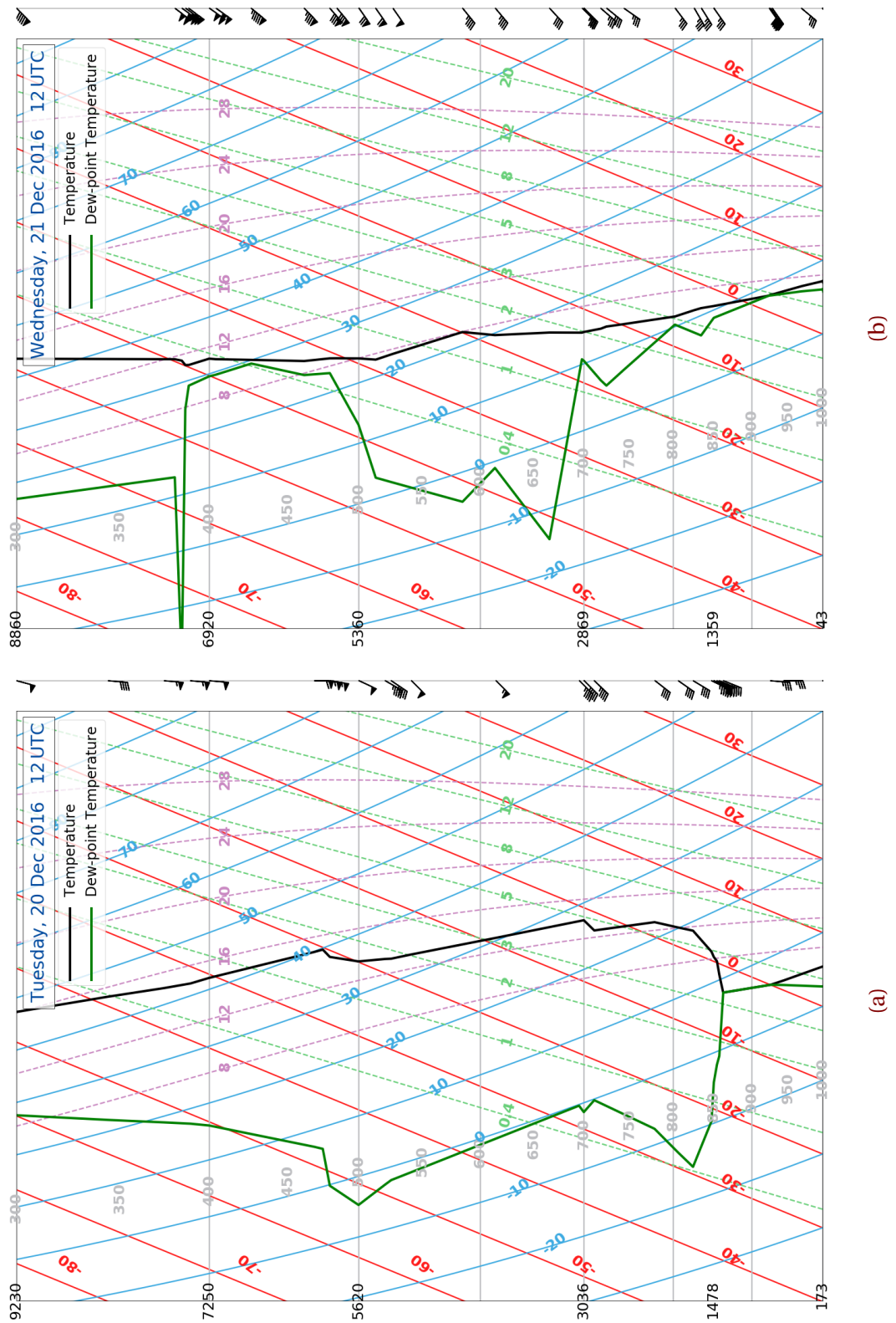
- N. B. Wood. *Estimation of snow microphysical properties with application to millimeter-wavelength radar retrievals for snowfall rate.* Ph.D., Colorado State University, 2011. URL https://dspace.library.colostate.edu/bitstream/handle/10217/48170/Wood_colostate_0053A_10476.pdf?sequence=1&isAllowed=y.
- N. B. Wood, T. S. L'Ecuyer, D. G. Vane, G. L. Stephens, and P. Partain. Level 2c snow profile process description and interface control document. Technical Report, 2013. URL http://www.cloudsat.cira.colostate.edu/sites/default/files/products/files/2C-SNOW-PROFILE_PDICD.P_R04.20130210.pdf.
- N. B. Wood, T. S. L'Ecuyer, A. J. Heymsfield, G. L. Stephens, D. R. Hudak, and P. Rodriguez. Estimating snow microphysical properties using collocated multisensor observations. *J. Geophys. Res. Atmos.*, 119(14):8941–8961, July 2014. ISSN 2169-8996. doi: [10.1002/2013JD021303](https://doi.org/10.1002/2013JD021303). URL <http://onlinelibrary.wiley.com/doi/10.1002/2013JD021303/abstract>.
- N. B. Wood, T. S. L'Ecuyer, A. J. Heymsfield, and G. L. Stephens. Microphysical Constraints on Millimeter-Wavelength Scattering Properties of Snow Particles. *J. Appl. Meteor. Climatol.*, 54(4):909–931, January 2015. ISSN 1558-8424. doi: [10.1175/JAMC-D-14-0137.1](https://doi.org/10.1175/JAMC-D-14-0137.1). URL <http://journals.ametsoc.org/doi/10.1175/JAMC-D-14-0137.1>.

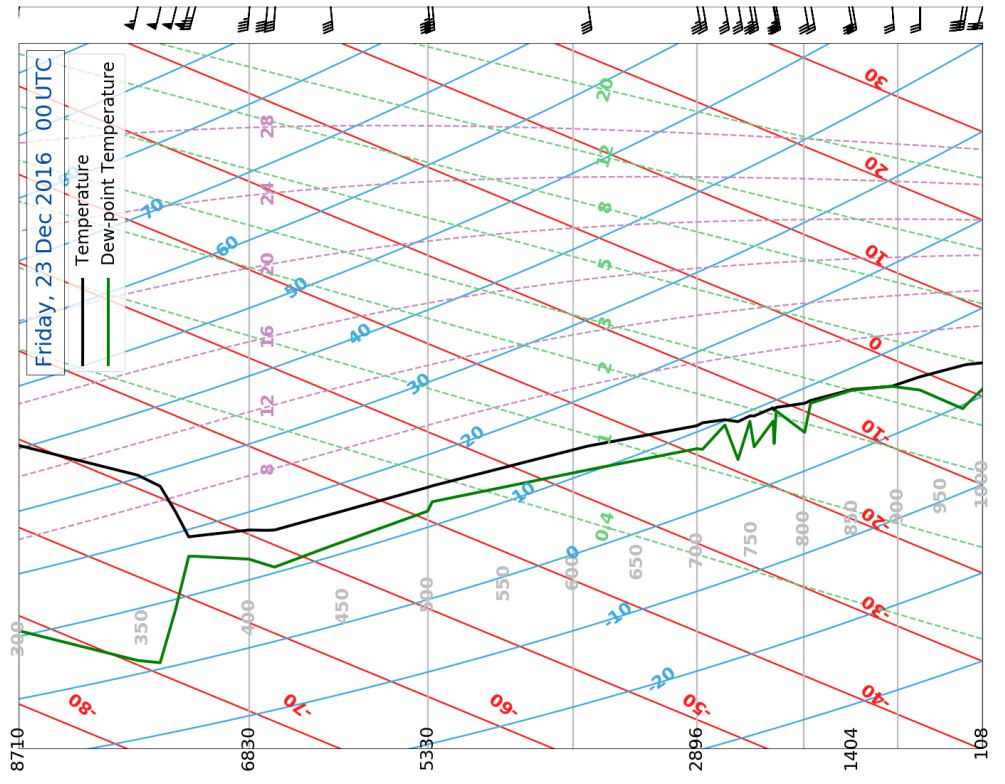
APPENDIX A: SYNOPTIC WEATHER SITUATION

A.1 SKEW-T LOG-P DIAGRAM FROM STAVANGER

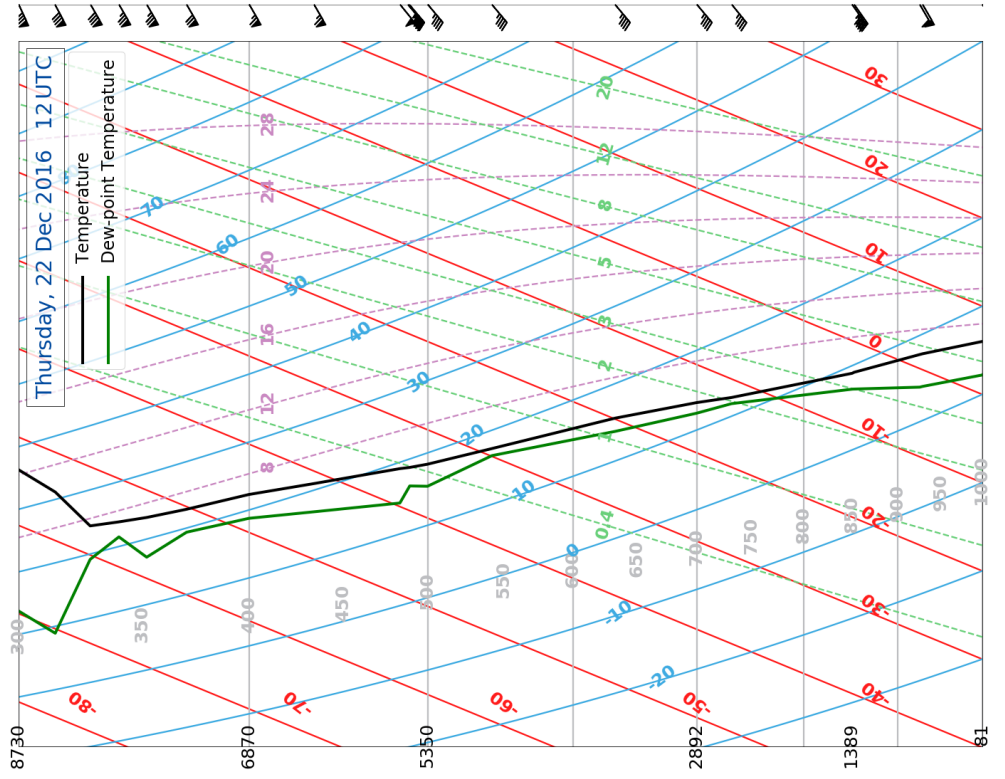
The Skew-T log-P diagram shows the observed vertical temperature and dew-point temperature at Stavanger. The data are taken from [University Wyoming \[2018\]](#) and processed in Python.

Isobars are grey lines, every 50 hPa, dry adiabats are blue (labelled in $^{\circ}\text{C}$), isotherms are red [$^{\circ}\text{C}$], water vapour mixing ratios are green, dashed in $[\text{gkg}^{-1}]$, and moist adiabats are dashed, purple lines (labelled in [$^{\circ}\text{C}$]).





(d)



(c)

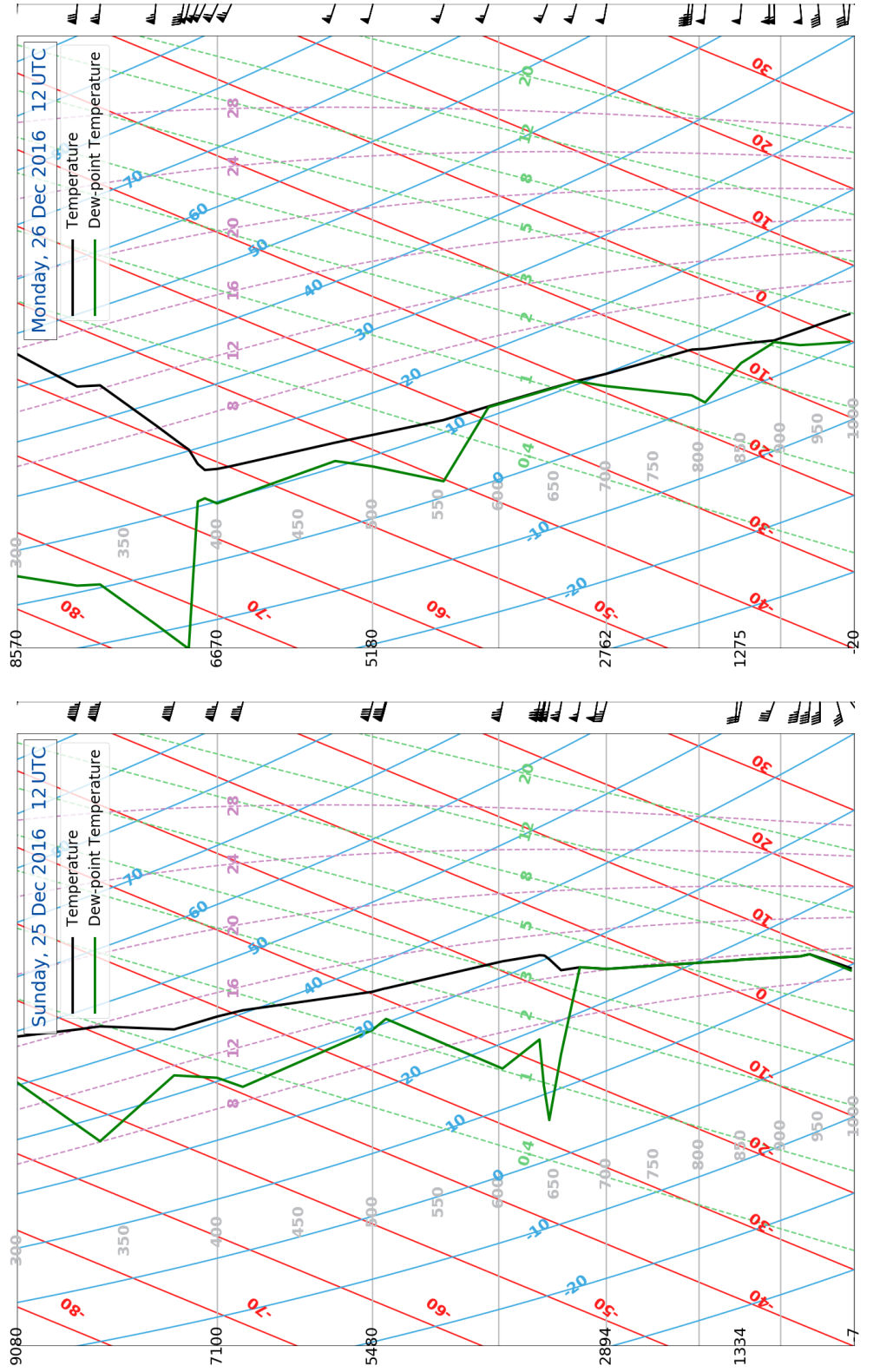


Figure A.1.1: Vertical profiles of atmospheric temperature (black) and dew-point temperature (green) during 20 December 2016 to 26 December 2016. Vertical Profiles from 24 December 2016 are missing at the webpage <http://weather.uwyo.edu/upperair/sounding.html>

APPENDIX B: FORWARD MODEL

B.1 SCATTERING MODEL

Table B.1.1: Branched 6-arm spatial particle with porosities, 2D, mass oriented scattering scheme at 24.0GHz. \mathbf{r} , particle size of the snow particle; $\mathbf{m}(\mathbf{r})$, particle mass; $\sigma_{\text{bk}}(\mathbf{r})$ and $\sigma_{\text{ext}}(\mathbf{r})$, backscattering and extinction cross-section, respectively.

\mathbf{r} [μm]	$\mathbf{m}(\mathbf{r})$ [kg]	$\sigma_{\text{bk}}(\mathbf{r})$ [m^{-2}]	$\sigma_{\text{ext}}(\mathbf{r})$ [m^{-2}]
35.27	1.68529×10^{-10}	8.85111×10^{-17}	4.85381×10^{-17}
41.73	2.79128×10^{-10}	2.00612×10^{-16}	1.28776×10^{-16}
47.87	4.21355×10^{-10}	4.792×10^{-16}	2.9959×10^{-16}
53.76	5.96809×10^{-10}	1.02733×10^{-15}	6.08871×10^{-16}
59.45	8.07074×10^{-10}	1.68272×10^{-15}	1.09633×10^{-15}
70.34	1.3368×10^{-9}	5.7444×10^{-15}	3.61096×10^{-15}
80.69	2.01798×10^{-9}	1.0899×10^{-14}	6.93961×10^{-15}
90.63	2.85939×10^{-9}	2.244×10^{-14}	1.42249×10^{-14}
100.20	3.86421×10^{-9}	3.7814×10^{-14}	2.73019×10^{-14}
109.50	5.04313×10^{-9}	7.05869×10^{-14}	5.36211×10^{-14}
118.60	6.40785×10^{-9}	1.16874×10^{-13}	9.74644×10^{-14}
127.40	7.94266×10^{-9}	1.67227×10^{-13}	1.56602×10^{-13}
144.50	1.15894×10^{-8}	3.41952×10^{-13}	4.19048×10^{-13}
160.90	1.60002×10^{-8}	7.30397×10^{-13}	1.05187×10^{-12}

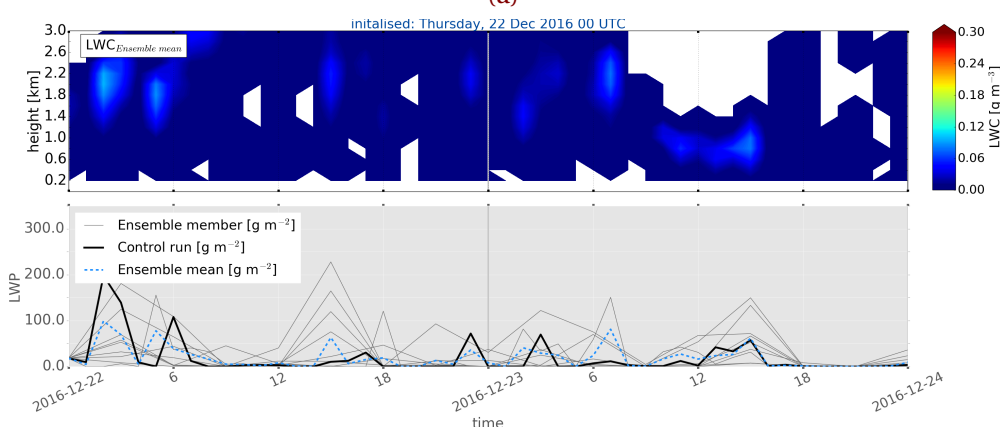
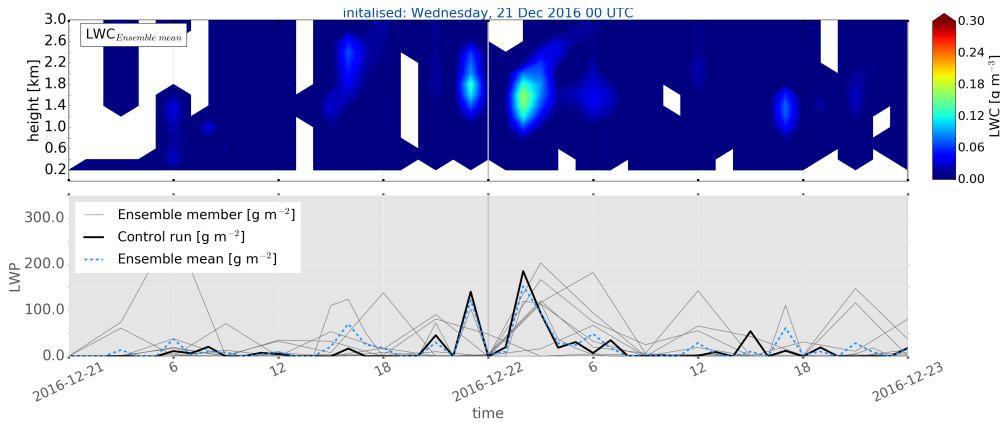
Continued on next page

Table B.1.1 Continued from previous page

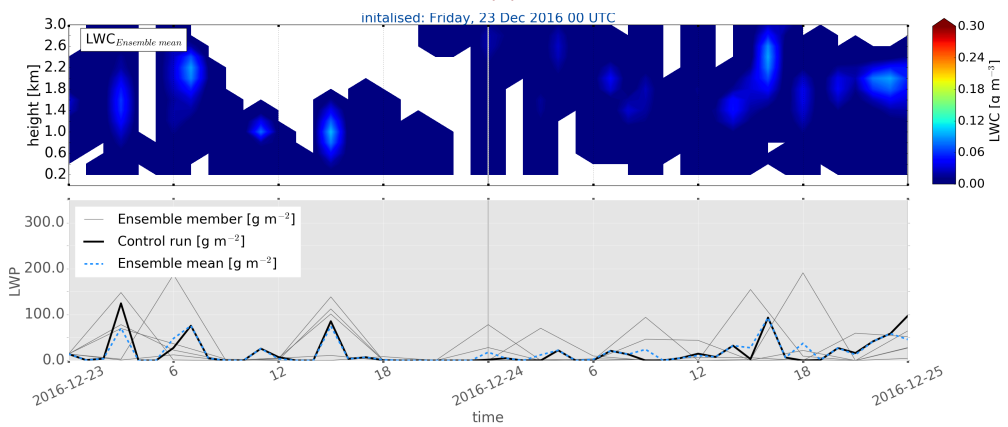
r [μm]	m(r) [kg]	$\sigma_{\text{bk}}(\mathbf{r})$ [m^{-2}]	$\sigma_{\text{ext}}(\mathbf{r})$ [m^{-2}]
176.80	2.12278×10^{-8}	1.13638×10^{-12}	2.00359×10^{-12}
192.30	2.73147×10^{-8}	2.05333×10^{-12}	3.63531×10^{-12}
236.50	5.08103×10^{-8}	5.94138×10^{-12}	1.5256×10^{-11}
278.10	8.26154×10^{-8}	1.57715×10^{-11}	4.31927×10^{-11}
317.70	1.23171×10^{-7}	3.68719×10^{-11}	9.71916×10^{-11}
355.80	1.73012×10^{-7}	6.46005×10^{-11}	1.89057×10^{-10}
392.60	2.32439×10^{-7}	1.29191×10^{-10}	3.5246×10^{-10}
428.20	3.01577×10^{-7}	1.7526×10^{-10}	5.67393×10^{-10}
463.00	3.81242×10^{-7}	3.58177×10^{-10}	8.76374×10^{-10}
496.90	4.71265×10^{-7}	5.86279×10^{-10}	1.30417×10^{-9}
530.10	5.72178×10^{-7}	8.50141×10^{-10}	1.8862×10^{-9}
562.60	6.84002×10^{-7}	1.04566×10^{-9}	2.60854×10^{-9}
594.50	8.07074×10^{-7}	1.54514×10^{-9}	3.68176×10^{-9}
625.80	9.41379×10^{-7}	1.61704×10^{-9}	4.48578×10^{-9}
656.60	1.08733×10^{-6}	2.10709×10^{-9}	5.71184×10^{-9}
687.00	1.24546×10^{-6}	3.31567×10^{-9}	7.85938×10^{-9}
717.00	1.41584×10^{-6}	3.73598×10^{-9}	9.50817×10^{-9}
746.50	1.59789×10^{-6}	4.40591×10^{-9}	1.14824×10^{-8}
775.60	1.79214×10^{-6}	5.1432×10^{-9}	1.37371×10^{-8}
804.40	1.99928×10^{-6}	4.21261×10^{-9}	1.59603×10^{-8}
832.90	2.2194×10^{-6}	7.0875×10^{-9}	1.90438×10^{-8}
861.10	2.45255×10^{-6}	7.606×10^{-9}	2.17023×10^{-8}
888.90	2.69784×10^{-6}	9.61605×10^{-9}	2.52476×10^{-8}
916.50	2.95703×10^{-6}	1.20108×10^{-8}	2.91329×10^{-8}
943.80	3.22922×10^{-6}	1.29326×10^{-8}	3.30911×10^{-8}
970.80	3.51437×10^{-6}	1.53246×10^{-8}	3.82595×10^{-8}
997.60	3.81353×10^{-6}	1.32687×10^{-8}	4.344×10^{-8}

APPENDIX C: RESULTS

C.1 LWC AND LWP FROM MEPS



(b)



(c)

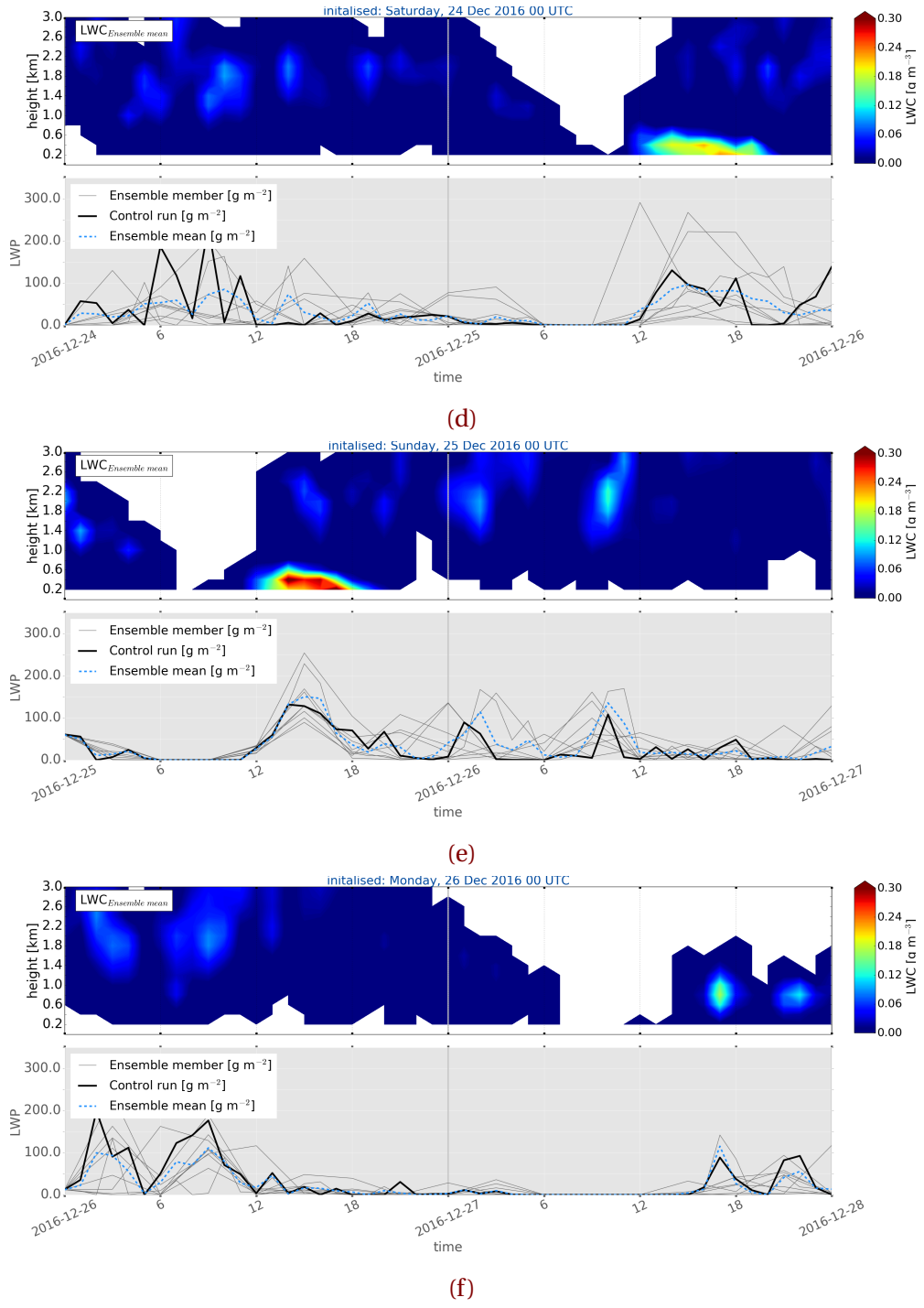
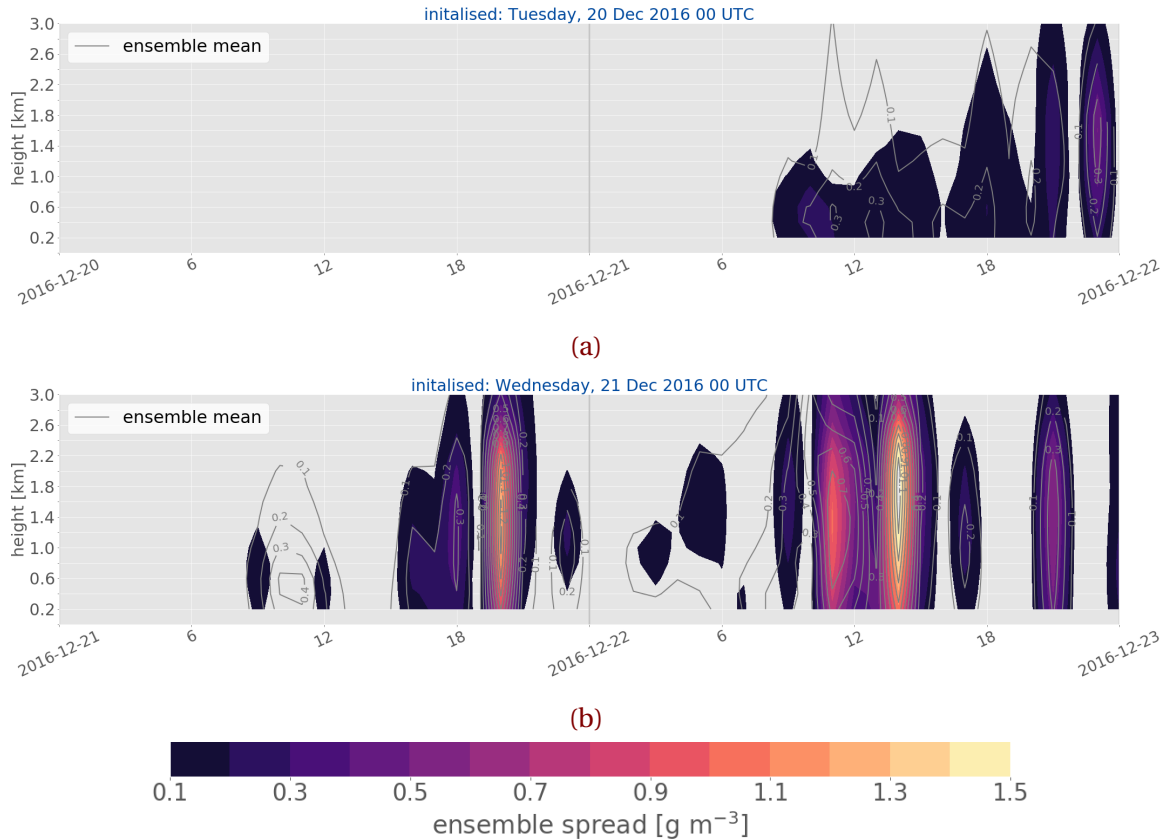
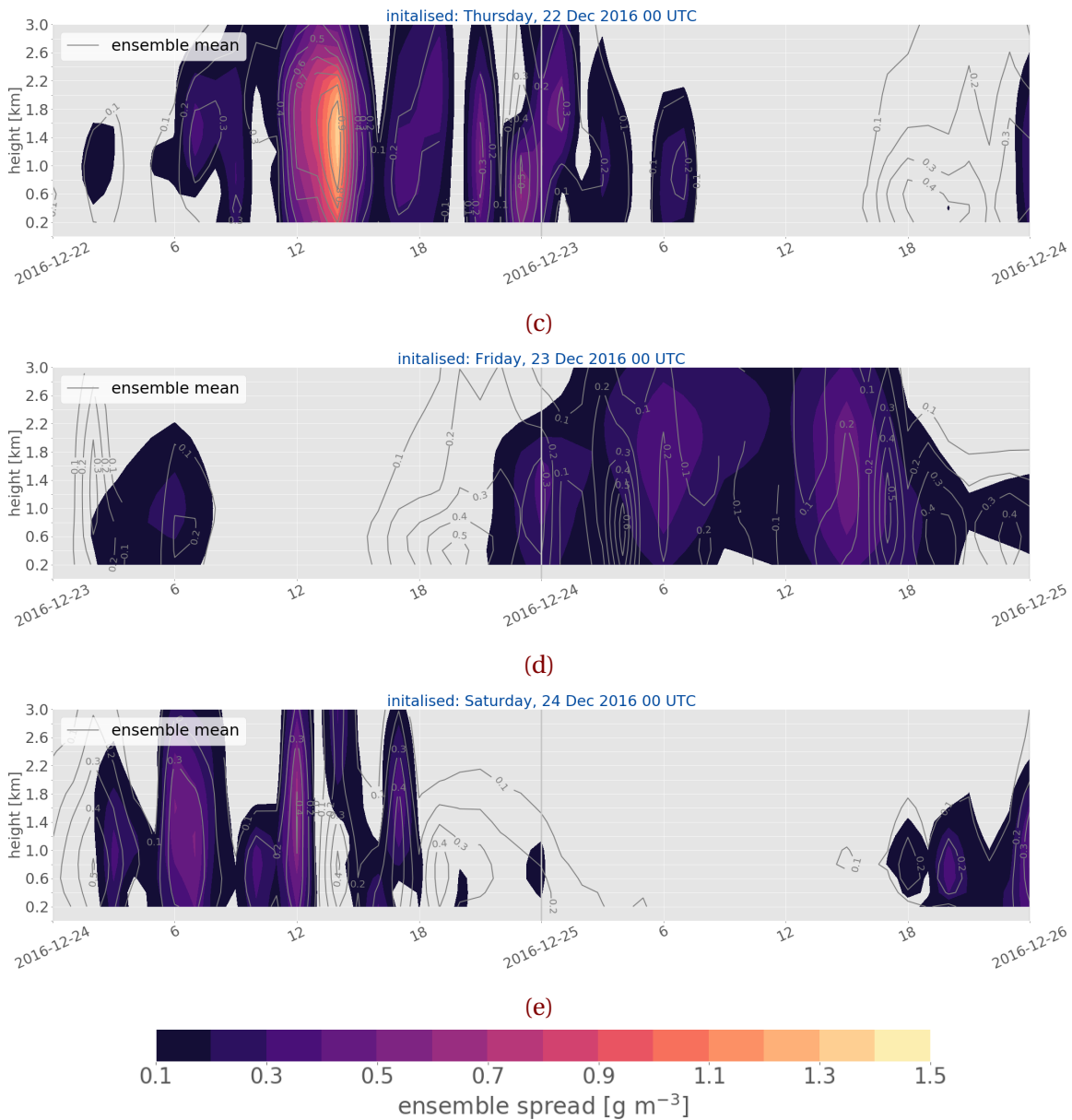


Figure C.1.1: Upper panel: 200 m-averaged LWC ensemble mean forecast from MEPS. Lower panel: LWP from MEPS, initialised at 0 UTC. Black line represents the deterministic forecast, the dotted blue line the ensemble mean and the grey lines the nine perturbed members.

C.2 ENSEMBLE SPREAD





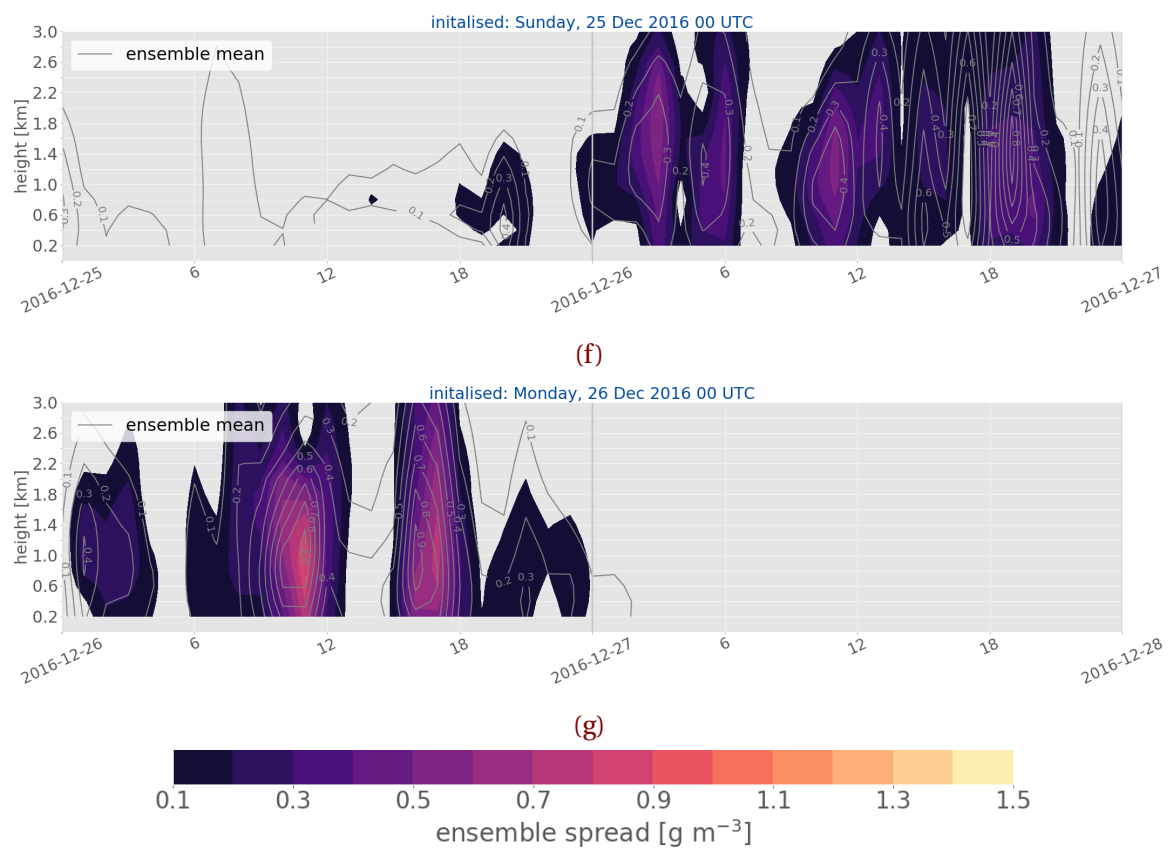
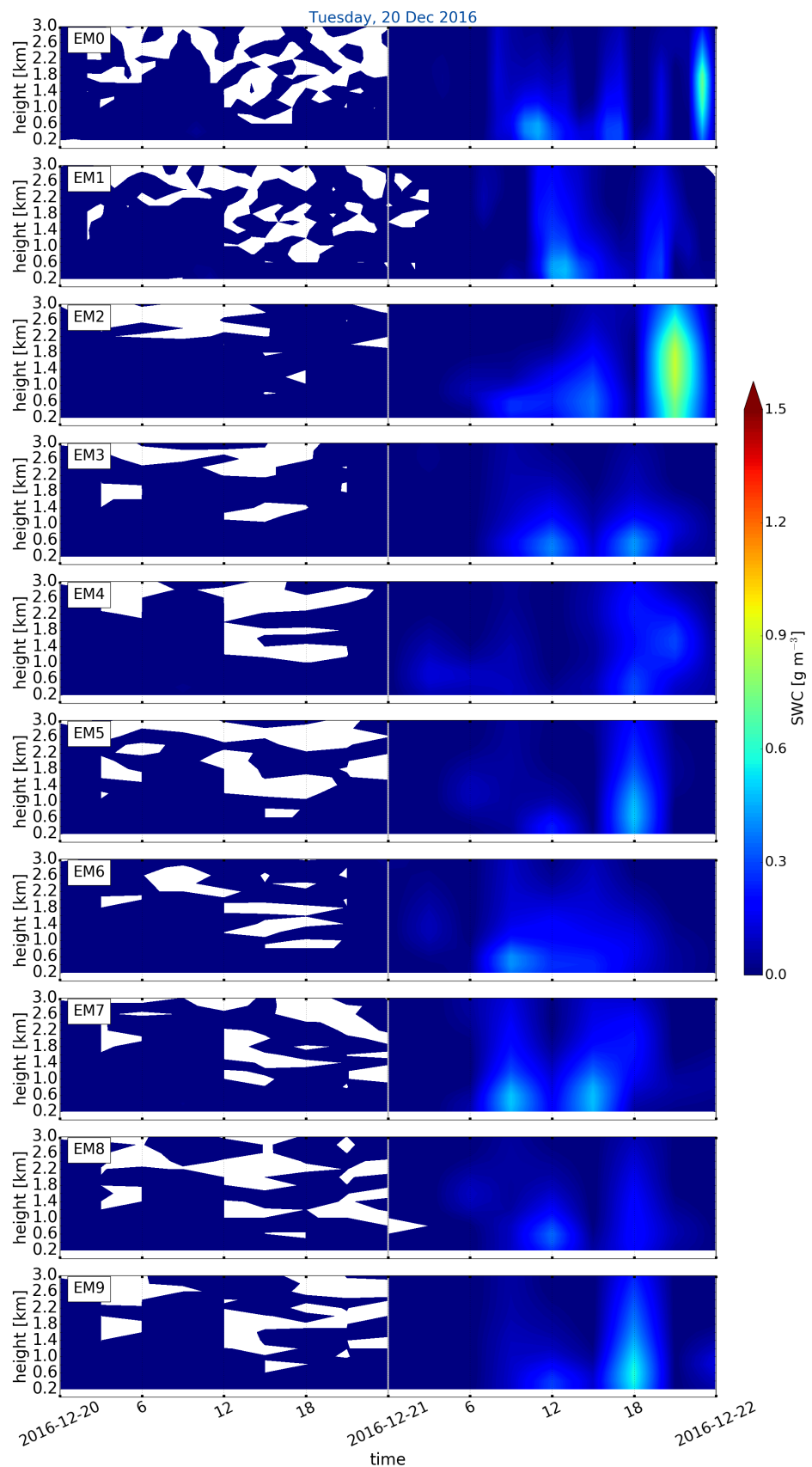
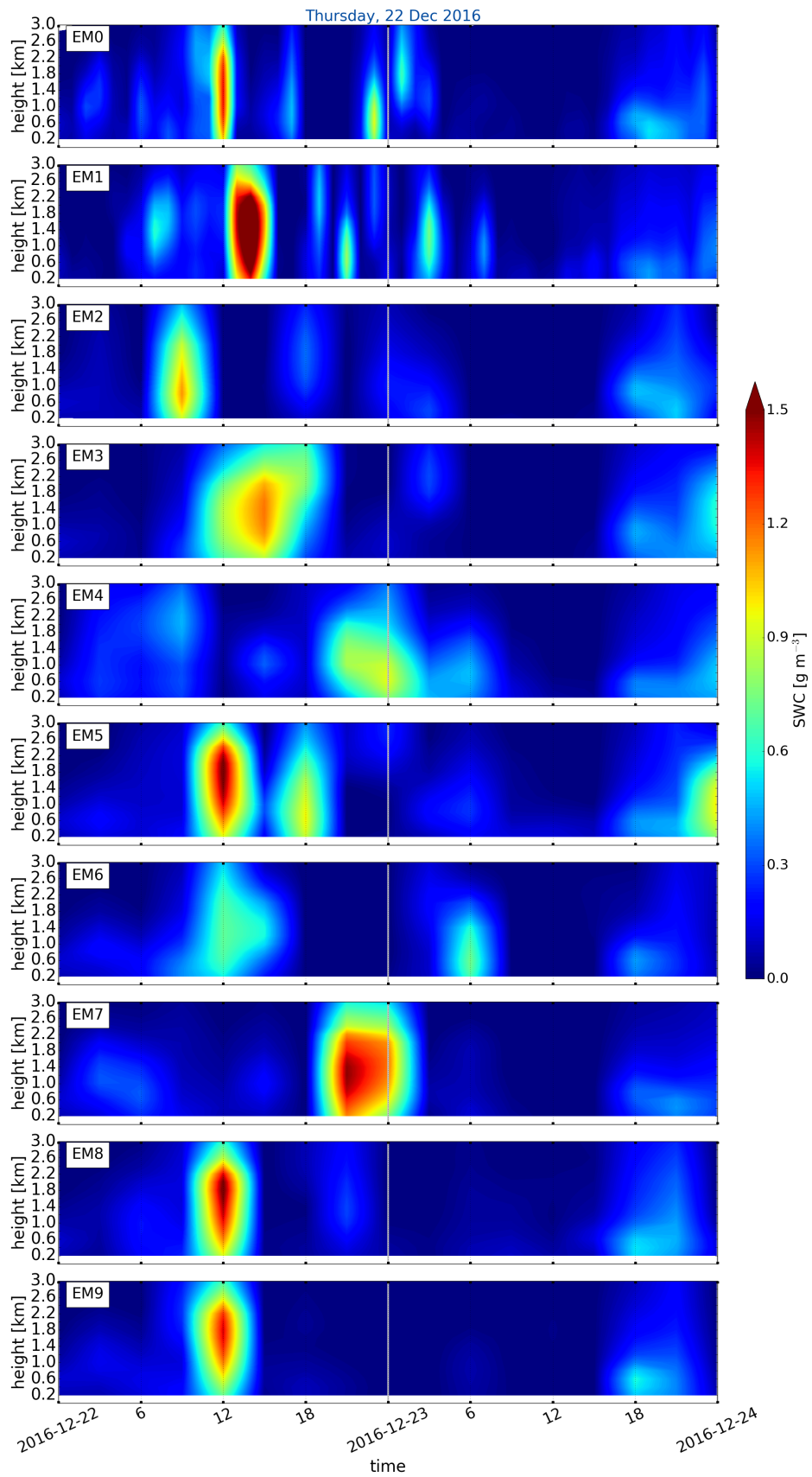


Figure C.2.1: Ensemble spread of the SWC of the ten ensemble members of MEPS. The lighter the colour according to the colour bar the higher the standard deviation between the perturbed ensemble members. In grey the ensemble mean of all ten members.

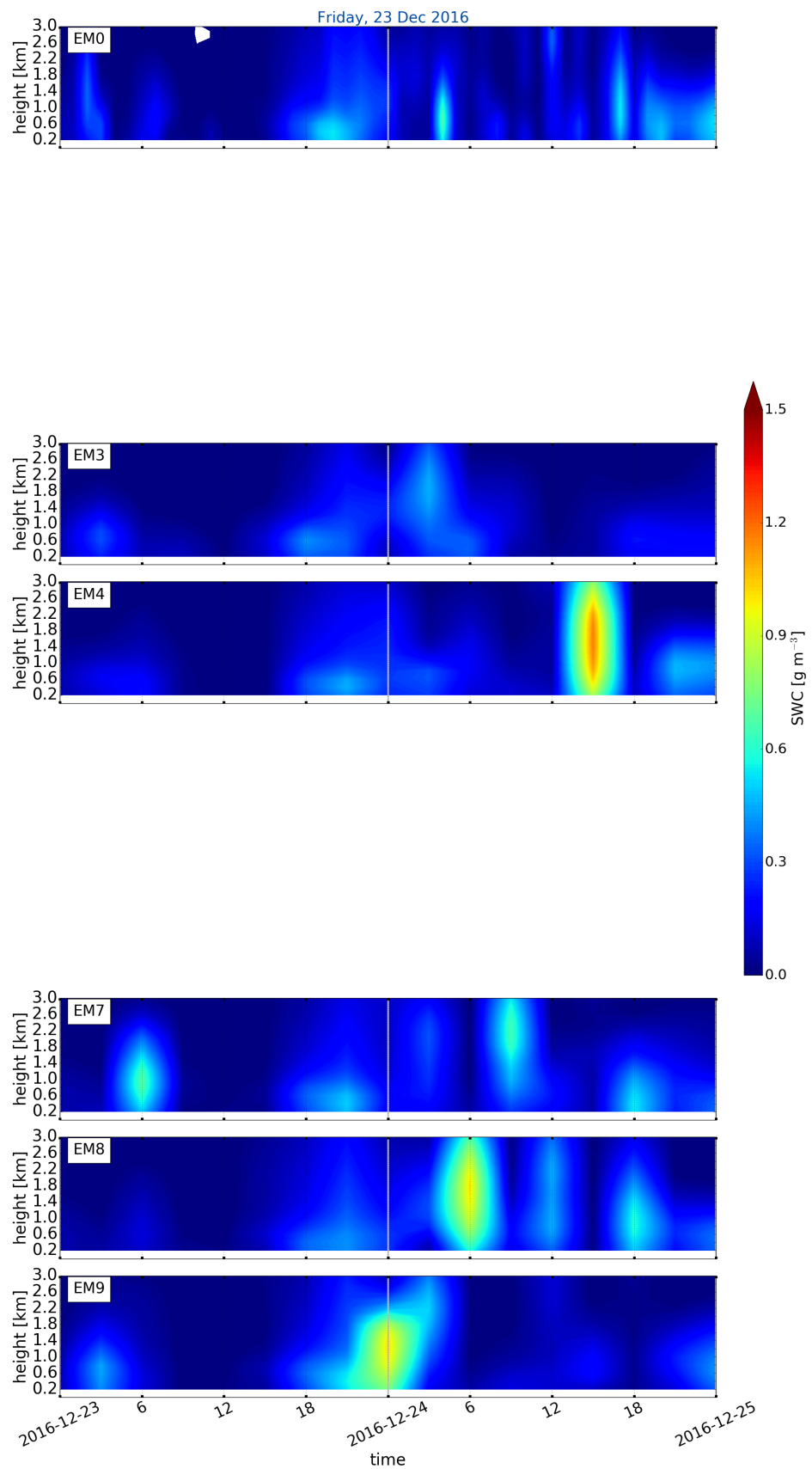
C.3 VERTICAL SWC - ENSEMBLE MEMBER 0 TO 9



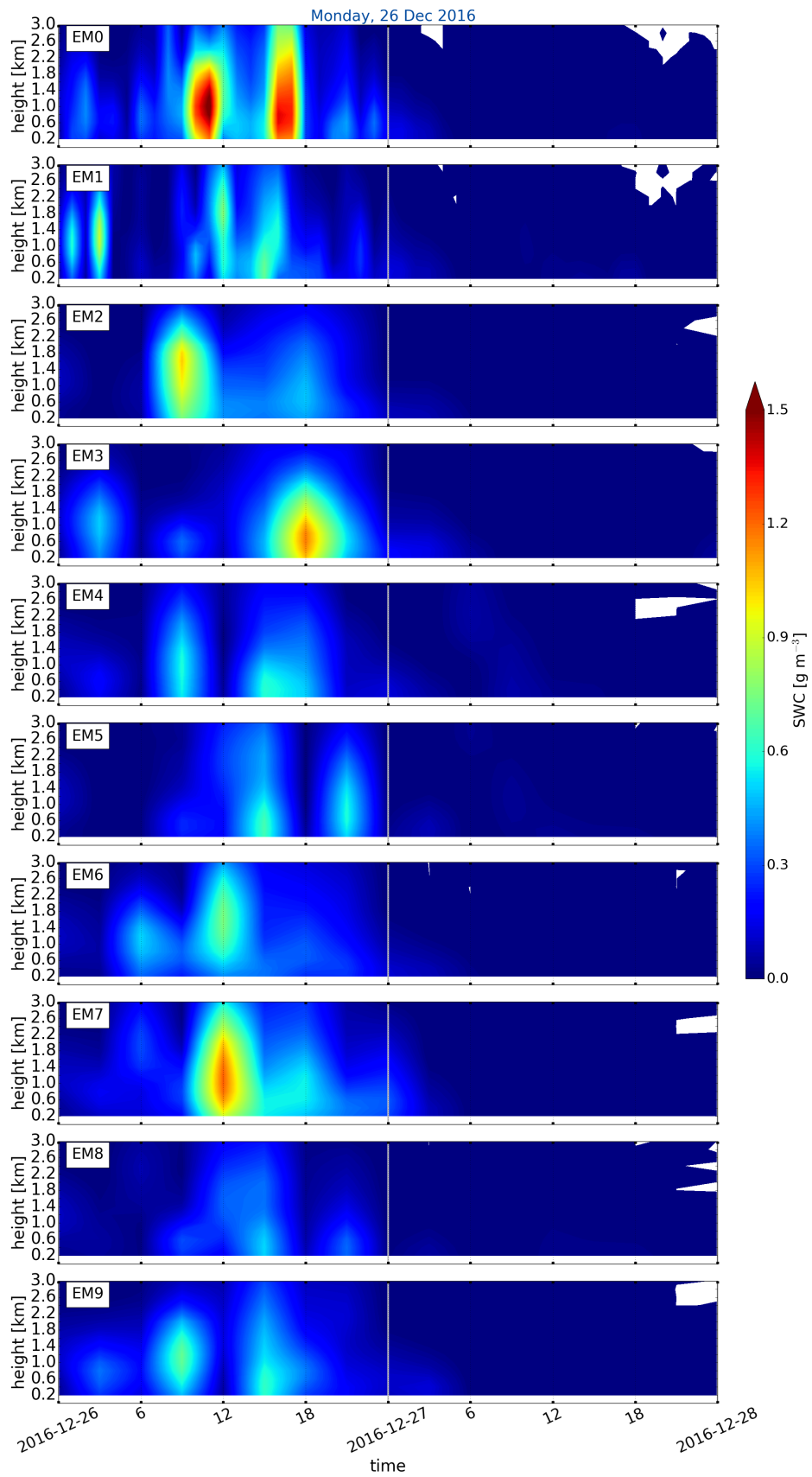
(a) initialised Tuesday, 20 December 2016 at 00 UTC forecast for 48 h.



(b) SWC of all ensemble members initialised Thursday, 22 December 2016 at 00 UTC forecast for 48 h.



(c) SWC of all ensemble members initialised Friday, 23 December 2016 at 00 UTC forecast for 48 h.



(d) SWC of all ensemble members initialised Monday, 26 December 2016 at 00 UTC forecast for 48 h.

Figure C.3.1: Vertical SWC of each individual ensemble member from 0 to 9